CRANFIELD UNIVERSITY

Zacharias Ioannis ZACHARIADIS

High Resolution And High Order Methods For RANS Modelling & Aerodynamic Optimization

SCHOOL OF ENGINEERING

PhD THESIS

CRANFIELD UNIVERSITY

SCHOOL OF ENGINEERING

PhD THESIS

Academic Year 2008-2009

Zacharias Ioannis ZACHARIADIS

High Resolution And High Order Methods For RANS Modelling & Aerodynamic Optimization

Supervisors: D. Drikakis, E. Shapiro

October 2008

This thesis is submitted in partial fulfilment of the requirements
for the degree of Doctor of Philosophy

©Cranfield University 2008. All rights reserved. No part of this publication may be reproduced without the written permission of the copyright owner.

To my most loved ones:

Πέτρο, *Καλλιόπη*, *Ιωάννη*, Παναγιώτα & *Τρύφων*.

Acknowledgements

Several people have made contribution to this project and it is a pleasure to acknowledge them. My most heartfelt thanks go to my supervisor Prof. Dimitri Drikaki for giving me the opportunity to explore the amazing world of CFD. His guidance and support are greatly appreciated. I am also grateful to Dr. Evgeniy Shapiro for his invaluable advice and motivation, especially through the dark days of this journey. I would also like to thank Dr. Timoleon Kipouros for providing the MOTS libraries and for sharing his expertise and experience in multi-objective optimisation.

Part of this work was funded by the European FP 6 "FRIEND-COPTER" project and is gratefully acknowledged.

Finally, I would like to thank my family, friends and Panagiota for their unconditional support over the four years of this research and earlier. In particular, I owe them all a great deal for shaping my character and fine-tuning my intellectual abilities and encouraging both creativity and rigor in my work.

Abstract

With the optimisation of fixed aerodynamic shapes reaching its limits, the active flow control concept increasingly attracts attention of both academia and industry. Adaptive wing technology, and shape morphing airfoils in particular, represents a promising way forward. The aerodynamic performance of the morphing profiles is an important issue affecting the overall aerodynamic performance of an adaptive wing.

A new concept of active flow, the Active Camber concept has been investigated. The actuator is integrated into the aerofoil and aerofoil morphing is realized via camber deformation. In order to identify the most aerodynamically efficient designs, an optimisation study has been performed using high resolution methods in conjunction with a two equation eddy viscosity model.

Several different types of previously proposed compressible filters, including monotone upstream-centered schemes for conservation laws (MUSCL) and weighted essential non-oscillatory (WENO) filters, are incorporated and investigated in the present research. The newly developed CFD solver is validated and the effect that high resolution methods have on turbulent flow simulations is highlighted. The outermost goal is the development of a robust high resolution CFD method that will efficiently and accurately simulate various phenomena, such as shock/boundary layer interaction, flow separation and turbulence and thus provide the numerical framework for analysis and aerodynamic aerofoil design.

With respect to the latter a multi-objective integrated design system (MOBID) has been developed that incorporates the CFD solver and

a state-of-the-art heuristic optimisation algorithm, along with an efficient parametrization technique and a fast and robust method of propagating geometric displacements. The methodologies in the MO-BID system resulted in the identification of the design vectors that revealed aerodynamic performance gains over the datum aerofoil design. The Pareto front provided a clear picture of the achievable trade-offs between the competing objectives.

Furthermore, the implementation of different numerical schemes led to significant differences in the optimised airfoil shape, thus highlighting the need for high-resolution methods in aerodynamic optimisation.

Contents

List of Figures

Nomenclature

Greek Symbols

α	Angle of attack
δ_{ij}	Kronecker delta function
ϵ	Rate of turbulent dissipation
γ	Specific heat ratio
λ	Bulk viscosity
μ	Molecular viscosity
μ_t	Turbulent eddy viscosity
ν	Kinematic viscoscity of the fluid
ω	Specific rate of turbulent dissipation
ρ	Fluid density
τ_{ij}^l	Molecular stress tensor
τ_{ij}^t	Reynolds stress tensor
κ	Von Kármán constant

Symbols

c_d	Coefficient of drag

c_l Coefficient of lift

c_m Coefficient of moment

c_p Specific heat at constant pressure

C_D Cross-Diffusion term

c_v Specific heat at constant volume

e Total energy

e_{in} Internal energy

J Geometric Jacobian of the inverse transformation

k Turbulent kinetic energy

L/D Lift-to-Drag ratio

M_∞ Freestream Mach number

p Pressure

Pr Laminar Prandtl number, $Pr = 0.7$

P_k Production term

Pr_t Turbulent Prandtl number, $Pr_t = 0.9$

p_t Turbulent pressure

q_i^t Turbulent heat flux vector

q_i^l Molecular heat flux vector

R Universal gas constant

Re Reynolds number

Re_∞ Reynolds number, based on chord length

S_{ij} Mean strain rate

T Temperature

u_i Velocity vector

u_τ Friction velocity

x_a Active chord percentage

y Normal distance to solid boundary

y^+ Dimensionless wall distance, $y^+ = \frac{yu_\tau}{\nu}$

z^*_{max} Non-dimensional actuator deflection

Acronyms

AoA Angle of Attack (degrees)

BVI Blade Vortex Interaction

CFD Computational Fluid Dynamics

DNS Direct Numerical Simulations

ENO Essentially Nonoscillatory

IBC Individual Blade Control

$ILES$ Implicit LES

LES Large Eddy Simulations

$LEVM$ Linear Eddy Viscosity Models

LTM Long-Term-Memory

$MEMS$ Micro-electronic-mechanical-systems

$MOTS$ Multi-Objective Tabu Search

MTM Medium-Term-Memory

$MUSCL$ Monotone Upstream-centered Scheme for Conservation Laws

$NLEVM$ Non-Linear Eddy Viscosity Models

$RANS$ Reynolds-Averaged Navier Stokes

RSM Reynolds Stress Models

SGS Subgrid Scale Stress

SST Shear Stress Transport

STM Short-Term-Memory

TI Turbulent Intensity

TNT Turbulent/ Non Turbulent

TS Tabu Search

TVD Total Variation Diminishing

$WENO$ Weighted Essentially Nonoscillatory

Chapter 1

Introduction

One of the most important dimensionless quantity in Fluid Dynamics is the Reynolds number, which is a measure of the ratio of inertia to viscous forces. The Reynolds number provides a criterion for determining dynamic similitude between real and model applications, but, most critically, it describes whether a flow is laminar or turbulent. Laminar flows correspond to low Reynolds number, where viscous forces are dominant, and the flow is characterized by smooth, constant fluid motion [1]. Most aerodynamic engineering applications occur at high Reynolds number, where the flow is dominated by inertial forces that produce chaotic fluctuations with high velocity gradients and result in three-dimensional space and time flow disturbances. The identifiable disturbance with an associated scale that characterizes its spatial extent and persistence in time can be thought of as a turbulent eddy. In fact, turbulent flows are characterised by a wide continuous spectrum of eddies. Large eddies interact with the mean flow and with each other. Through this interaction, the turbulent kinetic energy is transferred from the mean flow to large eddies and so on to smaller ones, with the smallest eddies eventually dissipating into heat through molecular viscosity. Conclusively, turbulence can be described as a spatially varying mean flow with superimposed three-dimensional eddies that are self-sustaining and enhance mixing, diffusion and dissipation [1].

Experimental results indicate that airfoil performance deteriorates when the chord Reynolds number decreases below about 5×10^5 [2, 3]. The flow over the aerofoil at these low Reynolds numbers is laminar, and even slight changes

in the flow field have significant effects in the lift-to-drag ratio. Even at low angles of attack, the laminar boundary layer on the suction surface of the aerofoil becomes subjected to an adverse pressure gradient, resulting in laminar boundary-layer separation and formation of a shear layer. Past the separation point, the boundary layer undergoes transition due to amplification of flow instabilities. At Reynolds number below 5×10^4 the separated shear layer does not reattach to the aerofoil surface and a large wake is formed [4]. In contrast, at higher Reynolds numbers, the separated shear layer may become turbulent and reattach to the aerofoil surface, resulting in the formation of a separation bubble and the development of an attached turbulent boundary layer. In both cases, laminar separation has a detrimental effect on aerofoil performance.

From an aerodynamic point of view, laminar separation leads to high pressure drag rise. On the other hand, turbulent flows result in thick boundary layers that produce more skin friction drag than laminar boundary layers, which are thinner by principle. Moreover, in compressible flows, shocks may appear that interact with the boundary layer causing flow separation. Shock/boundary layer interaction appears in many aeronautical applications, such as flows around turbomachinery blades and external flows over aircraft wings or helicopter blades. The aerodynamic performance in these applications depends strongly on the location and strength of the shocks, as well as on the flow separation, induced by the shock/boundary layer interaction. Flow separation on lifting and control surfaces of flying vehicles and/or shock/boundary-layer interaction is the main reason for a series of problems, such as drag increase, loss of lift and poor controllability, that limit the realization of engineering ingenuity.

1.1 Flow Control

It was previously stressed that the boundary layer development and the interaction of the boundary layer with the outer flow field, aggravated at high speeds by the occurrence of shock waves, limits the overall air-vehicle or air-vehicle component [5]. This interaction dictates the pressure distribution on the aerofoil surface, and subsequently the aerodynamic loads. Therefore in order to achieve

high performance for mission varying air-vehicles it is necessary to either: (a) alter the boundary layer behavior of the aerofoil, and/or (b) change the geometry of the aerofoil real time for changing freestream conditions.

Flow control essentially involves a beneficial change in the wall-bounded and/or free-shear flow with the objectives of (a) delaying/advancing boundary layer transition, (b) suppressing/enhancing turbulence and (c) preventing excessive boundary layer growth and separation. Means of boundary layer flow control include, conventional air-jet [6] and sub-boundary layer vortex generators [7], or zero-mass pulsing jets [8], deployed to delay separation, discrete suction or blowing meant to decrease viscous drag [9, 10] and unconventional deploying devices such as Gurney flaps [11], divergent trailing edges and reversed flow flaps [12] to increase lift-to-drag ratios (L/D) and c_{lmax}. Micro-electronic-mechanical-systems (MEMS) that manipulate the high-shear-stress streaks in the boundary layer [13], can also be utilised for vortex control, by affecting local leading edge separation and vortex location, to enhance maneuver capability [14].

Special consideration is also given to control the shock waves and the shock associated boundary layer development. The objective here is either to influence the shock strength, by spreading the shock associated pressure rise over a certain chordwise distance, thus reducing wave drag, or to energize the boundary layer making it less prone to adverse pressure gradients. Reducing the shock strength can be accomplished by passive or active cavity ventilation [15, 16] or by a contour bump in the shock region [17]. Energizing the boundary layer upstream of the shock may be accomplished by discrete suction [5], or by integrating vortex generators [18].

Although promising results have been obtained with the aforementioned flow control methods, adaptive wing technology is of interest in this work. Employing adaptive wing technology, where the effective aerofoil/wing geometry adjusts to the changing flow and load requirements, allows to fully explore the aerodynamic flow potential at different points of the flight envelope, thus resulting in aerodynamic performance gains during take-off, cruise, maneuver and landing and, furthermore, most likely improved structural designs [19, 20, 21, 22]. Means of realizing adaptive wing technology are predominantly geometrical adjustments including the deformation of the complete wing and/or the use of leading and

trailing edge camber variations to achieve the desired aerodynamic loads distribution. Moreover, local contour modifications, in the shock region, can be implemented to reduce shock strength that ameliorate boundary layer development and drag.

1.1.1 Flow Control in Helicopter Main Rotor Blades

Anecdotal evidence points to the increase in helicopter usage due to its ability to fly commercial, medical, rescue and law enforcements missions. These missions require flight profiles close to populated areas. Therefore, it is important that modern helicopters are further improved with respect to environmental and public acceptance. Key aspects are envisaged to be external and cabin noise reduction, vibration reduction for passenger comfort and component life, better fuel consumption and increased performance regarding flight envelope, speed and range.

The main source of noise and vibrations in the helicopter are due to the non-symmetric main rotor flow. In forward flight, the advancing and retreating blade experience varying spanwise distribution of lift and drag, that excite the blade's bending modes and result in alternating rotor hub loads and moments. Furthermore, in high speed flight, the retreating blade experiences dynamic stall while the flow at the advancing blade tip becomes transonic resulting in strong vibrations and loud noise generation. On the other hand, in descent flight or low speed maneuvers, the rotor blades interact with the tip vortices of the preceding blade. This type of interaction, termed as Blade Vortex Interaction (BVI) is another source of helicopter vibration and noise.

Because of the complex flow features, BVI cannot be easily alleviated. However, there is significant potential for improvement by actively altering the aerodynamic loads of each blade individually (Individual Blade Control) [23]. Under this scope, a lot of research has been performed and several adaptive helicopter rotor blade systems have been developed. In fact, although designs featuring hydraulic actuators have been developed and tested in helicopters [24, 25], recent research is focused on electro-mechanical actuators [26], since high performance induced strain piezo-electric actuators offer advantages in terms of weight, power

consumption, frequency bandwidth and reliability [27]. Emerging on - blade actuation technologies comprise (a) active twist control and (b) discrete flap actuation.

In active twist control, the distributed induced-strain actuation results in a continuous twisting of the blade that varies the spanwise lift distribution without affecting the aerodynamic pitching moment. In discrete flap actuation, a servo-aerodynamic control surface (leading of trailing edge flap) induces localized aerodynamic force variations, offering control of both lift and pitching moment in combination. The main advantages of the active twist concept are the aerodynamically unchanged blade profile and the absence of moving of parts, whereas the discrete flaps allow a more flexible modular design.

Under the EU FP6 Friendcopter project, a new concept for an IBC actuator, the Active Camber concept has been investigated. The actuator is integrated into the aerofoil and aerofoil morphing is realized via camber deformation. The advantages of the Active Camber concept are a smoothly deflected aerofoil contour in the chordwise direction, without the associated gaps of the discrete actuators. Since there are no moving parts nor discrete hinges, parasitic drag and discrete vortices are alleviated when the Active Chamber actuator is enabled. Furthermore, the feasible modular design provides ease of maintenance and the actuator may be detached from the host blade structure for replacement. In order to identify the most aerodynamically efficient designs, an optimisation study has been performed using high resolution methods in conjunction with a two equation eddy viscosity model.

1.2 High resolution CFD methods

Throughout the relatively short but highly evolutionary history of CFD, numerous methodologies have been devised in order to accurately predict complex flow phenomena. The state-of-the-art in modern CFD computations lies in the development and efficient implementation of high resolution methods.

High resolution methods are typically used in Direct Numerical Simulations (DNS) and Large Eddy Simulations (LES) of turbulent flows. The high order of accuracy inherent in high resolution schemes is a prerequisite in order to reduce

dissipative numerical errors and to resolve a larger range of length scales than the traditional second-order methods. On the other hand, the increase in accuracy comes at a cost, due to the large discretisation stencil required, high resolution methods are harder to code and also result in longer computation times than low-order methods.

The outermost goal of any high resolution method is to circumvent the fundamental Godunov's theorem that states that monotone methods are at most first order accurate [28]. High accuracy must be achieved without the introduction of spurious oscillations across discontinuous flow phenomena, such as shock waves and steep shear layers. Hence high resolution methods are sought to be non-oscillatory. Furthermore, positiveness must be guaranteed, that is, positive definite quantities, such as density and energy must remain positive [28]. These attractive numerical properties are satisfied by employing nonlinear discretisations, where the discrete stencil changes as a function of the solution itself. This is what distinguishes high-resolution schemes from linear second, or higher, order finite difference methods that make use of the same differencing stencil throughout the computational domain, regardless the characteristics of the solution. Following Harten's definition [29], high resolution methods exhibit the following properties:

1. provide second or higher order of accuracy in smooth regions of the flow,
2. yield solutions that are free from spurious oscillations and
3. produce high resolution of discontinuities by adapting the discetisation stencil, containing the contact wave, similar to that of first-order monotone methods.

The main approaches to achieve high resolution comprise Total Variation Diminishing (TVD), Monotone Upstream-centered Scheme for Conservation Laws (MUSCL), Essentially Nonoscillatory (ENO) and Weighted ENO (WENO) methods.

TVD methods comprise one type of Total-Variation Stable schemes, which is founded on the very condition that the total variation of the numerical solution

does not increase in time [30]. TVD schemes are highly associated with traditional Artificial Viscosity Methods. In particular, TVD methods and Artificial Viscosity Methods achieve the elimination or control of the spurious oscillations near high gradients. Both types of schemes apply the mechanism of the addition of artificial viscosity to construct schemes with accuracy higher that first order while overcoming Godunov's theorem [31]. However, in TVD methods artificial viscosity is inherent in the scheme and is applied on a more rational basis than in Artificial Viscosity methods, whereby extra diffusive terms are explicitly added to the total partial differential system.

The Monotone Upstream-centered Scheme for Conservation Laws (MUSCL) approach was introduced by Bram van Leer [32, 33, 34] in order to achieve higher order of accuracy, through modification of the piece-wise constant data in the first-order Godunov method and is used to construct high order methods. The MUSCL results in high-order of accuracy achieved through data reconstruction that is bounded via the use of limiters so as to avoid spurious oscillations [30]. MUSCL schemes have gained popularity during the 1970's and the 1980's, which is manifested by the numerous limiters developed. The most well known and commonly used limiters are ULTRABEE, SUPERBEE and MINBEE due to Roe [35], VANLEER due to van Leer [32, 33] and VANALBADA due to van Albada [36].

Essentially Non-Oscillatory (ENO) and Weighted ENO (WENO) schemes are high order accurate finite difference schemes that have been formulated and successfully applied in the resolution of problems with piecewise smooth solutions containing discontinuities [29]. ENO and WENO schemes are specifically designed for hyperbolic conservation laws. Through the use of a nonlinear adaptive procedure at the level of approximation, what is succeeded is an automatic preference for the locally smoothest stencil, which leads to the prevention of the crossing of discontinuities in the interpolation procedure [37]. Common problems that are regulated with the use of ENO and WENO schemes are shocks and complicated solution structures, including applications of compressible turbulence simulations and aeroacoustics.

1.3 Turbulence Modelling

Most practical aeronautical engineering flows are turbulent. Turbulence is one of the most-studied phenomenon in CFD. In fact, parallel to the development of numerical methods for CFD was the evolution of turbulence modelling that is a vast subject on its own. There exist three major branches of CFD that deal with the study of turbulence, namely Direct Numerical Simulation (DNS), Large Eddy Simulation (LES) and Reynolds -Averaged Navier Stokes (RANS) simulation.

In DNS the entire spectrum of spatial and temporal scales is fully resolved. DNS is applied to simple geometries of low Reynolds number flows and provides an essential tool in fundamental turbulence related research, such as transition to turbulence, bypass transition in boundary layers [38] and streak instabilities [39]. The computational cost and storage requirements of DNS increase proportionally to the Reynolds number (in three dimensions the grid points required can be approximated by $Re^{9/4}$ and the cost by Re^3 [40]). The computational constraints associated with DNS, render this numerical approach impractical for almost all engineering applications and far beyond affordable computing resources for many years to come [41].

In LES the large scales are fully resolved while the small scales are modeled. This permits the usage of larger discretisation cells and time steps than what are generally employed in DNS, thus allowing the study of much higher Reynolds flows in a computationally more efficient manner. A deduction of Kolmogorov's Universal Equilibrium Theory is that large eddies are dependent on the flow geometry whereas the small eddies display a self similar, isotropic, behavior [42]. This serves as the rational behind LES, where the large scales are mainly accounted for the transport properties in a turbulent flow and therefore are computed directly, whereas the smallest eddies are either implicitly modeled, in which case LES is labeled Implicit LES (ILES) [28] or explicitly modeled through the implementation of a Subgrid Scale Stress model (SGS). In either case the near wall resolution requirements restrict LES to relatively low Reynolds numbers making it unfeasible for most of the aeronautical engineering problems.

In view of the above, the solution of the RANS equations is the most realistic choice for real life aerodynamic problems. RANS can be best described as a

statistical approach according to which the Navier Stokes equations are time averaged. Because of the nonlinearity of the Navier Stokes equations, the time averaging procedure leads to the appearance of extra momentum fluxes that act as stresses throughout the flow, the Reynolds stresses, which are not known a priori. Herein lies the closure problem; establishing a sufficient number of equations for all unknowns [42].

Turbulence models can be classified depending on complexity, sophistication and accuracy. On top of the hierarchy lie the Reynolds Stress Models (RSM) that capture more of the flow physics while at the same time are computationally intensive since seven additional transport equations need to be solved along with the mean flow equations [43]. Due to the associated complexity and computational costs of RSM, two equation turbulence models are considered as a more viable approach for high Reynolds number applications. Furthermore, regarding the constitutive relation between Reynolds stress and mean strain rate tensors, turbulence models can be categorised to Non-Linear Eddy Viscosity Models (NLEVM) and Linear Eddy Viscosity Models (LEVM). Although, there are many approaches to the derivation of NLEVM, Explicit Algebraic RSMs (EARSM) have recently received great attention. These models are derived by applying simplifying assumptions to RSM, and demonstrate potential in predicting normal-stress anisotropy and the effects of streamline curvature, swirl, or secondary strain effects [44]. However, the increased complexity and computational cost, when compared to LEVM, prohibits the use of NLEVM in engineering design processes.

LEVM seem to offer the best balance between accuracy and computational efficiency. LEVM make use of the Boussinesq approximation to relate the Reynolds stress tensor with the mean strain rate tensor and the eddy viscosity. Since the 1950's three main categories of LEVM have evolved; algebraic models [45, 46, 47], one equation models [48, 49] and two equation models. The algebraic and one equation models are incomplete as the turbulence length scale is related to a typical flow dimension and therefore, their range of applicability is limited. On the other hand, in two equation LEVM the second scale variable is solved for a modeled transport equation and therefore are complete [42].

The current level of maturity of both high resolution methods and turbulence modelling renders the technological value of Computational Fluid Dynamics

undisputed and invaluable. Furthermore, modern Computation Fluid Dynamics methods has become an indispensable tool for design optimisation, since a plethora of different configurations can be investigated at acceptable cost and in relatively short time. Therefore it is essential to examine different aspects of flow control by performing CFD based aerodynamic optimisation.

1.4 Aerodynamic Optimisation

In general, design optimisation can be considered as the numerical process of finding a feasible set of design variables that correspond to an optimum design (solution) that satisfies the minimization or maximization of one or more quantitatively modeled objectives (functions), within the allowable design boundaries (constraints). In other words, design optimisation is the solution of the objective functions subject to constraints. In solving optimisation problems there exist the traditional gradient-based methods and the more recent meta-heuristic optimisation techniques such as Simulated Annealing, Genetic Algorithms, Evolution Strategies and Tabu Search.

Furthermore, in multi-objective aerodynamic optimisation problems, the traditional gradient-based methods are not appropriate because of the highly constrained, non-linear nature of the underlying problem [50]. Consequently, gradient-based optimisation techniques tend to get locked in the numerous local minima in the design space of aerodynamic applications [51]. Furthermore it has been found that the computational time required by, derivative free, stochastic methods has been comparable to that of gradient-based methods [52]. For the above reasons, heuristic and meta-heuristic methods became popular. The most widely used meta-heuristic algorithms are Simulated Annealing [53, 54], Genetic Algorithms [55] and Tabu Search [56, 57].

Regardless of the underlying optimisation strategy there exist two major approaches in solving the multi-objective problem. The most common method is to reduce the multi objective to a single objective optimisation problem, by forming a composite objective function, through the use of a weighting sum of the individual objective functions [58]. The main disadvantage of this approach is that the weights must be pre-set and this inherently introduces the designer's

preconceptions about the relative trade-off between objectives. The second approach is to search directly for a set of design vectors that represent the optimal trade-off between the objective functions, known as the Pareto-optimal set. The advantage of the second approach is that the identification of the Pareto-optimal set, provides the designer with a clear picture of the achievable trade-offs between the competing objectives.

For the conduct of the multi-objective optimisation and the identification of the Pareto front, a variant of the Tabu Search (TS) algorithm, developed by Jaeggi et al. [59], was employed in the present work. TS comprises an optimiser that has been proved more effective than the Genetic Algorithm and Simulated Annealing methods when tested on a number of meta-heuristic methods on a representative single-objective aerodynamic design optimisation problem [60].

In 1986 Glover [56] postulated a new (meta-heuristic) approach, the Tabu Search, that enhances the performance of local search (heuristic) methods by overcoming local optima. In its essence, Tabu search is a meta-heuristic superimposed on another heuristic. The basic principle of the TS is to implement a local search strategy, however, when a local optimum is encountered a non-improving move is allowed. Key to the realisation of the TS is the use of short, medium and long term memories. The *Short-Term-Memory* (STM) records recent history and prevents the search from tracing back its steps; points stored in the STM are *Tabu* and are not accessed by subsequent searches. The *Medium-Term-Memory* (MTM), keeps an unbounded record of the generated Pareto-optimal points and is used for *search intensification* to reinforce attractive designs. The *Long-Term-Memory* (LTM) monitors the region of the explored design space and is accessed for *search diversification*, that is, directing the search into previously unexplored areas.

In 1997 Hansen [61] developed a multi-objective TS optimisation algorithm that extended the composite-objective approach. In specific, it performed several component objective Tabu searches in parallel. Every each one of them was characterized by different, dynamically updated set of weights that resulted in the exploration of the entire Pareto front. Nevertheless, and although Hansen's attempt stands as a good TS implementation, it is presented with problems that are common to all weight-sum approaches. In particular, when dealing with

Pareto fronts, problems are identified in non-convex regions of the front that are not defined by a combination of weights. Later on, in 1999 Baykasoglu et al. [62] developed a TS algorithm that combined a downhill local search with an intensification memory. Certain concerns, such as the fact that the search was restricted to downhill moves without a diversification strategy render the algorithm of Baykasoglu et al. to be more of an elaborate local search algorithm rather than a genuine TS algorithm.

On the other hand the multi-objective TS algorithm employed in this work is based on the single-objective TS implementation of Connor & Tilley [63]. It uses a Hooke and Jeeves [64] local search algorithm, coupled with short, medium and long term memories that are accessed to implement search intensification and diversification, according to Glover and Laguna [57]. A complete description of the TS algorithm can be found in Kipouros et al. [65], while the performance of the multi-objective TS on both unconstrained and constrained optimisation was presented in Jaeggi et al.[59, 66].

1.5 Aims and Objectives

In view of the above, the objectives of this thesis can now be outlined;

- Development of a robust high resolution CFD solver that will efficiently and accurately simulate various flow phenomena, such as shock/boundary layer interaction, flow separation and turbulence and also provide the numerical framework for analysis and aerodynamic design.
- Incorporation of the CFD solver with a state-of-the-art multi-objective optimisation algorithm, along with necessary parametrization and grid generation/deformation techniques, for the development of an integrated design system capable of generating feasible designs within the Active Camber flow control concept.
- Study of the effect that very high resolution schemes have in conjunction with two equation eddy viscosity models both in terms of analysis and optimisation.

Chapter 2

Mathematical Modelling of Turbulent flows

In this chapter the governing equations for the dynamics of a compressible fluid, such as air, along with closure conditions in the form of equations of state are presented. Meanwhile, there is no attempt to provide a rigorous derivation of the equations of classical continuum mechanics, since this is available in numerous CFD textbooks [1, 28, 30, 67, 68]. Instead a self-contained summary of the fluid flow equations and the thermodynamics is presented in a manner that it serves the development of the numerical method employed in the present work.

2.1 Governing equations - Laminar flow

The governing equations of motion for a continuous viscous fluid, such as air, are the time-dependent compressible Navier-Stokes equations. The Navier-Stokes equations represent the flow conservation laws of classical physics, namely conservation of mass (continuity), momentum and energy. The conservation laws in compact tensor notation are:

- Continuity equation:

$$\frac{\partial \rho}{\partial t} + \frac{\partial \left(\rho u_i\right)}{\partial x_i} = 0 \tag{2.1}$$

- Momentum equation

$$\frac{\partial(\rho u_i)}{\partial t} + \frac{\partial\left(\rho u_i u_j + p\delta_{ij} - \tau_{ij}^l\right)}{\partial x_i} = 0 \tag{2.2}$$

- Energy equation

$$\frac{\partial e}{\partial t} + \frac{\partial\left[\rho u_i (e+p) - u_i \tau_{ij}^l - q_i^l\right]}{\partial x_i} = 0 \tag{2.3}$$

Where ρ is the density of the fluid, u_i is the velocity vector, p is the pressure, e is the total energy, τ_{ij}^l and q_i^l are the molecular stress tensor and heat flux vector respectively, and δ_{ij} is the Kronecker delta function ($\delta_{ij} = 1$ if $i = j$ and $\delta_{ij} = 0$ if $i \neq j$).

The governing partial differential equation system (2.1) - (2.3) is incomplete, since there are more unknowns than equations. In order to properly describe the physical flow processes, constitute relations that describe the physical properties of the fluid under consideration, are incorporated. Thermodynamic equilibrium conditions, in the form of equations of state, provide the necessary additional closure equations. Since air can be considered as a thermally ideal gas, the thermal equation of state dictates that:

$$p = \rho R T \tag{2.4}$$

where R is the universal gas constant and T is the temperature of the fluid.

Meanwhile, the caloric equation of state relates the internal energy to temperature:

$$e_{in} = c_v T \tag{2.5}$$

where $e_{in}$is the internal energy and $c_v$is the specific heat at constant volume.

The thermal and caloric equations of state are closely related and are necessary for a complete description of the thermodynamic properties of the system. Furthermore, by combining Eq.'s (2.4) and (2.5), while noting that $R = (\gamma - 1)\, c_v$, a simple expression that relates internal energy, pressure and density is obtained for a calorically ideal gas:

$$e_{in} = \frac{p}{\rho(\gamma - 1)} \tag{2.6}$$

where γ is the specific heat ratio, $\gamma = \frac{c_p}{c_v}$, with c_p being the specific heat at constant pressure.

The total energy e consists of the internal e_{in} and the kinetic $\frac{1}{2}\rho u_i u_i$ energy of the fluid according to:

$$e = \rho e_{in} + \frac{1}{2}\rho u_i u_i. \tag{2.7}$$

By substituting Eq. (2.6) to the latter Eq. (2.7), a direct relation of pressure, total and kinetic energy is obtained:

$$e = \frac{p}{(\gamma - 1)} + \frac{1}{2}\rho u_i u_i \tag{2.8}$$

In defining the molecular viscous stress tensor τ_{ij}^l, the Newtonian approximation is employed, according to which the relationship between stress and strain rate is homogeneous and linear. This is given by:

$$\tau_{ij}^l = 2\mu S_{ij} + \lambda \frac{\partial u_k}{\partial x_k}\delta_{ij} \tag{2.9}$$

where $S_{ij} = \frac{1}{2}\left(\frac{\partial u_i}{\partial x_j} + \frac{\partial u_j}{\partial x_i}\right)$is the mean strain rate, μ and λ are the coefficients of molecular and bulk viscosity, respectively. The latter follows Stokes's hypothesis, according to which $\lambda = -\frac{2}{3}\mu$.

The molecular viscosity (μ)coefficient is modeled by Sutherland's law:

$$\frac{\mu}{\mu_0} \approx \left(\frac{T}{T_0}\right)^{\frac{3}{2}} \frac{T_0 + S}{T + S} \tag{2.10}$$

where the subscript 0 denotes a reference state, which is usually defined to be a freestream condition. Typically for air: $\mu_0 = 1.716E^{-5}\frac{Ns}{m^2}$, $T_0 = 273K$, $S = 110.5K$.

In a fashion similar to which the viscous stresses are related to the gradients of the velocity vector, the molecular heat flux vector can be linearly related to the temperature gradient via Fourier's heat conduction law:

$$q_i^l = -\kappa \frac{\partial T}{\partial x_i} \tag{2.11}$$

where κ is the heat conduction coefficient. Under the assumption that both the specific heat at constant pressure, c_p, and the laminar Prandtl number $Pr = \frac{\mu c_p}{Pr}$ are constant then the heat conduction coefficient can be directly determined. In fact, for air in the temperature range $200K \leq T \leq 1000K$, P_r can be considered to have a constant value of 0.7 [30]. The molecular heat flux can be therefore written as:

$$q_i^l = -\left(\frac{\mu c_p}{Pr}\right)\frac{\partial T}{\partial x_i} \tag{2.12}$$

2.2 Reynolds-Averaged Navier Stokes equations (RANS)

Turbulence is characterised by random fluctuations and as such a statistical approach can be used, according to which pressure and the velocity vectors are decomposed into the mean and fluctuating parts. This is known as the Reynolds decomposition. Following the procedure introduced by Reynolds [69], the instantaneous flow is expressed as the sum of the mean and the fluctuating component:

$$u_i = \overline{u_i} + u_i'. \tag{2.13}$$

Applying such an averaging to the nonlinear governing equations, results in additional momentum fluxes that include unknown quantities. These momentum fluxes act as turbulent stresses throughout the flow and are known as the Reynolds stresses.

Furthermore, for flows in which compressible effects are important, in addition to velocity and pressure, density and energy fluctuations must be also taken under consideration. This in its turn, leads to a turbulent heat-flux vector. Therefore, mass (Favre) averaging [70] is considered to be more consistent with the associated compressible flow physics, according to which the instantaneous velocity is decomposed to the mass averaged and fluctuating part:

$$u = \frac{\overline{\rho u}}{\overline{\rho}} + u" \tag{2.14}$$

where $\overline{\rho}$ is the convectional Reynolds-averaged density.

Following the mass averaging procedure described in detail in Wilcox [42], the Reynolds mass Averaged Navier-Stokes Eq.'s (2.1), (2.2), (2.3) for compressible fluids can be written as:

$$\frac{\partial \rho}{\partial t} + \frac{\partial (\rho u_i)}{\partial x_i} = 0 \tag{2.15}$$

$$\frac{\partial (\rho u_i)}{\partial t} + \frac{\partial (\rho u_i u_j + p\delta_{ij} - \tau_{ij})}{\partial x_j} = 0 \tag{2.16}$$

$$\frac{\partial e}{\partial t} + \frac{\partial [\rho u (e + p) - u_i \tau_{ij} - q_i]}{\partial x_i} = 0 \tag{2.17}$$

where the overbars have been dropped for simplicity.

In Eq.'s (2.15), (2.16), (2.17) ρ is the averaged density ($\rho \equiv \overline{\rho}$) and u_i is the averaged velocity vector ($u_i \equiv \overline{u_i}$).

Due to the averaging procedure, the total averaged energy e includes an extra term, the turbulent kinetic energy k:

$$e = \frac{p}{(\gamma - 1)} + \frac{1}{2}\rho u_i u_i + \rho k \tag{2.18}$$

The pressure is evaluated from:

$$p = (\gamma - 1)(e - \frac{1}{2}\rho(u^2 + w^2) - \rho k) \tag{2.19}$$

Moreover, the Reynolds mass Averaged Navier Stokes equations differ from their laminar counterparts by the appearance of the mass-averaged Reynolds-stresses, τ_{ij}^t, and the turbulent heat fluxes q_i^t. Therefore, the total stress tensor is written as:

$$\tau_{ij} = \tau_{ij}^l + \tau_{ij}^t \tag{2.20}$$

and the heat flux as:

$$q_i = q_i^l + q_i^t \tag{2.21}$$

In the context of two equation, linear, eddy viscosity modeling, the Reynolds stress tensor is modeled as a linear constitutive relation of the local mean strain rate and the two turbulence scale variables. This assumption is analogous to the Newtonian approximation for the laminar stress tensor, and although it is not universally applicable, it provides an adequate level of modeling for many applications. The most popular constitutive relation is the Boussinesq approximation with suitable generalizations for compressible flows:

$$\tau_{ij}^t = 2\mu_t S_{ij} - \frac{2}{3}\mu_t \frac{\partial u_k}{\partial x_k}\delta_{ij} - \frac{2}{3}\rho k \delta_{ij} \tag{2.22}$$

where k is the turbulence kinetic energy and μ_t is the turbulent viscosity.

The turbulence heat fluxes are modeled analogous to their laminar counterpart and thus it is assumed to be proportional to the mean temperature gradient.

$$q_i^t = -\left(\frac{\mu_t c_p}{Pr_t}\right)\frac{\partial T}{\partial x_i} \tag{2.23}$$

where Pr_t is the turbulent Prandtl number. A constant value of $Pr_t = 0.9$, in the case of a boundary layer, is considered satisfactory from subsonic up to low supersonic flows [42].

2.3 Linear Eddy Viscosity Modeling (LEVM)

Conceptually two equation turbulence models consist of two characteristic parts (a) the scale determining model and (b) the constitutive model. Instead of solving a transport equation for each stress component it is assumed that the Reynolds stress tensor is an algebraic function of the local mean flow velocities (gradients) and the two turbulent scale variables. In the case of LEVM, the constitutive relation is the Boussinesq approximation, as defined in Eq. (2.22). A transport equation is then solved for each of the two scale variables. The most common turbulent scales are the turbulent kinetic energy k and either the rate of turbulent dissipation ϵ or the specific rate of turbulent dissipation ω.

The $k-\epsilon$ model is probably the most widely known and extensively used LEVM. Although numerous versions of this model can be found in the literature, the main contributions are due to Jones and Launder [71] and Launder and Sharma [72]. The $k-\epsilon$ models provide adequate modeling for free shear layers flows with zero or small pressure gradients while they are less accurate for large adverse pressure gradients. The $k-\epsilon$ models are insensitive to freestream values of turbulence, however the models require explicit wall-damping functions

The $k-\omega$ two equation eddy-viscosity model has become a widely used turbulence model for wall-bounded, aerodynamic flow for two main reasons: (a) it does not require any wall-damping functions nor the computation of wall distances and (b) numerically, it is less stiff than $k-\epsilon$ models in the near wall region.

Besides the novel work of Kolmogorov [73], the cornerstone in the evolution of the $k-\omega$ eddy viscosity models is the $k-\omega$ model of Wilcox [42]. Later models developed by Menter [74] and Kok [75] are based on Wilcox's work. Wilcox's model is designed so as to be integrated down to the wall without any near-wall modifications and it has been shown to perform well in boundary layers under adverse pressure gradients. Nevertheless, Menter first observed that Wilcox's model suffers from sensitivity to the free-stream boundary value of ω. Due to this free-stream sensitivity, the use of this model is limited to fully turbulent internal flows.

Menter's $k-\omega$ Shear Stress Transport (SST) [76] model is probably one of the most popular turbulence models for aeronautical applications. Menter, eliminated the free-stream sensitivity of Wilcox's model by combining it with the Jones-Launder $k-\epsilon$ [71] model. This was achieved by recognizing that the ϵ transport equation could be transformed to the ω transport equation by variable substitution. Furthermore, a switching function was devised that effectively blends the robust and accurate formulation of the $k-\omega$ in the near-wall region with the free stream independence of the $k-\epsilon$ model in the far-field region. In addition, the model limits the eddy viscosity by coupling the shear stress with the turbulent kinetic energy. This reduces the amount of the generated eddy viscosity and thus favors separation under adverse pressure gradients. However, Menter's model requires the wall distance thus loosing one of the advantages of the $k-\omega$ family of two equation eddy viscosity models.

Relatively recently, Kok designed a $k-\omega$ model that resolves the free-stream dependence of Wilcox's model and shares the favorable near wall behavior of Menter's models, by using only one set of closure coefficients. Kok's model that combines relative simplicity without compromising accuracy, is an attractive option for aerodynamic applications and thus it is incorporated in this work and described below.

2.3.1 The TNT $k-\omega$ model

Kok's version of the $k-\omega$ model equations are given by:

$$\frac{\partial \rho k}{\partial t} + \frac{\partial \left(\rho k u_i\right)}{\partial x_i} = P_k - \beta^* \rho \omega k + \frac{\partial}{\partial x_i}\left[\left(\mu + \sigma_k \mu_t\right)\frac{\partial k}{\partial x_i}\right] \tag{2.24}$$

$$\frac{\partial \rho \omega}{\partial t} + \frac{\partial \left(\rho \omega u_i\right)}{\partial x_i} = P_\omega - \beta^* \rho \omega^2 + \frac{\partial}{\partial x_i}\left[\left(\mu + \sigma_\omega \mu_t\right)\frac{\partial \omega}{\partial x_i}\right] + C_D \tag{2.25}$$

where ω is the specific turbulent dissipation and the eddy viscosity coefficient is defined as:

$$\mu_t = \frac{\rho k}{\omega} \tag{2.26}$$

The production and cross-diffusion terms are given by:

$$P_k = \tau_{ij}^t \frac{\partial u_i}{\partial x_j} \tag{2.27}$$

$$P_\omega = \frac{\alpha_\omega \omega}{k} P_k \tag{2.28}$$

and

$$C_D = \sigma_d \frac{\rho}{\omega} max\left\{\frac{\partial k}{\partial x_i}\frac{\partial \omega}{\partial x_i}, 0\right\} \tag{2.29}$$

It is noteworthy that Kok's model equations include the cross-diffusion term that essentially switches from $k-\omega$ to $k-\epsilon$ when approaching the boundary-layer

edge. However, no blending functions are introduced, instead the model's closure coefficients are re-calibrated.

According to Wilcox [42] in order to be consistent with the experimental decay of the turbulent kinetic energy for homogeneous, isotropic turbulence, $\frac{\beta}{\beta^*} = \frac{6}{5}$. Also to obtain the correct solution in the inner layer of a constant-pressure boundary layer, consistent with the law of the wall, $\alpha_\omega = \frac{\beta}{\beta^*} - \frac{\sigma_\omega \kappa^2}{\sqrt{\beta^*}}$ (with $\kappa = 0.41$ being the Von Kármán constant), and $\beta^* = 0.09$, while $\sigma_\omega = 0.5$ or otherwise a low-Reynolds-number modification is needed [75].

For the two remaining diffusion coefficients, Kok performed a turbulent/ non turbulent (TNT) analysis based on a set of 1D diffusion equations that modeled free-stream edges of turbulent regions. The values $\sigma_k = \frac{2}{3}$ *and* $\sigma_d = 0.5$ satisfied the constraints of his TNT analysis. Table 2.1 summarizes the closure coefficients:

$\beta^* =$	0.09
$\beta =$	0.075
$\sigma_\omega =$	0.5
$\sigma_k =$	$\frac{2}{3}$
$\sigma_d =$	0.5
$\alpha_\omega =$	$\frac{\beta}{\beta^*} - \frac{\sigma_\omega \kappa^2}{\sqrt{\beta^*}}$

Table 2.1: The TNT set of closure coefficients for the $k - \omega$ model.

2.3.2 Turbulent Boundary Conditions

At a no slip wall, the obvious boundary condition is to set the turbulent kinetic energy to zero. However, the boundary condition for the specific rate of turbulent dissipation is quite ambiguous since at solid boundaries, ω tends to infinity. In this work, ω is determined following a proposition of Menter [74], and is set to:

$$\omega = 10 \frac{6\mu}{\beta \rho y^2} \tag{2.30}$$

where y is the normal distance of the first cell center off the wall. According to Menter the results are not sensitive to the factor (10), while it should be noted that models based on the ω transport equation produce accurate results, when the near wall values of ω_w are sufficiently large.

A common approach for the specification of the turbulent kinetic energy at the far field boundaries is to define the level of free-stream turbulence as a percentage of the mean kinetic energy of the fluid, according to the relation:

$$k_\infty = \frac{3}{2}\left(TI \cdot u_\infty\right)^2 \tag{2.31}$$

where TI is the turbulent intensity. Having specified $k_\infty$the free-stream turbulent Reynolds number $Re_{t\infty} = (\mu_t/\mu)_\infty$ needs to be specified as well, in order to determine the free-stream specific dissipation rate $\omega_\infty$from Eq. (2.26). At the outflow boundary a zero gradient of the turbulence quantities is assumed.

2.4 Governing equation - Matrix form

The transport equations for the two scale variables of the turbulence model are solved in conjunction with the Navier Stokes averaged equations. In order to facilitate the development of numerical schemes the resulting system of the conservative Navier-Stokes equations in Cartesian 2D co-ordinates, are written in a compact vector-variable form:

$$\frac{\partial \tilde{\mathbf{U}}}{\partial t} + \frac{\partial \tilde{\mathbf{F}}}{\partial x} + \frac{\partial \tilde{\mathbf{G}}}{\partial z} = \frac{\partial \tilde{\mathbf{R}}}{\partial x} + \frac{\partial \tilde{\mathbf{S}}}{\partial z} + \tilde{\mathbf{H}} \tag{2.32}$$

In the above relation $\tilde{\mathbf{U}}$ is the solution vector of the conservative variables, $\tilde{\mathbf{E}}$, $\tilde{\mathbf{G}}$ and $\tilde{\mathbf{R}}$, $\tilde{\mathbf{S}}$ are the inviscid and viscous Cartesian flux vectors, respectively, while H represents the turbulent source vector. It follows that:

$$\tilde{\mathbf{U}} = (\rho, \rho u, \rho w, e, k, \omega)^T \tag{2.33}$$

$$\tilde{\mathbf{F}}(\tilde{\mathbf{U}}) = \begin{bmatrix} \rho u \\ \rho u^2 + p \\ \rho u w \\ u\,(e+p) \\ \rho u k \\ \rho u \omega \end{bmatrix},\ \tilde{\mathbf{G}}(\tilde{\mathbf{U}}) = \begin{bmatrix} \rho w \\ \rho u w \\ \rho w^2 + p \\ w\,(e+p) \\ \rho w k \\ \rho w \omega \end{bmatrix} \tag{2.34}$$

$$\tilde{\mathbf{R}}(\tilde{\mathbf{U}}) = \begin{bmatrix} 0 \\ \tau_{xx} \\ \tau_{xz} \\ u\tau_{xx} + w\tau_{xz} - q_x \\ (\mu + \sigma_k \mu_t) \frac{\partial k}{\partial x} \\ (\mu + \sigma_\omega \mu_t) \frac{\partial \omega}{\partial x} \end{bmatrix}, \; \tilde{\mathbf{S}}(\tilde{\mathbf{U}}) = \begin{bmatrix} 0 \\ \tau_{zx} \\ \tau_{zz} \\ u\tau_{zx} + w\tau_{zz} - q_z \\ (\mu + \sigma_k \mu_t) \frac{\partial k}{\partial z} \\ (\mu + \sigma_\omega \mu_t) \frac{\partial \omega}{\partial z} \end{bmatrix} \tag{2.35}$$

and

$$\tilde{\mathbf{H}} = \begin{bmatrix} 0 \\ 0 \\ 0 \\ 0 \\ P_k - \beta^* \rho \omega k \\ P_\omega - \beta \rho \omega^2 + C_D \end{bmatrix} \tag{2.36}$$

Due to the Boussinesq assumption the stress tensors include terms of $-\frac{2}{3}\rho k$. Some researchers ignore the turbulent kinetic energy contribution to the total energy and the momentum equations. However, in this work it was decided to include these terms since this is in a better accordance to physical reasoning and the averaging procedure. Moving these terms to the LHS and redefining $\tau_{ij} = \tau_{i,j} + \frac{2}{3}\rho k \delta_{ij}$, so that the stresses are free from the turbulent kinetic energy terms, the inviscid fluxes are modified as:

$$\tilde{\mathbf{F}}(\tilde{\mathbf{U}}) = \begin{bmatrix} \rho u \\ \rho u^2 + p_t \\ \rho u w \\ u\left(e + p_t\right) \\ \rho u k \\ \rho u \omega \end{bmatrix}, \; \tilde{\mathbf{G}}(\tilde{\mathbf{U}}) = \begin{bmatrix} \rho w \\ \rho u w \\ \rho w^2 + p_t \\ w\left(e + p_t\right) \\ \rho w k \\ \rho w \omega \end{bmatrix} \tag{2.37}$$

where p_t is the turbulent pressure, as suggested by Hirsch [77], Venkateswaran and Merkle [78] and Lee and Choi [79]:

$$p_t = p + \frac{2}{3}\rho k \tag{2.38}$$

The total averaged energy e now reads:

$$e = \frac{p_t}{\gamma - 1} + \rho\frac{u^2 + w^2}{2} + \mathbf{C}\rho k \tag{2.39}$$

where the parameter $\mathbf{C} = \frac{3\gamma-5}{3(\gamma-1)}$.

As will be seen in Chapter 3 the inclusion of the turbulent kinetic energy and the definition of the turbulent pressure p_t affects the eigenvalues of the system.

Chapter 3

NUMERICAL IMPLEMENTATION

This chapter details the development of the numerical methodologies implemented in the present work. The governing equations are non-dimensionalised and transformed to a generalised curvilinear co-ordinate system in order to enhance both efficiency and accuracy. The fundamental feature for the calculation of the inviscid fluxes is a modified HLLC Riemann solver, that properly accounts for the turbulence transport quantities. Up to fifth order accuracy in space is achieved by employing different reconstruction schemes for the inviscid fluxes, while the viscous terms are centrally discretised to second order. Time integration is performed by a Newton method that solves the unfactored implicit equations. The implicit operator is constructed through the implementation of the flux vector splitting method of Steger-Warming along with contributions resulting from the thin layer viscous Jacobians and the turbulence source terms Jacobian. Convergence to steady state is accelerated with a point Gauss-Seidel relaxation technique.

3.1 NON-DIMENSIONALISATION

The equations of fluid motion are non-dimensionalised so as to obtain similarity for geometrically similar situations. The non-dimensionalisation process provides a direct comparison of values with experimental data and tends to bound the

variables between zero and one. Generally, a characteristic dimension, such as the chord of an aerofoil is selected to non-dimensionalise the independent spatial variables, while reference conditions are used to non-dimensionalise the dependent variables. Amongst many available choices, characteristic values for length l_c, velocity $\overrightarrow{u}_c$, density ρ_c, temperature T_c and viscosity μ_c are considered for non-dimensionalising the fluid flow variables. In this work, the characteristic velocity and temperature are designed to satisfy a modified caloric equation of state according to which:

$$e_\infty = \rho_c c_v T_c = \rho_c u_c^2 \tag{3.1}$$

The characteristic density ρ_c is chosen to be the free-stream density, i.e., $\rho_c = \rho_\infty$.

From Eq. (3.1) it simply follows that:

$$T_c = \frac{u_c^2}{c_v} \tag{3.2}$$

Combining Eq.'s (3.1) and (2.17), the characteristic velocity can be defined as:

$$u_c = s_\infty \sqrt{\frac{1 + 0.5 M_\infty^2 \gamma \left(\gamma - 1\right) \left(1 + 3\mathbf{C}TI^2\right)}{\gamma \left(\gamma - 1\right)}} \tag{3.3}$$

where $s_\infty = \sqrt{\gamma p_\infty / \rho_\infty}$ and M_∞ are respectively the free-stream speed of sound and Mach number.

The Reynolds number is defined as:

$$Re = \frac{\rho_\infty u_\infty l_c}{\mu_\infty} = \frac{\rho_c u_c l_c}{\mu_c} \tag{3.4}$$

from which the characteristic molecular viscosity μ_c is given to be:

$$\mu_c = \mu_\infty \frac{u_c}{u_\infty} \tag{3.5}$$

Having defined the characteristic variables, the dimensionless dependent variables are given below:

$$t^* = \frac{tu_c}{l_c}, \quad x^* = \frac{x}{l_c}, \quad z^* = \frac{z}{l_c}, \quad \mu^* = \frac{\mu}{\mu_c}$$

$$\rho^* = \frac{\rho}{\rho_c}, \quad u^* = \frac{u}{u_c}, \quad w^* = \frac{w}{u_c}, \quad p^* = \frac{p}{\rho_c u_c^2}$$

$$e^* = \frac{e}{\rho_c u_c^2}, \quad T^* = \frac{T}{T_c}, \quad k^* = \frac{k}{u_c^2}, \quad \omega^* = \frac{\omega l_c}{Re u_c}$$

For consistency purposes and in order to provide a direct comparison against experimental data or other computational results, the non-dimensionalisation of the free-stream variables is essential.

Accordingly, the free-stream values are defined as:

- Free-stream Velocity:

$$u_\infty^* = \frac{u_\infty}{u_c} = \sqrt{\frac{\gamma\left(\gamma-1\right)M_\infty^2}{1+0.5M_\infty^2\gamma\left(\gamma-1\right)\left(1+3\mathbf{C}TI^2\right)}} \tag{3.6}$$

- Free-stream Turbulent Pressure:

$$p_{t\infty}^* = \frac{p_{t\infty}}{\rho_c u_c^2} = \frac{u_\infty^{*2}}{\gamma M_\infty^2} \tag{3.7}$$

- Free-stream Temperature:

$$T_\infty^* = \frac{T_\infty}{T_c} = \frac{p_{t\infty}^*}{\left(\gamma-1\right)} \tag{3.8}$$

- Free-stream Viscosity:

The dimensionless viscosity follows directly from Eq. (3.5):

$$\mu_\infty^* = \frac{\mu_\infty}{\mu_c} \tag{3.9}$$

Using the the dimensionless variables, the RANS equations are expressed as:
Continuity equation :

$$\frac{\partial \rho^*}{\partial t^*} + \frac{\partial}{\partial x^*}\left(\rho^* u^*\right) + \frac{\partial}{\partial z^*}\left(\rho^* w^*\right) = 0 \tag{3.10}$$

X-component of the Momentum equation:

$$\frac{\partial}{\partial t^*}\left(\rho^* u^*\right) + \frac{\partial}{\partial x^*}\left(\rho^* u^{*2} + p_t^*\right) + \frac{\partial}{\partial z^*}\left(\rho^* u^* w^*\right) = \frac{\partial}{\partial x^*}\left(\tau_{xx}^*\right) + \frac{\partial}{\partial z^*}\left(\tau_{xz}^*\right) \tag{3.11}$$

where the x-component of the normal stress is:

$$\tau_{xx}^* = \frac{2}{3}\frac{1}{Re}\left(\mu^* + \mu_t^*\right)\left(2\frac{\partial u^*}{\partial x^*} - \frac{\partial w^*}{\partial z^*}\right) - \frac{2}{3}\rho^* k^* \tag{3.12}$$

and the shear stress:

$$\tau_{xz}^* = \tau_{zx}^* = \frac{1}{Re}\left(\mu^* + \mu_t^*\right)\left(\frac{\partial u^*}{\partial z^*} + \frac{\partial w^*}{\partial x^*}\right) \tag{3.13}$$

Similarly,

Z - component of the Momentum equation:

$$\frac{\partial}{\partial t^*}\left(\rho^* w^*\right) + \frac{\partial}{\partial x^*}\left(\rho^* u^* w^*\right) + \frac{\partial}{\partial z^*}\left(\rho^* w^{*2} + p_t^*\right) = \frac{\partial}{\partial x^*}\left(\tau_{zx}^*\right) + \frac{\partial}{\partial z^*}\left(\tau_{zz}^*\right) \tag{3.14}$$

where the z-component of the normal stress is:

$$\tau_{zz}^* = \frac{2}{3}\frac{1}{Re}\left(\mu^* + \mu_t^*\right)\left(2\frac{\partial w^*}{\partial z^*} - \frac{\partial u^*}{\partial x^*}\right) - \frac{2}{3}\rho^* k^* \tag{3.15}$$

Energy equation:

$$\frac{\partial e^*}{\partial t^*} + \frac{\partial}{\partial x^*}\left[u^*\left(e^* + p_t^*\right)\right] + \frac{\partial}{\partial z^*}\left[w^*\left(e^* + p_t^*\right)\right] = \frac{\partial}{\partial x^*}\left(u^*\tau_{xx}^* + w^*\tau_{zx}^* - q_x^*\right) + \frac{\partial}{\partial z^*}\left(u^*\tau_{xz}^* + w^*\tau_{zz}^* - q_z^*\right) \tag{3.16}$$

where the heat flux components are:

$$-q_x^* = \frac{1}{Re}\left(\mu^*\frac{\gamma}{Pr} + \mu_t^*\frac{\gamma}{Pr_\tau}\right)\frac{\partial T^*}{\partial x^*} \tag{3.17}$$

and

$$-q_z^* = \frac{1}{Re}\left(\mu^* \frac{\gamma}{Pr} + \mu_t^* \frac{\gamma}{Pr_\tau}\right)\frac{\partial T^*}{\partial z^*} \tag{3.18}$$

Turbulent kinetic energy transport equation:

$$\frac{\partial}{\partial t^*}\left(\rho^* k^*\right) + \frac{\partial}{\partial x^*}\left(\rho^* u^* k^*\right) + \frac{\partial}{\partial z^*}\left(\rho^* w^* k^*\right) =$$

$$\frac{\partial}{\partial x^*}\left[\frac{1}{Re}\left(\mu^* + \sigma_\kappa \mu_t^*\right)\frac{\partial k^*}{\partial x^*}\right] + \frac{\partial}{\partial z^*}\left[\frac{1}{Re}\left(\mu^* + \sigma_\kappa \mu_t^*\right)\frac{\partial k^*}{\partial z^*}\right] + P_k^* - Re\beta^*\rho^*\omega^* k^* \tag{3.19}$$

the dimensionless turbulent kinetic energy production term is:

$$P_k^* = \tau_{xx}^{*t}\frac{\partial u^*}{\partial x^*} + \tau_{zx}^{*t}\frac{\partial u^*}{\partial z^*} + \tau_{xz}^{*t}\frac{\partial w^*}{\partial x^*} + \tau_{zz}^{*t}\frac{\partial w^*}{\partial z^*} \tag{3.20}$$

with the normal and shear Reynolds stresses:

$$\tau_{xx}^{*t} = \frac{2}{3}\left[\frac{1}{Re}\mu_t^*\left(2\frac{\partial u^*}{\partial x^*} - \frac{\partial w^*}{\partial z^*}\right) - \rho^* k^*\right] \tag{3.21}$$

$$\tau_{zz}^{*t} = \frac{2}{3}\left[\frac{1}{Re}\mu_t^*\left(2\frac{\partial w^*}{\partial z^*} - \frac{\partial u^*}{\partial x^*}\right) - \rho^* k^*\right] \tag{3.22}$$

$$\tau_{xz}^{*t} = \tau_{zx}^{*t} = \mu_t^* \frac{1}{Re}\left(\frac{\partial u^*}{\partial z^*} + \frac{\partial w^*}{\partial x^*}\right) \tag{3.23}$$

Specific rate of turbulent dissipation, transport equation:

$$\frac{\partial}{\partial t^*}\left(\rho^* \omega^*\right) + \frac{\partial}{\partial x^*}\left(\rho^* u^* \omega^*\right) + \frac{\partial}{\partial z^*}\left(\rho^* w^* \omega^*\right) =$$

$$\frac{\partial}{\partial x^*}\left[\frac{1}{Re}\left(\mu^* + \sigma_\omega \mu_t^*\right)\frac{\partial \omega^*}{\partial x^*}\right] + \frac{\partial}{\partial z^*}\left[\frac{1}{Re}\left(\mu^* + \sigma_\omega \mu_t^*\right)\frac{\partial \omega^*}{\partial z^*}\right] + P_\omega^* - Re\beta\rho^*\omega^{*2} + C_D^* \tag{3.24}$$

where the dimensionless production term is:

$$P_\omega^* = \frac{a_\omega \omega^*}{k^*} P_k^* \tag{3.25}$$

and the dimensionless cross-diffusion term reads:

$$C_D^* = \sigma_d \frac{\rho^*}{Re\omega^*} max\left\{\frac{\partial k^*}{\partial x^*}\frac{\partial w^*}{\partial x^*} + \frac{\partial k^*}{\partial z^*}\frac{\partial w^*}{\partial z^*},\ 0\right\} \tag{3.26}$$

The dimensionless conservative Navier-Stokes equations in Cartesian co-ordinates, in conjunction with the two-equation TNT $k-\omega$ eddy viscosity model can now be written in a compact vector-variable form, where the star superscript (*) has been omitted for simplicity:

$$\frac{\partial \tilde{\mathbf{U}}}{\partial t} + \frac{\partial \tilde{\mathbf{F}}}{\partial x} + \frac{\partial \tilde{\mathbf{G}}}{\partial z} = \frac{\partial \tilde{\mathbf{R}}}{\partial x} + \frac{\partial \tilde{\mathbf{S}}}{\partial z} + \tilde{\mathbf{H}} \tag{3.27}$$

where:

$$\tilde{\mathbf{U}} = \begin{bmatrix} \rho \\ \rho u \\ \rho w \\ e \\ \rho k \\ \rho \omega \end{bmatrix},$$

$$\tilde{\mathbf{F}}(\tilde{\mathbf{U}}) = \begin{bmatrix} \rho u \\ \rho u^2 + p_t \\ \rho u w \\ u\left(e + p_t\right) \\ \rho u k \\ \rho u \omega \end{bmatrix},\ \tilde{\mathbf{G}}(\tilde{\mathbf{U}}) = \begin{bmatrix} \rho w \\ \rho u w \\ \rho w^2 + p_t \\ w\left(e + p_t\right) \\ \rho w k \\ \rho w \omega \end{bmatrix}$$

$$\tilde{\mathbf{R}}(\tilde{\mathbf{U}}) = \begin{bmatrix} 0 \\ \tau_{xx} \\ \tau_{xz} \\ u\tau_{xx} + w\tau_{xz} - q_x \\ \frac{1}{Re}\left(\mu + \sigma_k \mu_t\right)\frac{\partial k}{\partial x} \\ \frac{1}{Re}\left(\mu + \sigma_\omega \mu_t\right)\frac{\partial \omega}{\partial x} \end{bmatrix},\ \tilde{\mathbf{S}}(\tilde{\mathbf{U}}) = \begin{bmatrix} 0 \\ \tau_{zx} \\ \tau_{zz} \\ u\tau_{zx} + w\tau_{zz} - q_z \\ \frac{1}{Re}\left(\mu + \sigma_k \mu_t\right)\frac{\partial k}{\partial z} \\ \frac{1}{Re}\left(\mu + \sigma_\omega \mu_t\right)\frac{\partial \omega}{\partial z} \end{bmatrix}$$

$$\tilde{\mathbf{H}} = \begin{bmatrix} 0 \\ 0 \\ 0 \\ 0 \\ P_k - Re\beta^*\rho\omega k \\ P_\omega - Re\beta\rho\omega^2 + C_D \end{bmatrix}$$

3.2 Transformation to Generalized Curvilinear Co-ordinates

To enhance the efficiency and accuracy of the numerical scheme, the governing equations expressed in the 2D Cartesian coordinate system ($x,\ z$) are transformed from the physical space to the computational space. The transformation is such that the resulting computational domain is a rectangular uniform grid system.

The generalized coordinate transformation can be defined as:

$$\begin{gathered} \xi = \xi(x, z, t) \\ \zeta = \zeta(x, z, t) \\ t = t \end{gathered}$$

Applying the chain rule of differentiation:

$$\frac{\partial}{\partial x} = \xi_x \frac{\partial}{\partial \xi} + \zeta_x \frac{\partial}{\partial \zeta} + t_x \frac{\partial}{\partial t} \tag{3.28}$$

$$\frac{\partial}{\partial z} = \xi_z \frac{\partial}{\partial \xi} + \zeta_z \frac{\partial}{\partial \zeta} + t_z \frac{\partial}{\partial t} \tag{3.29}$$

$$\frac{\partial}{\partial t} = \xi_t \frac{\partial}{\partial \xi} + \zeta_t \frac{\partial}{\partial \zeta} + t_t \frac{\partial}{\partial t} \tag{3.30}$$

The total differentials of the Cartesian coordinates are:

$$dx = x_\xi d\xi + x_\zeta d\zeta + x_\tau dt$$

$$dz = z_\xi d\xi + z_\zeta d\zeta + z_\tau dt$$

$$dt = t_\xi d\xi + t_\zeta d\zeta + t_\tau dt$$

Noting that $t_\tau = 1$ and $t_\xi = t_\zeta = t_x = t_z = 0$, while for a non moving mesh $x_t = z_t = 0$. The Cartesian co-ordinate differentials can be written in matrix form, :

$$\begin{bmatrix} dx \\ dz \\ dt \end{bmatrix} = \begin{bmatrix} x_\xi & x_\zeta & 0 \\ z_\xi & z_\zeta & 0 \\ 0 & 0 & 1 \end{bmatrix} \begin{bmatrix} d\xi \\ d\zeta \\ dt \end{bmatrix}$$

or

$$\begin{bmatrix} d\xi \\ d\zeta \\ dt \end{bmatrix} = \begin{bmatrix} x_\xi & x_\zeta & 0 \\ z_\xi & z_\zeta & 0 \\ 0 & 0 & 1 \end{bmatrix}^{-1} \begin{bmatrix} dx \\ dz \\ dt \end{bmatrix} \tag{3.31}$$

similarly, the differentials of the Generalized coordinates are:

$$d\xi = \xi_x dx + \xi_z dz + \xi_t dt$$

$$d\zeta = \zeta_x dx + \zeta_z dz + \zeta_t dt$$

$$dt = t_x dx + t_z dz + t_t dt$$

For a non deforming mesh, the time metrics are equal to zero $\xi_t = \zeta_t = 0$, or in matrix form:

$$\begin{bmatrix} d\xi \\ d\zeta \\ dt \end{bmatrix} = \begin{bmatrix} \xi_x & \xi_z & 0 \\ \zeta_x & \zeta_z & 0 \\ 0 & 0 & 1 \end{bmatrix} \begin{bmatrix} dx \\ dz \\ dt \end{bmatrix} \tag{3.32}$$

By comparing Eq.'s (3.31) and (3.32) it is evident that:

$$\begin{bmatrix} \xi_x & \xi_z & 0 \\ \zeta_x & \zeta_z & 0 \\ 0 & 0 & 1 \end{bmatrix} = \begin{bmatrix} x_\xi & x_\zeta & 0 \\ z_\xi & z_\zeta & 0 \\ 0 & 0 & 1 \end{bmatrix}^{-1} = \frac{1}{J} \begin{bmatrix} z_\zeta & -x_\zeta & 0 \\ -z_\xi & x_\xi & 0 \\ 0 & 0 & 1 \end{bmatrix}$$

the determinant of which is defined as the geometric Jacobian of the inverse transformation, noted in this work as J, i.e.,

$$J = \frac{\partial\left(x,\ z\right)}{\partial\left(\xi,\ \zeta\right)} = \begin{vmatrix} x_\xi & x_\zeta & x_\tau \\ z_\xi & z_\zeta & z_\tau \\ 0 & 0 & 1 \end{vmatrix}^{-1} = x_\xi z_\zeta - x_\zeta z_\xi \tag{3.33}$$

Therefore, the transformation metrics are:

$$\xi_x = \frac{1}{J} z_\zeta \tag{3.34}$$

$$\xi_z = -\frac{1}{J} x_\zeta \tag{3.35}$$

$$\zeta_x = -\frac{1}{J} z_\xi \tag{3.36}$$

$$\zeta_z = \frac{1}{J} x_\xi \tag{3.37}$$

3.2.1 Transformation of the Fluid Flow equations in 2D

The transformation of the governing equation is performed by multiplying Eq. (3.27) with the geometric Jacobian and expanding the spatial partial differentials as:

$$J\frac{\partial \tilde{\mathbf{U}}}{\partial t} + J\left(\frac{\partial \tilde{\mathbf{F}}}{\partial \xi}\xi_x + \frac{\partial \tilde{\mathbf{F}}}{\partial \zeta}\zeta_x\right) + J\left(\frac{\partial \tilde{\mathbf{G}}}{\partial \xi}\xi_z + \frac{\partial \tilde{\mathbf{G}}}{\partial \zeta}\zeta_z\right) =$$

$$J\left(\frac{\partial \tilde{\mathbf{R}}}{\partial \xi}\xi_x + \frac{\partial \tilde{\mathbf{R}}}{\partial \zeta}\zeta_x\right) + J\left(\frac{\partial \tilde{\mathbf{S}}}{\partial \xi}\xi_z + \frac{\partial \tilde{\mathbf{S}}}{\partial \zeta}\zeta_z\right) + J\tilde{\mathbf{H}}$$

by collecting common terms:

$$\begin{aligned} &\frac{\partial J\tilde{\mathbf{U}}}{\partial t} + \frac{\partial}{\partial \xi}\left(J\xi_x\tilde{\mathbf{F}} + J\xi_z\tilde{\mathbf{G}}\right) + \frac{\partial}{\partial \zeta}\left(J\zeta_x\tilde{\mathbf{F}} + J\zeta_z\tilde{\mathbf{G}}\right) = \\ &\frac{\partial}{\partial \xi}\left(J\xi_x\tilde{\mathbf{R}} + J\xi_z\tilde{\mathbf{S}}\right) + \frac{\partial}{\partial \zeta}\left(J\zeta_x\tilde{\mathbf{R}} + J\zeta_z\tilde{\mathbf{S}}\right) + J\tilde{\mathbf{H}} \end{aligned} \tag{3.38}$$

Since the geometric Jacobian is directly related to the metrics, one may wish to denote:

$$\begin{array}{c} \hat{\xi_x} = J\xi_x,\ \hat{\xi_z} = J\xi_z \\ \hat{\zeta_x} = J\zeta_x,\ \hat{\zeta_z} = J\zeta_z \end{array} \tag{3.39}$$

and Eq. (3.38) becomes:

$$\begin{array}{c} \dfrac{\partial J\tilde{\mathbf{U}}}{\partial t} + \dfrac{\partial}{\partial \xi}\left(\hat{\xi_x}\tilde{\mathbf{F}} + \hat{\xi_z}\tilde{\mathbf{G}}\right) + \dfrac{\partial}{\partial \zeta}\left[\hat{\zeta_x}\tilde{\mathbf{F}} + \hat{\zeta_z}\tilde{\mathbf{G}}\right] = \\ \dfrac{\partial}{\partial \xi}\left(\hat{\xi_x}\tilde{\mathbf{R}} + \hat{\xi_z}\tilde{\mathbf{S}}\right) + \dfrac{\partial}{\partial \zeta}\left(\hat{\zeta_x}\tilde{\mathbf{R}} + \hat{\zeta_z}\tilde{\mathbf{S}}\right) + J\tilde{\mathbf{H}} \end{array} \tag{3.40}$$

By further denoting:

$$\mathbf{U} = J\tilde{\mathbf{U}},\ \mathbf{H} = J\tilde{\mathbf{H}} \tag{3.41}$$

$$\mathbf{F} = \left(\hat{\xi_x}\tilde{\mathbf{F}} + \hat{\xi_z}\tilde{\mathbf{G}}\right),\ \mathbf{G} = \left(\hat{\zeta_x}\tilde{\mathbf{F}} + \hat{\zeta_z}\tilde{\mathbf{G}}\right) \tag{3.42}$$

$$\mathbf{R} = \left(\hat{\xi_x}\tilde{\mathbf{R}} + \hat{\xi_z}\tilde{\mathbf{S}}\right),\ \mathbf{S} = \left(\hat{\zeta_x}\tilde{\mathbf{R}} + \hat{\zeta_z}\tilde{\mathbf{S}}\right) \tag{3.43}$$

the governing equations can be written in a compact vector variable form, similar to Eq. (3.27) as:

$$\frac{\partial \mathbf{U}}{\partial t} + \frac{\partial \mathbf{F}}{\partial \xi} + \frac{\partial \mathbf{G}}{\partial \zeta} = \frac{\partial \mathbf{R}}{\partial \xi} + \frac{\partial \mathbf{S}}{\partial \zeta} + \mathbf{H} \tag{3.44}$$

For completeness, the components of the fluxes are given explicitly as:

$$\mathbf{F} = \begin{bmatrix} \rho\left(u\hat{\xi_x} + w\hat{\xi_z}\right) \\ \rho u\left(u\hat{\xi_x} + w\hat{\xi_z}\right) + p_t\hat{\xi_x} \\ \rho w\left(u\hat{\xi_x} + w\hat{\xi_z}\right) + p_t\hat{\xi_z} \\ (e + p_t)\left(u\hat{\xi_x} + w\hat{\xi_z}\right) \\ \rho k\left(u\hat{\xi_x} + w\hat{\xi_z}\right) \\ \rho\omega\left(u\hat{\xi_x} + w\hat{\xi_z}\right) \end{bmatrix} \tag{3.45}$$

$$\mathbf{G} = \begin{bmatrix} \rho\left(u\hat{\zeta_x} + w\hat{\zeta_z}\right) \\ \rho u\left(u\hat{\zeta_x} + w\hat{\zeta_z}\right) + p_t\hat{\zeta_x} \\ \rho w\left(u\hat{\zeta_x} + w\hat{\zeta_z}\right) + p_t\hat{\zeta_z} \\ (e+p_t)\left(u\hat{\zeta_x} + w\hat{\zeta_z}\right) \\ \rho k\left(u\hat{\zeta_x} + w\hat{\zeta_z}\right) \\ \rho\omega\left(u\hat{\zeta_x} + w\hat{\zeta_z}\right) \end{bmatrix} \tag{3.46}$$

$$\mathbf{R} = \begin{bmatrix} 0 \\ \tau_{xx}\hat{\xi_x} + \tau_{zx}\hat{\xi_z} \\ \tau_{xz}\hat{\xi_x} + \tau_{zz}\hat{\xi_z} \\ u\tau_{xx}\hat{\xi_x} + w\tau_{xz}\hat{\xi_x} - q_x\hat{\xi_x} + u\tau_{zx}\hat{\xi_z} + w\tau_{zz}\hat{\xi_z} - q_z\hat{\xi_z} \\ \frac{1}{Re}\left(\mu + \sigma_\kappa\mu_t\right)\frac{1}{J}\left[\frac{\partial k}{\partial\xi}\left(\hat{\xi_x}\hat{\xi_x} + \hat{\xi_z}\hat{\xi_z}\right) + \frac{\partial k}{\partial\zeta}\left(\hat{\zeta_x}\hat{\xi_x} + \hat{\zeta_z}\hat{\xi_z}\right)\right] \\ \frac{1}{Re}\left(\mu + \sigma_\omega\mu_t\right)\frac{1}{J}\left[\frac{\partial \omega}{\partial\xi}\left(\hat{\xi_x}\hat{\xi_x} + \hat{\xi_z}\hat{\xi_z}\right) + \frac{\partial \omega}{\partial\zeta}\left(\hat{\zeta_x}\hat{\xi_x} + \hat{\zeta_z}\hat{\xi_z}\right)\right] \end{bmatrix} \tag{3.47}$$

$$\mathbf{S} = \begin{bmatrix} 0 \\ \tau_{xx}\hat{\zeta_x} + \tau_{zx}\hat{\zeta_z} \\ \tau_{xz}\hat{\zeta_x} + \tau_{zz}\hat{\zeta_z} \\ u\tau_{xx}\hat{\zeta_x} + w\tau_{xz}\hat{\zeta_x} - q_x\hat{\zeta_x} + u\tau_{zx}\hat{\zeta_z} + w\tau_{zz}\hat{\zeta_z} - q_z\hat{\zeta_z} \\ \frac{1}{Re}\left(\mu + \sigma_\kappa\mu_t\right)\frac{1}{J}\left[\frac{\partial k}{\partial\xi}\left(\hat{\xi_x}\hat{\zeta_x} + \hat{\xi_z}\hat{\zeta_z}\right) + \frac{\partial k}{\partial\zeta}\left(\hat{\zeta_x}\hat{\zeta_x} + \hat{\zeta_z}\hat{\zeta_z}\right)\right] \\ \frac{1}{Re}\left(\mu + \sigma_\omega\mu_t\right)\frac{1}{J}\left[\frac{\partial \omega}{\partial\xi}\left(\hat{\xi_x}\hat{\zeta_x} + \hat{\xi_z}\hat{\zeta_z}\right) + \frac{\partial \omega}{\partial\zeta}\left(\hat{\zeta_x}\hat{\zeta_x} + \hat{\zeta_z}\hat{\zeta_z}\right)\right] \end{bmatrix} \tag{3.48}$$

The normal and shear stresses are transformed to generalized curvilinear co-ordinates as well. For brevity, the corresponding lengthy equations are included in Appendix A.

The incorporation of a turbulence model results in a modification of both the pressure and total kinetic energy. Furthermore, all eigenvalues and flux Jacobians have to be modified accordingly.

3.3 Approximate Riemann Solvers

Godunov type, upwind, methods have become popular due to their robustness and potential to achieve high resolution at discontinuities. In the pioneering work of Godunov [80], the key ingredient for capturing shocks, without introducing spurious oscillations is the solution of a Riemann problem. The solution of the Riemann problem, otherwise known as the shock-tube problem, represents the physical and mathematical characteristics of the relevant set of conservation laws. However, since there is no closed-form to the exact solution of the Riemann problem, an iterative exact Riemann solver would result in significant computational costs. Research has thus been focused on the construction of approximate solutions with acceptable accuracy.

Although vacuum conditions, resulting for hypersonic speeds are rarely encountered in most aeronautical engineering applications, vacuum or near-vacuum can occur in initial transients. Linearised approximate Riemann solvers are known to fail, due to negative pressures, well before a vacuum state is reached [81]. In linearised Riemann solvers, such as those presented by Eberle [82] and Roe [83] all wave speeds, eigenvalues, are obtained from a single average state, either an arithmetic mean or a square-root average. Wave speeds determined in this manner tend to underestimate the expansion wave velocity, leading to negative energies and expansion shocks [84].

These difficulties have motivated the investigation of a class of upwind fluxes, based on the construction of integral average-state approximations to the Riemann problem, first introduced by Harten, Lax and van Leer [85] in their HLL solver. The HLL flux can resolve accurately isolated shocks but its inability to preserve an isolated contact or shear wave, can be significant for Navier-Stokes computations, resulting in excessive dissipation of boundary layers. Toro et al. [86] restored the contact wave in the HLL solver by following a procedure similar to that of Harten, Lax and van Leer. The resulting HLLC solver, where C stands for contact wave, contains the most detailed physics of any of the average-state Riemann solvers, known to the author.

3.3.1 The HLLC Riemann Solver

The HLLC solver is an approximate Riemann solver that is essential an extension of the HLL solver. Due to its ability to resolve accurately and effectively isolated shocks and contact waves, the HLLC Riemann solver is incorporated in the present work. In this section the HLLC solver is presented in detail. Although, the turbulence scales k and ω are treated as passive scalars, the definition of turbulent pressure, Eq. (2.38), and the consideration of the turbulent kinetic energy as part of the total energy, Eq.(2.39), necessitate the re-derivation of the HLLC solver.

For a structured curvilinear mesh coordinate system after denoting the contravariant velocity components in the two coordinate directions as:

$$u\hat{\xi_x} + w\hat{\xi_z} = q_\xi \tag{3.49}$$

$$u\hat{\zeta_x} + w\hat{\zeta_z} = q_\zeta \tag{3.50}$$

the split one dimensional, say in ξ- direction, convective part of Eq. (3.44) assumes the form:

$$J\begin{bmatrix}\rho\\ \rho u\\ \rho w\\ e\\ \rho k\\ \rho\omega\end{bmatrix}_t + \begin{bmatrix}\rho\hat{q}_\xi\\ \rho u\hat{q}_\xi + p_t\hat{\xi_x}\\ \rho w\hat{q}_\xi + p_t\hat{\xi_z}\\ (e+p_t)\,\hat{q}_\xi\\ \rho k\hat{q}_\xi\\ \rho\omega\hat{q}_\xi\end{bmatrix}_\xi = 0 \tag{3.51}$$

Introducing, H, the total enthalpy $H = \frac{(e+p_t)}{\rho} = \frac{\gamma}{\gamma-1}\frac{p_t}{\rho} + \frac{q^2}{2} + \mathbf{C}k$, where $q = [u\ w]^T$ is the velocity vector, then Eq. (3.51) reads:

$$J\begin{bmatrix}\rho\\ \rho u\\ \rho w\\ e\\ \rho k\\ \rho\omega\end{bmatrix}_t + \begin{bmatrix}\rho\hat{q}_\xi\\ \rho u\hat{q}_\xi + p_t\hat{\xi_x}\\ \rho w\hat{q}_\xi + p_t\hat{\xi_z}\\ H\rho\hat{q}_\xi\\ \rho k\hat{q}_\xi\\ \rho\omega\hat{q}_\xi\end{bmatrix}_\xi = 0 \tag{3.52}$$

or written symbolically as:

$$\mathbf{U}_t + \mathbf{F}_\xi = 0 \tag{3.53}$$

Applying Rankine-Hugoniot conditions $\delta\mathbf{F} = S\delta\mathbf{U}$ across each of the wave of speeds $S_L,\ S_M\ S_R$ one can obtain:

$$\mathbf{F}_L^* = \mathbf{F}_L + S_L\left(\mathbf{U}_L^* - \mathbf{U}_L\right) \tag{3.54}$$

and

$$\mathbf{F}_R^* = \mathbf{F}_R + S_R\left(\mathbf{U}_R^* - \mathbf{U}_R\right) \tag{3.55}$$

or more conveniently:

$$S_O\mathbf{U}_O^* - \mathbf{F}_O^* = S_O\mathbf{U}_O - \mathbf{F}_O \tag{3.56}$$

where the subscript $O = L,\ R$ denotes either left (L) or right (R) states.

Then, the one-dimensional split governing equations, Eq. (3.52), with states $\mathbf{U}_L,\ \mathbf{U}_R$ separated by an interface become:

$$\hat{S}_O\begin{bmatrix}\rho_O^*\\ \rho_O^*u_O^*\\ \rho_O^*w_O^*\\ e_O^*\\ \rho_{*O}k_{*O}\\ \rho_{*O}\omega_{*O}\end{bmatrix} - \begin{bmatrix}\rho_O^*\hat{q}_{\xi,O}^*\\ \rho_O^*u_O^*\hat{q}_{\xi O}^* + p_{t,O}^*\hat{\xi}_x\\ \rho_O^*w_O^*\hat{q}_{\xi O}^* + p_{t,O}^*\hat{\xi}_z\\ \rho_O^*H_O^*\hat{q}_{\xi,O}^*\\ \rho_O^*k_O^*\hat{q}_{\xi,O}^*\\ \rho_O^*\omega_O^*\hat{q}_{\xi,O}^*\end{bmatrix} = \hat{S}_O\begin{bmatrix}\rho_O\\ \rho_Ou_O\\ \rho_Ow_O\\ e_O\\ \rho_Ok_O\\ \rho_O\omega_O\end{bmatrix} - \begin{bmatrix}\rho_O\hat{q}_{\xi,O}\\ \rho_Ou_O\hat{q}_{\xi,O} + p_{t,O}\hat{\xi}_x\\ \rho_Ow_O\hat{q}_{\xi,O} + p_{t,O}\hat{\xi}_z\\ \rho_OH_O\hat{q}_{\xi,O}\\ \rho_Ok_O\hat{q}_{\xi,O}\\ \rho_O\omega_O\hat{q}_{\xi,O}\end{bmatrix} \tag{3.57}$$

where $\hat{S}_O = JS_O$.

In order to find the state vectors $\mathbf{U}_O^*$ and hence determine the intercell fluxes $\mathbf{F}_O^*$, an assumption is being made that the particle velocity is constant across the Riemann fan and that is:

$$\hat{q}_{\xi,L}^* = \hat{q}_{\xi,R}^* = \hat{q}_\xi^* = \hat{S}_M \tag{3.58}$$

Inserting Eq. (3.58), to continuity equation and rearranging gives:

$$\rho_O^* = \rho_O \frac{\left(\hat{S}_O - \hat{q}_{\xi\,O}\right)}{\left(\hat{S}_O - \hat{S}_M\right)} \tag{3.59}$$

Furthermore, by multiplying the x and z components of the continuity equation by $\hat{\xi_x}$, $\hat{\xi_z}$ respectively, summing and inserting Eq. (3.59) yields:

$$p_{t,O}^* = \rho_O \left[\left(\hat{q}_{\xi\,O} - \hat{S}_O\right)\left(\hat{q}_{\xi\,O} - \hat{S}_M\right)\right]/A^2 + p_{t\,O} \tag{3.60}$$

where $A^2 = \hat{\xi_x}\hat{\xi_x} + \hat{\xi_z}\hat{\xi_z}$ is the squared unit length.

For the definition of the, all important, contact wave speed S_M, the latter equation is expanded for the left and right states and since pressure is not discontinuous across a contact wave, that is:

$$p_{t,R}^* = p_{t,L}^* \tag{3.61}$$

then Eq. (3.60) reads:

$$\rho_R \left[\left(\hat{q}_{\xi,R} - \hat{S}_R\right)\left(\hat{q}_{\xi,R} - \hat{S}_M\right)\right]/A^2 + p_{t,R} = \rho_L \left[\left(\hat{q}_{\xi,L} - \hat{S}_L\right)\left(\hat{q}_{\xi,L} - \hat{S}_M\right)\right]/A^2 + p_{t,L}$$

Expanding the terms in the brackets, rearranging and solving for S_M gives:

$$\hat{S}_M = \frac{\rho_R \hat{q}_{\xi,R}\left(\hat{S}_R - \hat{q}_{\xi,R}\right) - \rho_L \hat{q}_{\xi,L}\left(\hat{S}_L - \hat{q}_{\xi,L}\right) + \left(p_{t,L} - p_{t\,R}\right)A^2}{\rho_R\left(\hat{S}_R - \hat{q}_{\xi,R}\right) - \rho_L\left(\hat{S}_L - \hat{q}_{\xi,L}\right)} \tag{3.62}$$

Having specified ρ_O^*, $p_{t\,O}^*$ and $\hat{S}_M$then $(\rho u)_O^*$, $(\rho w)_O^*$, e_O^*, $(\rho k)_O^*$ and $(\rho\omega)_O^*$ can be directly obtained from Eq. (3.57):

$$(\rho u)_O^* = \frac{\rho_O u_O\left(\hat{S}_O - \hat{q}_{\xi\,O}\right) + \left(p_{t\,O}^* - p_{t\,O}\right)\hat{\xi_x}}{\left(\hat{S}_O - \hat{S}_M\right)} \tag{3.63}$$

$$(\rho w)_O^* = \frac{\rho_O w_O \left(\hat{S}_O - \hat{q}_{\xi\,O}\right) + \left(p_{t\,O}^* - p_{t\,O}\right)\hat{\xi}_z}{\left(\hat{S}_O - \hat{S}_M\right)} \tag{3.64}$$

$$e_O^* = \frac{e_O \left(\hat{S}_O - \hat{q}_{\xi\,O}\right) - p_{t\,O}\left(\hat{q}_{\xi\,O} - \hat{\xi}_t\right) + p_{t,O}^* \left(\hat{S}_M - \hat{\xi}_t\right)}{\left(\hat{S}_O - \hat{S}_M\right)} \tag{3.65}$$

$$(\rho k)_O^* = (\rho k)_O \frac{\left(\hat{S}_O - \hat{q}_{\xi\,O}\right)}{\left(\hat{S}_O - \hat{S}_M\right)} \tag{3.66}$$

$$(\rho \omega)_O^* = (\rho \omega)_O \frac{\left(\hat{S}_O - \hat{q}_{\xi\,O}\right)}{\left(\hat{S}_O - \hat{S}_M\right)} \tag{3.67}$$

Rewriting the components of the HLLC flux in vector form:

$$U_L^* = \begin{bmatrix} \rho_L^* \\ (\rho u)_L^* \\ (\rho w)_L^* \\ e_L^* \\ (\rho k)_L^* \\ (\rho \omega)_L^* \end{bmatrix} = \frac{1}{\left(\hat{S}_L - \hat{S}_M\right)} \begin{bmatrix} \rho_L \left(\hat{S}_L - \hat{q}_{\xi,L}\right) \\ (\rho u)_L \left(\hat{S}_L - \hat{q}_{\xi,L}\right) + \left(p_{t\,L}^* - p_{t\,L}\right)\hat{\xi}_x \\ (\rho w)_L \left(\hat{S}_L - \hat{q}_{\xi,L}\right) + \left(p_{t\,L}^* - p_{t\,L}\right)\hat{\xi}_x \\ e_L \left(\hat{S}_L - \hat{q}_{\xi,L}\right) - p_{t\,L}\left(\hat{q}_{\xi,L} - \hat{\xi}_t\right) + p_{t,L}^* \left(\hat{S}_M - \hat{\xi}_t\right) \\ (\rho k)_L \left(\hat{S}_L - \hat{q}_{\xi,L}\right) \\ (\rho \omega)_L \left(\hat{S}_L - \hat{q}_{\xi,L}\right) \end{bmatrix} \tag{3.68}$$

while the intercell convective flux is:

$$F_L^* = \begin{bmatrix} \rho_L^* \hat{S}_M \\ (\rho u)_L^* \hat{S}_M + p_t^* \hat{\xi}_x \\ (\rho w)_L^* \hat{S}_M + p_t^* \hat{\xi}_z \\ \left(e_L^* + p_t^*\right)\hat{S}_M - p_t^* \hat{\xi}_t \\ (\rho k)_L^* \hat{S}_M \\ (\rho \omega)_L^* \hat{S}_M \end{bmatrix} \tag{3.69}$$

The derivation of the star values is different from the one presented in Batten et al. [84], in that the actual metrics instead of the unit normals are being used.

This does not affect the solution itself, but effectively reduces the floating point arithmetics performed per iteration.

3.3.2 Wave Speed Estimates

According to Batten et al. [87], the following wave speed estimates yield the exact particle velocity at isolated shocks and are proven to be very robust:

$$\hat{S}_L = min\left[\hat{q}_{\xi\,L} - c_L\sqrt{\hat{\xi}_x^2 + \hat{\xi}_z^2},\ \tilde{\hat{q}}_\xi - \tilde{c}\sqrt{\hat{\xi}_x^2 + \hat{\xi}_z^2}\right] \tag{3.70}$$

$$\hat{S}_R = max\left[\hat{q}_{\xi\,R} + c_R\sqrt{\hat{\xi}_x^2 + \hat{\xi}_z^2},\ \tilde{\hat{q}}_\xi + \tilde{c}\sqrt{\hat{\xi}_x^2 + \hat{\xi}_z^2}\right] \tag{3.71}$$

where the superscript $\tilde{}$ denotes the Roe averaged values:

$$\tilde{\hat{q}}_\xi = \tilde{u}\hat{\xi}_x + \tilde{w}\hat{\xi}_z \tag{3.72}$$

$$\tilde{u} = \frac{u_L + u_R R_\rho}{1 + R_\rho} \tag{3.73}$$

$$\tilde{w} = \frac{w_L + w_R R_\rho}{1 + R_\rho} \tag{3.74}$$

$$\tilde{c}^2 = (\gamma - 1)\left(\tilde{H} - \frac{\tilde{q}^2}{2} - \mathbf{C}\tilde{k}\right) \tag{3.75}$$

$$\tilde{q}^2 = \tilde{u}^2 + \tilde{w}^2 \tag{3.76}$$

$$\tilde{k} = \frac{k_L + k_R R_\rho}{1 + R_\rho} \tag{3.77}$$

$$\tilde{H} = \frac{H_L + H_R R_\rho}{1 + R_\rho} \tag{3.78}$$

and

$$R_\rho = \sqrt{\frac{\rho_L}{\rho_R}} \tag{3.79}$$

3.4 High Order Upwind Scheme

The divergence of the inviscid fluxes is approximated by the implementation of different reconstruction methods. High order reconstruction of the conservative variables at the cell faces is realized by employing 2^{nd} order MUSCL type limiters, van Albada [36] and van Leer [32, 33], while higher order resolution is accomplished via the implementation of 3^{rd} and 5^{th} order WENO reconstructions, according to Shu [37]. The interpolation stencils, used for the flux reconstruction at the cell interface, of the different discretisation schemes are shown in Figure 3.1.

- MUSCL scheme

According to the upwind MUSCL scheme, the left and right states are defined as:

$$\left.\begin{array}{c} \mathbf{U}_{L\,i+1/2} = \mathbf{U}_i + 0.5\phi\left(r_i\right) \bigtriangledown \mathbf{U}_i \\ \mathbf{U}_{R\,i+1/2} = \mathbf{U}_{i+1} - 0.5\phi\left(r_{i+1}\right) \bigtriangleup \mathbf{U}_{i+1} \end{array}\right\}, \tag{3.80}$$

where $\phi\left(r_i\right)$ is either the van Albada:

$$\phi\left(r_i\right) = \frac{r + r^2}{1 + r^2 + \epsilon} \tag{3.81}$$

or the van Leer limiter:

$$\phi\left(r_i\right) = \frac{r + |r|}{1 + r + \epsilon} \tag{3.82}$$

where $r = \bigtriangledown \mathbf{U}_i / \bigtriangleup \mathbf{U}_i$, $\bigtriangledown \mathbf{U}_i = \mathbf{U}_i - \mathbf{U}_{i-1}$, $\bigtriangleup \mathbf{U}_i = \mathbf{U}_{i+1} - \mathbf{U}_i$, and ϵ is a small positive number preventing division by zero.

- WENO scheme

The 3^{rd} order WENO reconstruction for the left state can be written as:

$$\mathbf{U}_{L\,i+1/2} = \tilde{\omega}_0 \mathbf{q}_0 + \tilde{\omega}_1 \mathbf{q}_1 \tag{3.83}$$

where

$$\left.\begin{array}{c} \mathbf{q}_0 = \frac{1}{2}\mathbf{U}_i + \frac{1}{2}\mathbf{U}_{i+1} \\ \mathbf{q}_1 = -\frac{1}{2}\mathbf{U}_{i-1} + \frac{3}{2}\mathbf{U}_i \end{array}\right\} \tag{3.84}$$

and

$$\tilde{\omega}_r = \frac{\tilde{\alpha}_r}{\tilde{\alpha}_0 + \tilde{\alpha}_1 + \tilde{\alpha}_2}, \quad \tilde{\alpha}_r = \frac{\tilde{d}_r}{(\epsilon + \beta_r)^2}, \quad with \quad r = 0,\ 1 \tag{3.85}$$

$$\tilde{d}_0 = \frac{2}{3},\ \tilde{d}_1 = \frac{1}{3} \tag{3.86}$$

and

$$\left.\begin{array}{c} \beta_0 = (\mathbf{U}_{i+1} - \mathbf{U}_i)^2 \\ \beta_1 = (\mathbf{U}_i - \mathbf{U}_{i-1})^2 \end{array}\right\} \tag{3.87}$$

The more elaborate 5^{th} order WENO reconstruction for the left state can be written as:

$$\mathbf{U}_{L\,i+1/2} = \tilde{\omega}_0 \mathbf{q}_0 + \tilde{\omega}_1 \mathbf{q}_1 + \tilde{\omega}_2 \mathbf{q}_2 \tag{3.88}$$

where

$$\left.\begin{array}{l} \mathbf{q}_0 = \frac{1}{3}\mathbf{U}_i + \frac{5}{6}\mathbf{U}_{i+1} - \frac{1}{6}\mathbf{U}_{i+2} \\ \mathbf{q}_1 = -\frac{1}{6}\mathbf{U}_{i-1} + \frac{5}{6}\mathbf{U}_i + \frac{1}{3}\mathbf{U}_{i+1} \\ \mathbf{q}_2 = \frac{1}{3}\mathbf{U}_{i-2} - \frac{7}{6}\mathbf{U}_{i-1} + \frac{11}{6}\mathbf{U}_i \end{array}\right\} \tag{3.89}$$

and

$$\tilde{\omega}_r = \frac{\tilde{\alpha}_r}{\tilde{\alpha}_0 + \tilde{\alpha}_1 + \tilde{\alpha}_2}, \quad \tilde{\alpha}_r = \frac{\tilde{d}_r}{(\epsilon + \beta_r)^2}, \quad with \quad r = 0,\ 1,\ 2 \tag{3.90}$$

$$\tilde{d}_0 = 0.3,\ \tilde{d}_1 = 0.6,\ \ \tilde{d}_2 = 0.1 \tag{3.91}$$

and

$$\left.\begin{array}{c} \beta_0 = \frac{13}{12}\left(\mathbf{U}_i - 2\mathbf{U}_{i+1} + \mathbf{U}_{i+2}\right)^2 + \frac{1}{4}\left(3\mathbf{U}_i - 4\mathbf{U}_{i+1} + \mathbf{U}_{i+2}\right)^2 \\ \beta_1 = \frac{13}{12}\left(\mathbf{U}_{i-1} - 2\mathbf{U}_i + \mathbf{U}_{i+1}\right)^2 + \frac{1}{4}\left(\mathbf{U}_{i-1} + \mathbf{U}_{i+1}\right)^2 \\ \beta_2 = \frac{13}{12}\left(\mathbf{U}_{i-2} - 2\mathbf{U}_{i-1} + \mathbf{U}_i\right)^2 + \frac{1}{4}\left(\mathbf{U}_{i-2} - 4\mathbf{U}_{i-1} + 3\mathbf{U}_i\right)^2 \end{array}\right\} \tag{3.92}$$

where, similarly to the MUSCL scheme, ϵ is introduced to avoid the denominator becoming zero. Numerical tests in [37] indicate that the results are not sensitive to the value of ϵ when it is in the range $10^{-7} < \epsilon < 10^{-5}$.

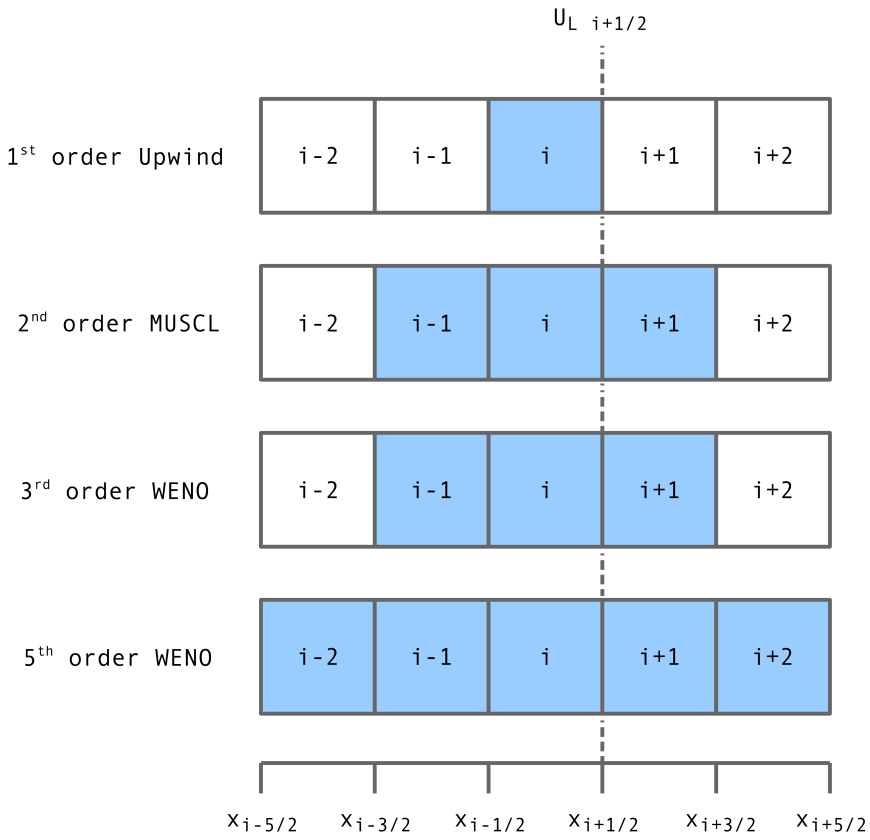

Figure 3.1: Interpolation stencils according to the Upwind, MUSCL and WENO schemes. Blue areas indicate the cells used for the interpolation.

3.5 Implicit Unfactored Method

The time integration of the Navier-Stokes and turbulence model equations is obtained by an implicit unfactored method [88] which allows high CFL numbers to be used. The implicit unfactored discretisation of the governing equations is combined with Newton sub-iterations and point-successive Gauss-Seidel relaxation. This algorithm was found to provide high efficiency in both vector and parallel computations [89, 90]. According to this method Eq. (3.44) is written after a first-order implicit discretisation in time as:

$$\frac{\mathbf{U}^{n+1}-\mathbf{U}^{n}}{\Delta t}+\mathbf{F}_{\xi}^{n+1}+\mathbf{G}_{\zeta}^{n+1}=\mathbf{R}_{\xi}^{n+1}+\mathbf{S}_{\zeta}^{n+1}+\mathbf{H}^{n+1}. \tag{3.93}$$

Since Eq. (3.93) is not directly solvable for the dependent variable U^{n+1}, due to its nonlinearity, a sequence of approximations denoted by U^{ν} is constructed such that $lim_{v\to\infty}\mathbf{U}^{\nu}\to\mathbf{U}^{n+1}$:

$$\frac{\mathbf{U}^{\nu+1}-\mathbf{U}^{n}}{\Delta t}+\mathbf{F}_{\xi}^{\nu+1}+\mathbf{G}_{\zeta}^{\nu+1}=\mathbf{R}_{\xi}^{\nu+1}+\mathbf{S}_{\zeta}^{\nu+1}+\mathbf{H}^{\nu+1}. \tag{3.94}$$

Linearising the inviscid fluxes and the source terms:

$$\begin{aligned}\mathbf{F}^{\nu+1} &= \mathbf{F}^{\nu}+\mathbf{A}_{inv}^{\nu}\Delta\mathbf{U},\\ \mathbf{G}^{\nu+1} &= \mathbf{G}^{\nu}+\mathbf{C}_{inv}^{\nu}\Delta\mathbf{U},\\ \mathbf{H}^{\nu+1} &= \mathbf{H}^{\nu}+\mathbf{D}_{inv}^{\nu}\Delta\mathbf{U}\end{aligned} \tag{3.95}$$

where $\Delta\mathbf{U}=\mathbf{U}^{\nu+1}-\mathbf{U}^{\nu}$ is the variation of the solution vector in time, and

$$\mathbf{A}_{inv}=\frac{\partial\mathbf{F}}{\partial\mathbf{U}},\quad \mathbf{C}_{inv}=\frac{\partial\mathbf{G}}{\partial\mathbf{U}},\quad \mathbf{D}=\frac{\partial\mathbf{H}}{\partial\mathbf{U}} \tag{3.96}$$

The linearisation of the viscous fluxes must be handled with special care, owning to the fact that the components of the viscous flux vector are composed of gradients of the dependent variables. Therefore,

$$\begin{aligned}\mathbf{R}^{\nu+1} &= \mathbf{R}^{\nu}+\mathbf{A}_{vis,\xi}^{\nu}\Delta\mathbf{U}_{\xi}+\mathbf{A}_{vis,\zeta}^{\nu}\Delta\mathbf{U}_{\zeta},\\ \mathbf{G}^{\nu+1} &= \mathbf{G}^{\nu}+\mathbf{C}_{vis,\xi}^{\nu}\Delta\mathbf{U}_{\xi}+\mathbf{C}^{\nu}{}_{vis,\zeta}\Delta\mathbf{U}_{\zeta}\end{aligned} \tag{3.97}$$

where:

$$\mathbf{A}_{vis,\xi}=\frac{\partial\mathbf{R}}{\partial\mathbf{U}_{\xi}},\quad \mathbf{A}_{vis,\zeta}=\frac{\partial\mathbf{R}}{\partial\mathbf{U}_{\zeta}},\quad \mathbf{C}_{vis,\xi}=\frac{\partial\mathbf{G}}{\partial\mathbf{U}_{\xi}},\quad \mathbf{C}_{vis,\zeta}=\frac{\partial\mathbf{G}}{\partial\mathbf{U}_{\zeta}} \tag{3.98}$$

However, for the construction of the implicit scheme it is not necessary to balance the resulting equation perfectly since the left-hand-side is required only to guarantee stability [91, 92]. Thus the viscous Jacobians can be reduced by assuming thin-layer approximations, but for both directions at the same time, leading to:

$$\begin{aligned} \mathbf{R}^{\nu+1} = &\quad \mathbf{R}^{\nu} + \mathbf{A}^{\nu}_{vis,\xi}\Delta\mathbf{U}_{\xi}, \\ \mathbf{G}^{\nu+1} = &\quad \mathbf{G}^{\nu} + \mathbf{C}^{\nu}_{vis,\zeta}\Delta\mathbf{U}_{\zeta} \end{aligned} \tag{3.99}$$

A non-linear Newton method for $U^{\nu+1}$ can be developed around the subiteration state ν, such that:

$$\begin{gathered} \tfrac{\Delta\mathbf{U}}{\Delta t} + (\mathbf{A}^{\nu}_{inv}\Delta\mathbf{U})_{\xi} + (\mathbf{C}^{\nu}_{inv}\Delta\mathbf{U})_{\zeta} - (\mathbf{A}^{\nu}_{vis,\xi}\Delta\mathbf{U}_{\xi})_{\xi} - (\mathbf{C}^{\nu}_{vis,\zeta}\Delta\mathbf{U}_{\zeta})_{\zeta} - \mathbf{D}^{\nu}\Delta\mathbf{U} \quad = \\ -\left(\tfrac{\mathbf{U}^{\nu}-\mathbf{U}^{n}}{\Delta t} + \mathbf{F}^{\nu}{}_{\xi} + \mathbf{G}^{\nu}{}_{\zeta} - \mathbf{R}^{\nu}_{\xi} - \mathbf{S}^{\nu}_{\zeta} - \mathbf{H}^{\nu}\right) \equiv RHS \end{gathered} \tag{3.100}$$

The inviscid Jacobians are written in terms of their eigenvector and eigenvalue matrices as:

$$\mathbf{A}_{inv} = \mathbf{T}\mathbf{\Lambda}\mathbf{T}^{-1} \tag{3.101}$$

where $\mathbf{\Lambda}$ is the eigenvalue matrix and $\mathbf{T}$, $\mathbf{T}^{-1}$ are the left and right eigenvector matrices, respectively.

The inviscid terms $(\mathbf{A}^{\nu}_{inv}\Delta\mathbf{U})_{\xi}$ and $(\mathbf{C}^{\nu}_{inv}\Delta\mathbf{U})_{\zeta}$ are discretised up to second-order of accuracy, i.e., the left-hand-side term in ξ-direction is discretised as:

$$(\mathbf{A}^{\nu}_{inv}\Delta\mathbf{U})_{\xi} = \quad (\mathbf{A}^{\nu}_{inv}\Delta\mathbf{U})_{i+1/2,k} - (\mathbf{A}^{\nu}_{inv}\Delta\mathbf{U})_{i-1/2,k} \tag{3.102}$$

At this stage the flux vector splitting method of Steger-Warming [93] is employed whereby, the homogeneous property of the Euler equations is exploited and, the fluxes are decomposed to positive and negative parts with respect to the sign of the eigenvalues:

$$(\mathbf{A}^{\nu}_{inv}\Delta\mathbf{U})_{i+1/2,k} = \left(\mathbf{T}\mathbf{\Lambda}^{+}\mathbf{T}^{-1}\right)^{\nu}_{i+1/2,k}\Delta\mathbf{U}^{+}_{i+1/2,k} + \left(\mathbf{T}\mathbf{\Lambda}^{-}\mathbf{T}^{-1}\right)^{\nu}_{i+1/2,k}\Delta\mathbf{U}^{-}_{i+1/2,k}, \tag{3.103}$$

$$(\mathbf{A}^{\nu}_{inv}\Delta\mathbf{U})_{i-1/2,k} = \left(\mathbf{T}\mathbf{\Lambda}^{+}\mathbf{T}^{-1}\right)^{\nu}_{i-1/2,k}\Delta\mathbf{U}^{+}_{i-1/2,k} + \left(\mathbf{T}\mathbf{\Lambda}^{-}\mathbf{T}^{-1}\right)^{\nu}_{i-1/2,k}\Delta\mathbf{U}^{-}_{i-1/2,k} \tag{3.104}$$

and similarly for the ζ- direction;

$$(C^{\nu}_{inv}\Delta\mathbf{U})_{\zeta} = \quad (\mathbf{C}^{\nu}_{inv}\Delta\mathbf{U})_{i,k+1/2} - (\mathbf{C}^{\nu}_{inv}\Delta\mathbf{U})_{i,k-1/2} \tag{3.105}$$

with

$$(\mathbf{C}^{\nu}_{inv}\Delta\mathbf{U})_{i+1/2,k} = \left(\mathbf{T}\mathbf{\Lambda}^{+}\mathbf{T}^{-1}\right)^{\nu}_{i,k+1/2}\Delta\mathbf{U}^{+}_{i,k+1/2} + \left(\mathbf{T}\mathbf{\Lambda}^{-}\mathbf{T}^{-1}\right)^{\nu}_{i,k+1/2}\Delta\mathbf{U}^{-}_{i,k+1/2}, \tag{3.106}$$

$$(\mathbf{C}^{\nu}_{inv}\Delta\mathbf{U})_{i-1/2,k} = \left(\mathbf{T}\mathbf{\Lambda}^{+}\mathbf{T}^{-1}\right)^{\nu}_{i,k-1/2}\Delta\mathbf{U}^{+}_{i,k-1/2} + \left(\mathbf{T}\mathbf{\Lambda}^{-}\mathbf{T}^{-1}\right)^{\nu}_{i,k-1/2}\Delta\mathbf{U}^{-}_{i,k-1/2} \tag{3.107}$$

where, $\Lambda^{+} = max(0,\Lambda)$ and $\Lambda^{-} = min(0,\Lambda)$ are the diagonal matrices of the positive and negative eigenvalues of the inviscid Jacobians. The differences $\Delta\mathbf{U}^{+}$ and $\Delta\mathbf{U}^{-}$ are defined at the cell faces up to first order as:

$$\Delta\mathbf{U}^{+}_{i+1/2,k} = \Delta\mathbf{U}^{-}_{i-1/2,k} = \Delta\mathbf{U}^{+}_{i,k+1/2} = \Delta\mathbf{U}^{-}_{i,k-1/2} = \Delta\mathbf{U}_{i,k} \tag{3.108}$$

$$\Delta\mathbf{U}^{-}_{i+1/2,k} = \Delta\mathbf{U}_{i+1,k}, \quad \Delta\mathbf{U}^{+}_{i-1/2,k} = \Delta\mathbf{U}_{i-1,k} \tag{3.109}$$

$$\Delta\mathbf{U}^{-}_{i,k+1/2} = \Delta\mathbf{U}_{i,k+1}, \quad \Delta\mathbf{U}^{+}_{i,k-1/2} = \Delta\mathbf{U}_{i,k-1} \tag{3.110}$$

The viscous terms are similarly discretised as,

$$\left(\mathbf{A}^{\nu}_{vis,\xi}\Delta\mathbf{U}_{\xi}\right)_{\xi} = \left(\mathbf{A}^{\nu}_{vis,\xi}\Delta\mathbf{U}_{\xi}\right)_{i+1/2,k} - \left(\mathbf{A}^{\nu}_{vis,\xi}\Delta\mathbf{U}_{\xi}\right)_{i-1/2,k} \tag{3.111}$$

where the term $\mathbf{A}_{vis,\xi}$ is calculated by simple averaging, while the gradient $\Delta\mathbf{U}_{\xi}$ is evaluated by central differencing. Hence,

$$\begin{aligned}\left(\mathbf{A}^{\nu}_{vis,\xi}\Delta\mathbf{U}_{\xi}\right)_{\xi} = \; & \tfrac{1}{2}\left(\mathbf{A}^{\nu}_{vis,\xi}\big|_{i,k} + \mathbf{A}^{\nu}_{vis,\xi}\big|_{i+1,k}\right)(\Delta\mathbf{U}_{i+1,k} - \Delta\mathbf{U}_{i,k}) \\ & -\tfrac{1}{2}\left(\mathbf{A}^{\nu}_{vis,\xi}\big|_{i,k} + \mathbf{A}^{\nu}_{vis,\xi}\big|_{i-1,k}\right)(\Delta\mathbf{U}_{i,k} - \Delta\mathbf{U}_{i-1,k})\end{aligned} \tag{3.112}$$

Performing inner operations, collecting common terms and denoting:

$$\begin{aligned}
\mathbf{L}_{i+1/2,k} &= \frac{1}{2}\left(\mathbf{A}_{vis,\xi}|_{i,k} + \mathbf{A}_{vis,\xi}|_{i+1,k}\right) \\
\mathbf{L}_{i-1/2,k} &= \frac{1}{2}\left(\mathbf{A}_{vis,\xi}|_{i,k} + \mathbf{A}_{vis,\xi}|_{i-1,k}\right) \\
\mathbf{L}_{i,k} &= \frac{1}{2}\left(\mathbf{A}_{vis,\xi}|_{i-1,k} + 2\,\mathbf{A}_{vis,\xi}|_{i,k} + \mathbf{A}_{vis,\xi}|_{i+1,k}\right) = \mathbf{L}_{i+1/2,k} + \mathbf{L}_{i-1/2,k}
\end{aligned} \tag{3.113}$$

result in:

$$\left(\mathbf{A}^{\nu}_{vis,\xi}\Delta\mathbf{U}_{\xi}\right)_{\xi} = \mathbf{L}^{\nu}_{i+1/2,k}\Delta\mathbf{U}_{i+1,k} - \mathbf{L}^{\nu}_{i,k}\Delta\mathbf{U}_{i,k} + \mathbf{L}^{\nu}_{i-1/2,k}\Delta\mathbf{U}_{i-1,k} \tag{3.114}$$

Similarly for the ζ- direction:

$$\left(\mathbf{C}^{\nu}_{vis,\zeta}\Delta\mathbf{U}_{\zeta}\right)_{\zeta} = \mathbf{N}^{\nu}_{i,k+1/2}\Delta\mathbf{U}_{i,k+1} - \mathbf{N}^{\nu}_{i,k}\Delta\mathbf{U}_{i,k} + \mathbf{N}^{\nu}_{i,k-1/2}\Delta\mathbf{U}_{i,k-1} \tag{3.115}$$

where,

$$\begin{aligned}
\mathbf{N}_{i,k+1/2} &= \frac{1}{2}\left(\mathbf{C}_{vis,\zeta}|_{i,k} + \mathbf{C}_{vis,\zeta}|_{i,k+1}\right) \\
\mathbf{N}_{i,k-1/2} &= \frac{1}{2}\left(\mathbf{C}_{vis,\zeta}|_{i,k} + \mathbf{C}_{vis,\zeta}|_{i,k-1}\right) \\
\mathbf{N}_{i,k} &= \frac{1}{2}\left(\mathbf{C}_{vis,\zeta}|_{i,k-1} + 2\,\mathbf{C}_{vis,\zeta}|_{i,k} + \mathbf{C}_{vis,\zeta}|_{i,k+1}\right) = \mathbf{N}_{i,k+1/2} + \mathbf{N}_{i,k-1/2}
\end{aligned} \tag{3.116}$$

Since the numerical solution of the Newton method is too time-consuming and the application of an approximate-factorization scheme leads to significant time-step restrictions, a Gauss-Seidel (GS) relaxation technique is used to solve the unfactored implicit governing equations. The discretised form of Eq. (3.100) for a point GS iteration reads:

$$\left[\frac{\mathbf{I}}{\Delta t} + (DIAG)^{\nu}_{i,k}\right]\Delta\mathbf{U}^{\mu}_{i,k} = \omega\,(RHS)_{i,k} + (ODIAG)^{\nu}_{ik} \tag{3.117}$$

where,

$$\begin{aligned}(DIAG)^{\nu}_{i,k} &= (\mathbf{T}\mathbf{\Lambda}^{+}\mathbf{T}^{-1})^{\nu}_{i+1/2,k} - (\mathbf{T}\mathbf{\Lambda}^{-}\mathbf{T}^{-1})^{\nu}_{i-1/2,k} \\ &+ (\mathbf{T}\mathbf{\Lambda}^{+}\mathbf{T}^{-1})^{\nu}_{i,k+1/2} - (\mathbf{T}\mathbf{\Lambda}^{-}\mathbf{T}^{-1})^{\nu}_{i,k-1/2} \\ &+ \mathbf{L}^{\nu}_{i,k} + \mathbf{N}^{\nu}_{i,k} - \mathbf{D}^{\nu}_{i,k}\end{aligned} \tag{3.118}$$

$(DIAG)^{\nu}_{i,k}$ is a matrix including the diagonal elements of the eigenvalue-split inviscid and the viscous thin-layer Jacobians together with the source Jacobian $\mathbf{D}^{\nu}_{i,k}$. $(ODIAG)^{\nu}_{i,k}$ includes the complementary off-diagonal elements and is a function of the neighboring points $\Delta\mathbf{U}_{i+1,k}$, $\Delta\mathbf{U}_{i-1,k}$, $\Delta\mathbf{U}_{i,k+1}$, $\Delta\mathbf{U}_{i,k-1}$:

$$\begin{aligned}(ODIAG)^{\nu}_{i,k} &= -(\mathbf{T}\mathbf{\Lambda}^{-}\mathbf{T}^{-1} - \mathbf{L})^{\nu}_{i+1/2,k}\,\Delta\mathbf{U}_{i+1,k} \\ &\quad + (\mathbf{T}\mathbf{\Lambda}^{+}\mathbf{T}^{-1} + \mathbf{L})^{\nu}_{i-1/2,k}\,\Delta\mathbf{U}_{i-1,k} \\ &\quad - (\mathbf{T}\mathbf{\Lambda}^{-}\mathbf{T}^{-1} - \mathbf{N})^{\nu}_{i,k+1/2}\,\Delta\mathbf{U}_{i,k+1} \\ &\quad + (\mathbf{T}\mathbf{\Lambda}^{+}\mathbf{T}^{-1} + \mathbf{N})^{\nu}_{i,k-1/2}\,\Delta\mathbf{U}_{i,k-1}\end{aligned} \tag{3.119}$$

The under-relaxation factor ω compensates for errors of different spatial orders of accuracy on RHS and LHS, and is also used to accelerate convergence to steady state. The RHS term is the divergence of the fluxes at each time step n during the μ Gauss-Seidel iterations. For steady flows, four Gauss-Seidel steps ($\mu = 4$) and two Newton sub-iteration ($\nu = 2$) are usually performed.

The time step Δt is calculated by:

$$\Delta t = \frac{J \quad CFL}{\left[max|\lambda_{i,k}| + 2\frac{\mu c_p}{Pr}\sqrt{(\xi_x^2 + \xi_z^2 + \zeta_x^2 + \zeta_z^2)}\right]}. \tag{3.120}$$

For multi-dimensional problems the matrix $(DIAG)^{\nu}_{i,k}$ has zero or negative diagonal elements and is, therefore, ill-posed for Gauss-elimination. To recover high values of the CFL number, right preconditioning is performed on each Gauss-Seidel sub-iteration [82, 94]. The term $\left[\frac{\mathbf{I}}{\Delta t} + (DIAG)^{\nu}_{i,k}\right]$ of the left-hand-side of Eq. (3.117) is multiplied with the transformation matrix $\mathbf{M} = \dfrac{\partial \mathbf{U}}{\partial \mathbf{u}}$ from the right,

$$\left[\frac{\mathbf{I}}{\Delta t} + (DIAG)^{\nu}_{i,k}\right]\mathbf{M}\Delta\mathbf{u}^{\mu}_{i,k} = \omega\,(RHS)_{i,k} + (ODIAG)^{\nu}_{ik} \tag{3.121}$$

with $\mathbf{\Delta u} = \mathbf{M}^{-1}\mathbf{\Delta U}$ being the vector of the non-conservative variables.

After every Gauss-elimination the conservative solution vector $\Delta\mathbf{U}$ is recovered by:

$$(\Delta\mathbf{U}) = \mathbf{M}\,(\Delta\mathbf{u}) \tag{3.122}$$

Finally, for completeness the inviscid Jacobians, transformation matrix, eigenvectors and the components of the eigenvalue split Jacobians are given in Appendices B, C, D, while the Jacobians of the viscous fluxes are summarized in Appendix E.

3.5.1 Implicit Treatment of the Source Term

The numerical treatment of the source terms of the turbulence equations models are of critical importance for the stability of the scheme. For this reason all destruction terms are treated implicitly, while the production terms are defined explicitly in the right hand side. This procedure leads to an increase in the diagonal dominance of the implicit operator and thereby enhances its stability. The following representation of the approximate Jacobian for the source terms, is indicative of the method employed here.

Considering the equation:

$$\frac{\partial\mathbf{U}}{\partial t} = \mathbf{H} \equiv \mathbf{H}(\mathbf{U}) \tag{3.123}$$

the following first order implicit time discretisation can be obtained :

$$\mathbf{U}^{n+1} = \mathbf{U}^{n} + \Delta t\mathbf{H}^{n+1} \tag{3.124}$$

After linearisation of the source matrix $\mathbf{H}^{n+1}$ (in terms of U):

$$\mathbf{H}^{n+1} = \mathbf{H}^{n} + \frac{\partial\mathbf{H}}{\partial\mathbf{U}}\left(\mathbf{U}^{n+1} - \mathbf{U}^{n}\right) \tag{3.125}$$

Eq. (3.124) is written as:

$$\left(\mathbf{U}^{n+1} - \mathbf{U}^{n}\right)\left(I - \Delta t\frac{\partial\mathbf{H}}{\partial\mathbf{U}}\right) = \Delta t\mathbf{H}^{n}. \tag{3.126}$$

The source terms Jacobian can be calculated as:

$$\frac{\partial \mathbf{H}}{\partial \mathbf{U}} = J \begin{bmatrix} 0 & 0 & 0 & 0 & 0 & 0 \\ 0 & 0 & 0 & 0 & 0 & 0 \\ 0 & 0 & 0 & 0 & 0 & 0 \\ 0 & 0 & 0 & 0 & 0 & 0 \\ \frac{k}{Re\omega}S + Re\beta^*\omega k & 0 & 0 & 0 & \frac{1}{Re\omega}S - \frac{2}{3}D - Re\beta^*\omega & -\frac{k}{Re\omega^2}S - Re\beta^* k \\ a_\omega \frac{1}{Re}S + Re\beta\omega^2 & 0 & 0 & 0 & 0 & -\frac{2}{3}a_\omega D - 2Re\beta\omega \end{bmatrix} \tag{3.127}$$

where S is the strain rate invariant, $S = \left(\frac{\partial u_i}{\partial x_j} + \frac{\partial u_j}{\partial x_i}\right)\frac{\partial u_i}{\partial x_j} - \frac{2}{3}D^2$ and D is the dilatation $D = \frac{\partial u_k}{\partial x_k}$.

However, for stability reasons only destruction terms are treated implicitly [79]. Then the Jacobian matrix for the source terms becomes:

$$\frac{\partial \mathbf{H}}{\partial \mathbf{U}} = J \begin{bmatrix} 0 & 0 & 0 & 0 & 0 & 0 \\ 0 & 0 & 0 & 0 & 0 & 0 \\ 0 & 0 & 0 & 0 & 0 & 0 \\ 0 & 0 & 0 & 0 & 0 & 0 \\ Re\beta^*\omega k & 0 & 0 & 0 & -Re\beta^*\omega & -Re\beta^* k \\ Re\beta\omega^2 & 0 & 0 & 0 & 0 & -2Re\beta\omega \end{bmatrix} \tag{3.128}$$

The elements of the source Jacobian ($\frac{\partial \mathbf{H}}{\partial \mathbf{U}}$) are added to the $(DIAG)^n_{i,k}$ term of Eq. (3.121), thus increasing diagonal dominance.

Chapter 4

Investigation of the Numerical Scheme Effects

In the following chapter, steady state investigations that have been performed on a subsonic flow over the NACA4412 aerofoil and a transonic flow over the Rae2822 aerofoil are presented. The objective of this study is to validate the performance and accuracy of the numerical schemes and turbulence model employed, with varying grid and reconstruction resolution, on two highly diverse flow situations.

The body-fitted, structured, C-type meshes used in the following calculations range from 277×65 (coarse), 397×95 (medium) to 517×125 (fine) in order to evaluate the sensitivity of the simulation to the spatial resolution. Besides the apparent differences in the grid density, all of the generated meshes share similar qualitative charecteristics. In particular: a) the mesh points are exponentially spaced away from the aerofoil surface and the cell spacing adjacent to the wall surface corresponds to a $y^+ < 1$, based on a flat plate assumption, b) the grid lines are clustered near the body surface in the normal direction, such that a minimum of 20 mesh points are contained in the boundary layer in order to resolve it effectively, c) the far field boundary is placed at 20 chord lengths away from the aerofoil and d) in the streamwise direction the clustering at the wall is finer at the leading and trailing edge to capture accurately geometric curvatures and singularities.

The order of reconstruction of the convective fluxes is increased from first up to fifth order, while the viscous fluxes are centrally discretized to second order

accuracy. The resulting non linear system is marched in time with the implicit unfactored method described in Chapter 3. The numerical results obtained are validated against experimental data regarding pressure coefficient distribution and streamwise velocity profiles, where available. It is noteworthy that the velocity profiles are calculated normal to the aerofoil surface, while the velocity is non-dimensionalized with respect to the boundary layer edge velocity, designated in this work by U_e, in agreement with the experiments of Cook et al. [95]. The findings of this investigation are presented in the following sections.

4.1 Transonic flow over the RAE 2822 aerofoil

The RAE 2822 supercritical aerofoil has been used extensively for code validation, of compressible flow solvers, under turbulent transonic flow conditions. A comprehensive experimental database has been established by Cook et al., that covers subcritical as well as supercritical local flow conditions. The present computation corresponds to their Test Case 10, with the adopted corrections of the EUROVAL project [96], that suggest a Mach number of $M_\infty = 0.754$, Reynolds number of $R_\infty = 6.2 \times 10^6$ and angle of incidence of $\alpha = 2.57^o$. In the experiment, the flow was tripped at 3% from the leading edge. However, in the present simulation transition was not modelled or fixed, deliberately, in order to investigate the capabilities and /or limitations of the turbulence model with varying the order of spatial resolution.

In order evaluate the sensitivity of the simulation to the grid resolution, numerical computations were performed on three different meshes, shown in Figure 4.1. The results obtained from the grid convergence study regarding pressure distribution velocity profiles and aerodynamic loads are summarized in Figure 4.2, Figures 4.3 - 4.6 and Table 4.2 respectively. Overall it is observed that by increasing the order of the underlying numerics the grid dependency decreases asymptotically, while no major discrepancies are observed amongst the medium (M2) and fine (M3) meshes. For this reason and due to inevitable time and computational resources constraints, further simulations were carried out on the medium mesh in order to investigate the effect of the numerical spatial accu-

racy on the flow field characteristics. In the subsequent paragraphs a detailed discussion of this investigation is presented.

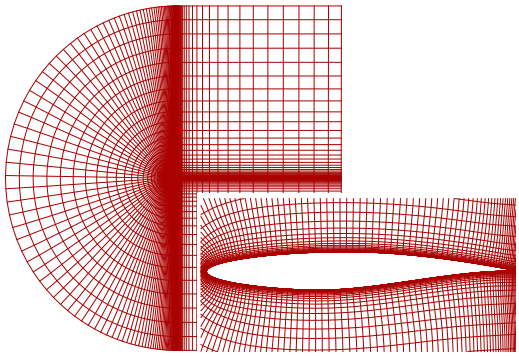

(a) RAE2822 M1 mesh (277x65)

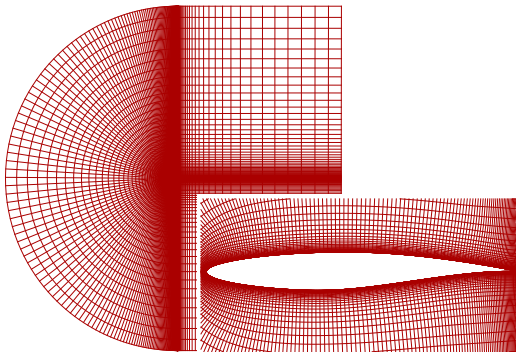

(b) RAE2822 M2 mesh (397x95)

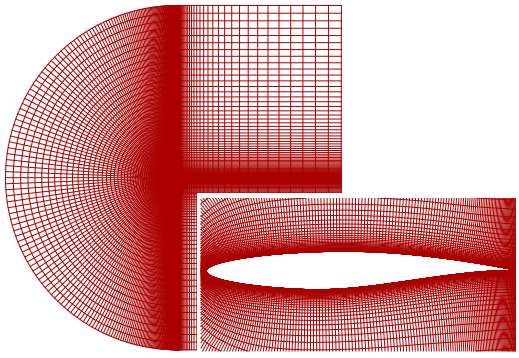

(c) RAE2822 M3 mesh (512x125)

Figure 4.1: Full and close-up views of the RAE2822 meshes

Computed Mach number and eddy viscosity (dimensionless) contours which give a qualitative description of the flow field, and indicate overall computational quality are shown in Figure 4.7. It is evident that different resolution schemes result in discrepancies on the local Mach number, shock location and wake thickness. The flow is accelerated at the suction surface of the aerofoil, where due to local supercritical flow conditions, a strong shock is formed that interacts with the boundary layer. Downstream the shock formation, the induced separation results in a thicker boundary layer that is sharply captured as the order of the method increases. Aft the shock induced separation the flow becomes highly turbulent and the increased levels of turbulence kinetic energy give rise to high values of eddy viscosity.

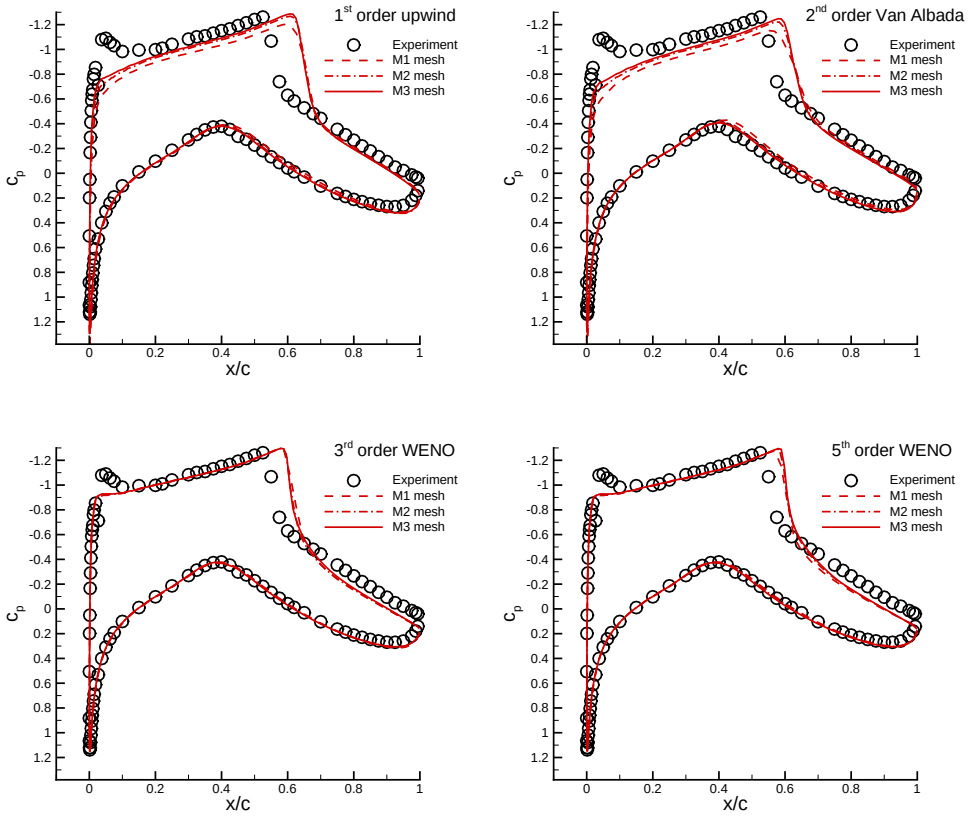

Figure 4.2: Grid convergence of the computed pressure-coefficient distributions along the RAE2822 aerofoil surface.

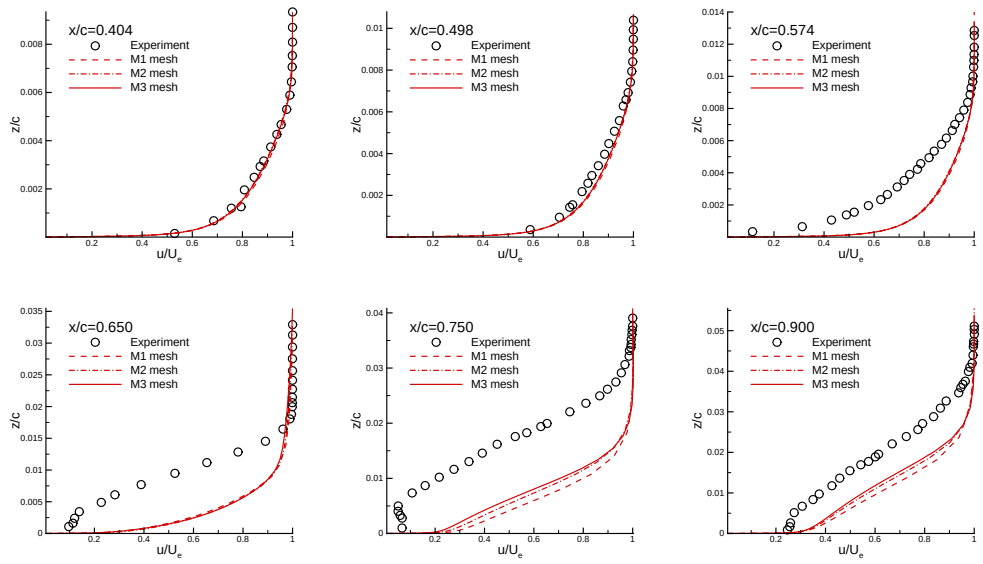

Figure 4.3: Grid convergence of the computed velocity profiles with first order upwind flux reconstruction, along the RAE2822 aerofoil surface.

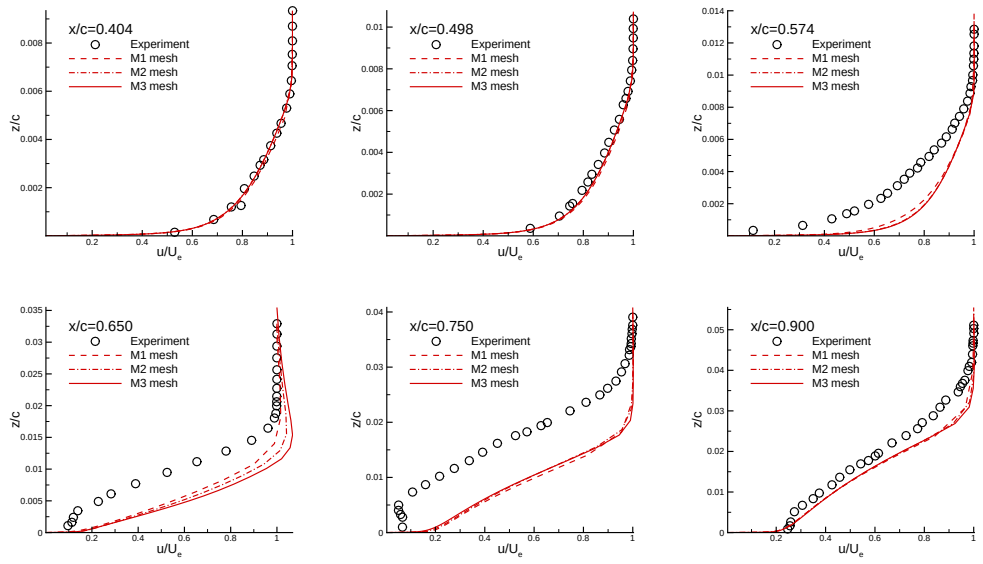

Figure 4.4: Grid convergence of the computed velocity profiles with second order Van Albada MUSCL flux reconstructions, along the RAE2822 aerofoil surface.

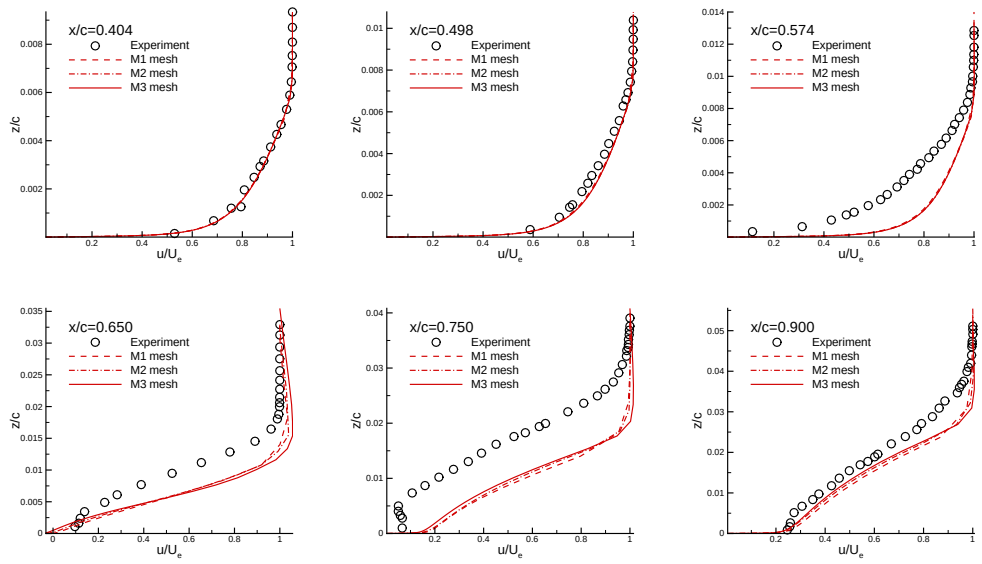

Figure 4.5: Grid convergence of the computed velocity profiles with third order WENO flux reconstructions, along the RAE2822 aerofoil surface.

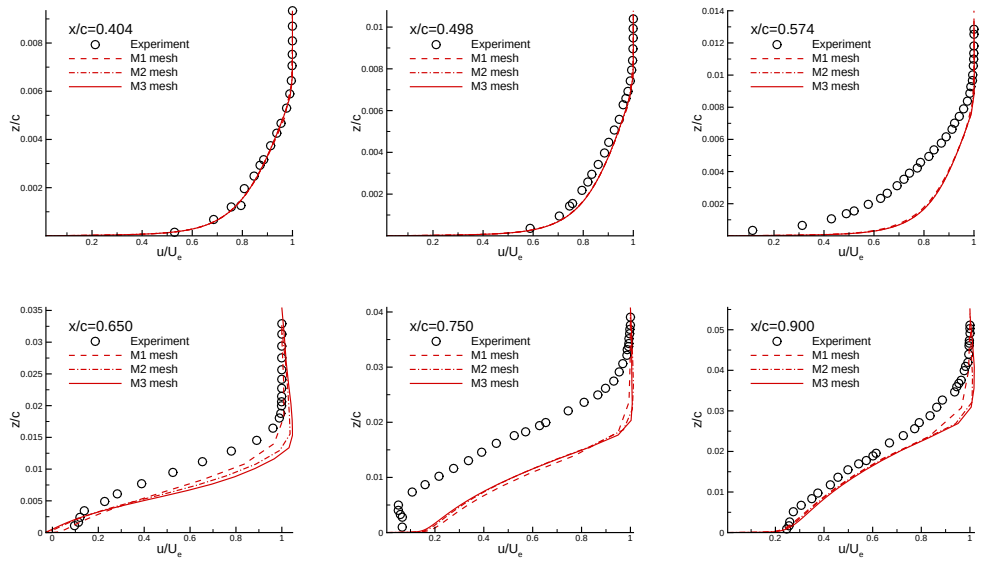

Figure 4.6: Grid convergence of the computed velocity profiles with fifth order WENO flux reconstructions, along the RAE2822 aerofoil surface.

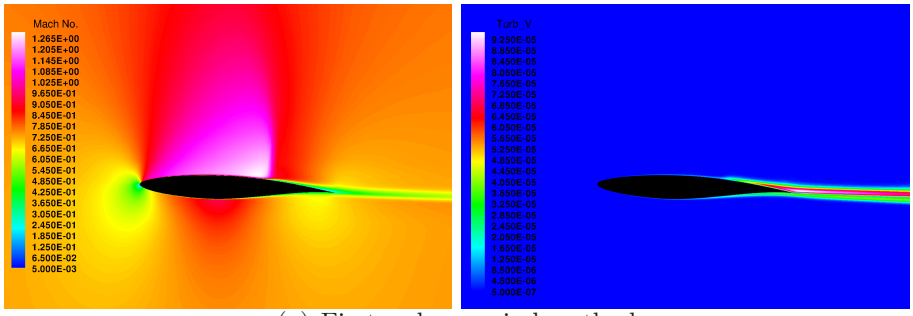

(a) First order upwind method

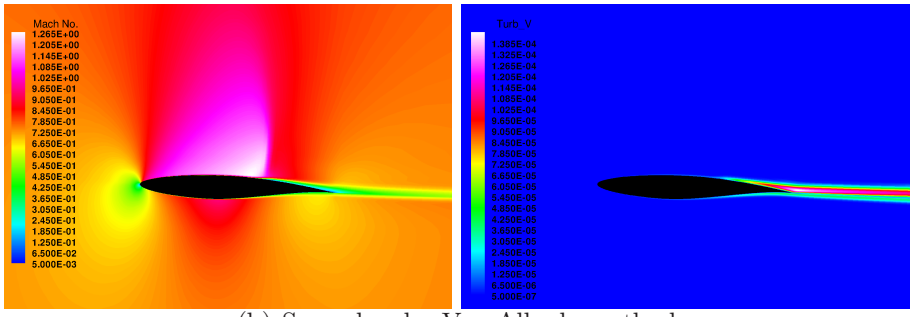

(b) Second order Van Albada method

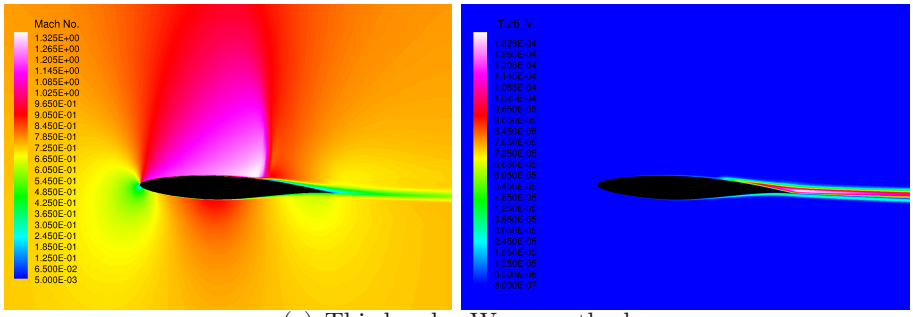

(c) Third order Weno method

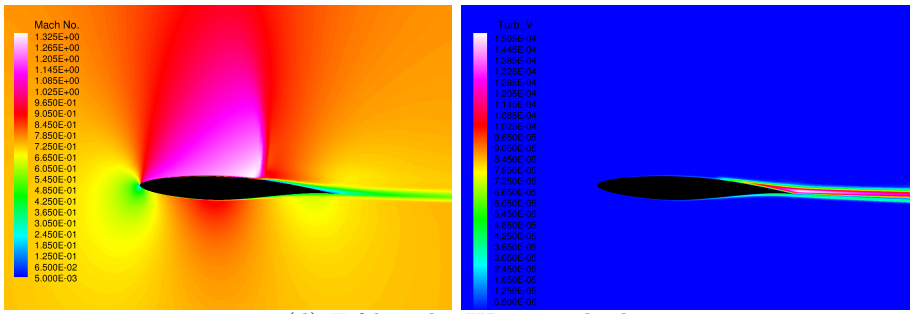

(d) Fifth order Weno method

Figure 4.7: Mach number (left) and eddy viscosity (dimensionless) (right) contours of the RAE2822 aerofoil at $M_\infty = 0.754$, $R_\infty = 6.2 \times 10^6$ and $\alpha = 2.57^o$as predicted by different order methods.

Figure 4.8 presents the comparison of the predicted surface pressure coefficient distribution of different orders of resolution. As shown in the plot, the higher resolution method compares more favorably to the experimental data. However, the $k-\omega$ model predicts the shock location further downstream than what was observed in the experiment. Furthermore, the poor pressure recovery, on the suction surface, downstream of the shock indicates that the model fails to predict reattachment of the flow. In all calculations the leading edge peak is not captured correctly, which is mainly attributed to the fact that transition was not modelled and further demonstrates the limitations of the turbulence model. The aforementioned deficiencies of turbulence modelling, are also reported in the published works of Spalart and Almaras [49] who compared their one equation model against the models of Baldwin and Lomax [46] and Johnson and King [47], Moryossef and Levy [97] who used the TNT model of Kok [75], Catalano and Amato [98] who investigated several $k-\omega$ and $k-\epsilon$ models, and also in the work of Lien and Kalitzin [99] who used the more elaborate υ^2-f, four equation, eddy viscosity model.

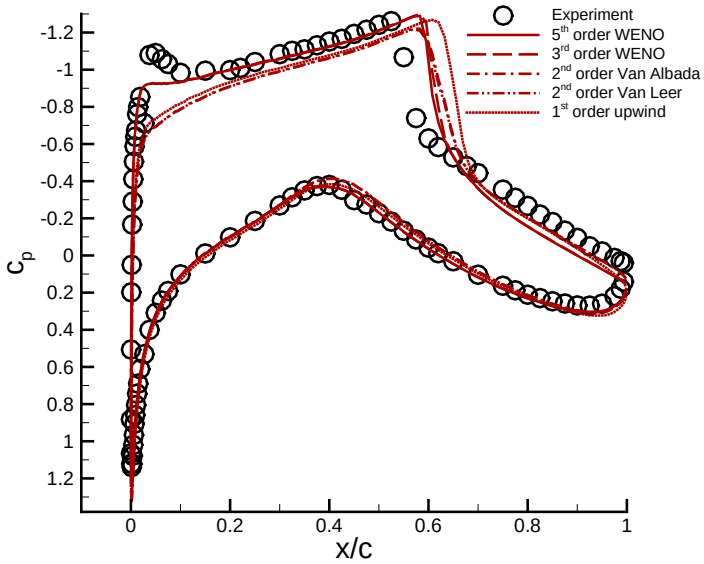

Figure 4.8: Computed and measured pressure-coefficients distribution along the RAE2822 surface.

Besides the well known limitations of the eddy viscosity models, each method converged to a different result manifesting that the solution is dominated by the underlying numerics. It is remarkable that the increase of the numerical resolution improves significantly the predictions in terms of shock location, and pressure distribution both near the leading edge and trailing edge. It is also noteworthy that the pressure distribution predicted by the high resolution fifth order WENO scheme is much less sensitive to the grid resolution than the more diffusive first and second order schemes (see Figures 4.3-4.6). The same is true for the calculated velocity profiles along the suction surface of the aerofoil. Therefore, an assumption can be made at this point that the additional cost of the computationally more expensive WENO scheme can be, somewhat, counterbalanced by the use of a much coarser grid than what would be normally used for a widely commissioned second order scheme to produce results of similar quality.

A comparison of the calculated stream-wise velocity profiles at various stations along the upper airfoil surface is shown in Figure 4.9. At stations $x/c = 0.404$ and $x/c = 0.498$ that are located upstream of the shock all resolution schemes perform similarly. The flow remains attached to the aerofoil surface and the velocity profiles agree well with the experiment. The same agreement in results is not evident in the case of locations that are stationed further downstream. The shock predicted is too far downstream, as indicated by the velocity profile at station $x/c = 0.571$, which is close to the shock. The TNT model fails to accurately predict the boundary layer growth, which is particularly apparent in the velocity profiles at stations $x/c = 0.650$, $x/c = 0.750$ and $x/c = 0.900$. Furthermore, the incorrect "hook" shape of the velocity profile in the defect layer indicates the inability of the model to resolve the mixing layer between the retarded recirculating fluid and the contiguous high momentum fluid. In fact, as the numerical resolution increases this effect becomes more profound as the turbulence model is inadequate of modelling the escalated mixing of momentum, dictated by the momentum equation. The slow growth and the unphysical sharp edge of the boundary layer reveal the inability of the model to predict separation correctly under adverse pressure gradients.

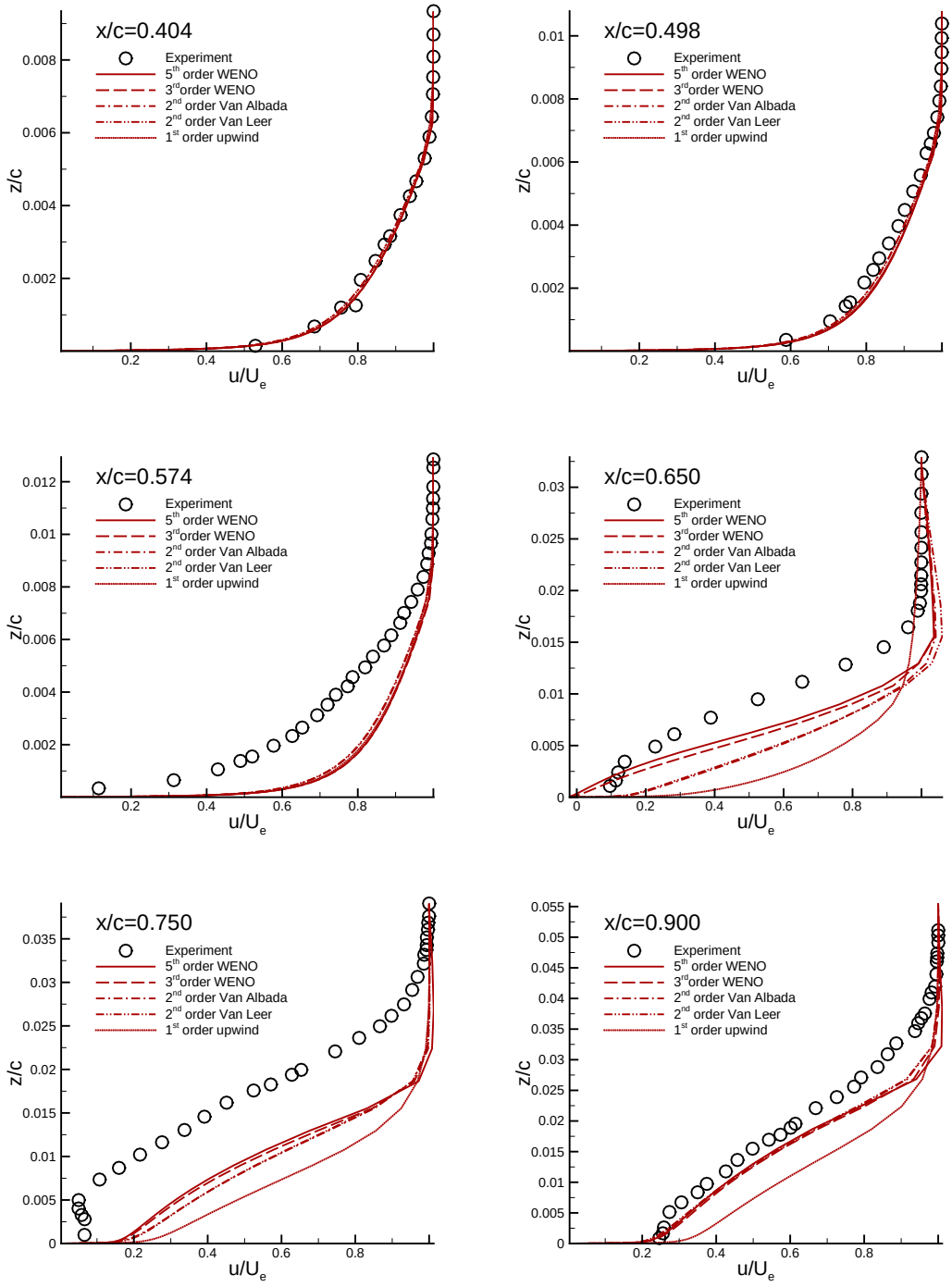

Figure 4.9: Computed and measured velocity profiles along the RAE2822 suction surface.

The integrated aerodynamic loads around the aerofoil surface using different of orders of accuracy on grids of varying resolution, are summarized in Table 4.2. The observed low errors for the lift coefficient obtained with the first order upwind scheme are incidental and are attributed to the incorrect pressure prediction near the shock and the high pressure value at the lower surface of the aerofoil's leading edge, as seen in Figure 4.2. This is further confirmed by the high values of the more sensitive drag and moment coefficients. By refining the grid, the discrepancies between the predicted and measured aerodynamic loads decrease. However, the relative errors of the first and second order scheme are considered high even for the fine grid.

In contrast, the higher order schemes perform very well, with the fifth order scheme indicating grid independent results, regarding the coefficient of lift, even on the coarse grid. The observed error increase of the drag and pitching moment coefficients predicted with fifth order WENO scheme is attributed to the precedence of viscous terms on the fine grids and possibly due to the interaction between the non uniform discretisations of the convective and viscous terms. Viscous terms become increasingly important when a turbulence model is employed since the numerical error associated with the viscous flux discretization is augmented by the turbulence viscosity quantity μ_t. A possible remedy would be a globally uniform accurate scheme. Nevertheless, the results in Table 4.2 highlight the superiority of the high resolution methods over the lower order methods.

The effect on accuracy of the high order methods when used in conjunction with a turbulence model is emphasized below. Table 4.3 compares the integrated aerodynamic loads of this work with the ones from Barakos [100] who investigated different turbulence models, with linear and non-linear constitutive relations, for the same case using comparable grids (260×80). Although striking, it is evident that the aerodynamic loads are more sensitive to the order of the convective flux reconstruction than to the turbulence model employed itself. The pattern here is similar; lower resolution schemes tend to underpredict the coefficient of lift and overpredict the coefficient of drag, whereas higher order reconstructions are in a better agreement with the experimental values, with the fifth order scheme comparing more favorably with only 1.9 % relative error regarding both c_l and c_m. A value that is well within the experimental uncertainty.

Spatial Resolution	Grid	c_l (% error)	c_d (% error)	c_m(% error)
1^{st}order upwind	M1	0.701 (5.7)	0.0527 (117.8)	-0.124 (17.0)
	M2	0.737 (0.8)	0.0467 (93.8)	-0.126 (18.9)
	M3	0.749 (0.8)	0.0433 (78.9)	-0.125 (17.9)
2^{nd}order Van Albada	M1	0.653 (12.1)	0.0514 (112.4)	-0.117 (10.4)
	M2	0.689 (7.3)	0.0448 (85.1)	-0.117 (10.4)
	M3	0.704 (5.2)	0.0412 (70.2)	-0.117 (10.4)
2^{nd}order Van Leer	M2	0.685 (7.8)	0.0446 (84.3)	-0.116 (9.4)
3^{rd}order WENO	M1	0.757 (1.9)	0.0286 (18.2)	-0.114 (7.5)
	M2	0.749 (0.8)	0.0272 (12.4)	0.110 (3.8)
	M3	0.753 (1.3)	0.0274 (13.2)	-0.112 (5.7)
5^{th}order WENO	M1	0.729 (1.9)	0.0257 (6.2)	-0.104 (1.9)
	M2	0.741 (0.3)	0.0263 (8.7)	-0.107 (0.9)
	M3	0.746 (0.4)	0.0268 (10.7)	-0.109 (2.8)
Experiment		0.743	0.0242	-0.106

Table 4.2: Spatial resolution and grid dependency effect on the lift and drag coefficients of the RAE2822 aerofoil.

Turbulence Model	c_l (% error)	c_d (% error)	c_m(% error)
$k-\omega$ TNT (current, WENO5)	0.729 (1.9)	0.0257 (6.2)	-0.104 (1.9)
Non -Linear $k-\epsilon-A_2$ (Barakos)	0.802 (7.9)	0.0301 (24.4)	-0.110 (3.8)
Non -Linear $k-\epsilon$ (Barakos)	0.813 (9.4)	0.0312 (28.9)	-0.112 (5.7)
One equation SA (Barakos)	0.803 (8.1)	0.0322 (33.1)	-0.113 (6.6)
Experiment	0.743	0.0242	-0.106

Table 4.3: Lift drag and pitching moment coefficients of the RAE2822 aerofoil.

Overall, the results obtained with the fifth order WENO scheme are in better accordance with the experimental data. The observed discrepancies are mainly attributed to the assumed linear dependency of the Reynolds stress to the mean strain rate tensor, via the Boussinesq relation. The isotropic assumption of turbulence is no longer valid at high strain rates, caused by rapid dilatation and streamline curvature. This condition renders any linear constitutive turbulence model

unreliable for separated flows, especially for shock-induced separation where a multitude of flow phenomena are present.

An estimate of the CPU time required by the different convective flux reconstruction methods to run a fixed number of iterations is summarized in Table 4.4. The first order upwind method on the coarse M1 grid is considered as reference. The CPU time increases linearly with respect to the order of the method, since for the higher order methods more floating point arithmetics are performed. However, the effect of increasing the grid resolution is much more profound in terms of computational cost. Therefore the required CPU time of the lower order schemes to run on the fine grid is significantly greater to the time that the fifth order WENO reconstruction required to run on the coarse grid or even on the medium grid. If one considers that the more grid sensitive lower order methods require much finer grids to produce results of similar quality to the higher resolution schemes, then the assumption made earlier is valid. That is, the additional cost of the fifth order WENO scheme can be, indeed, counterbalanced by the use of a much coarser grid than what would be normally used for a lower order method to yield comparable results. In that sense, it turns out that the higher resolution methods is much more efficient.

Spatial Resolution	Grid	CPU time
1^{st}order upwind	M1	1.000
	M2	2.059
	M3	3.570
2^{nd}order Van Albada	M1	1.016
	M2	2.103
	M3	3.757
3^{rd}order WENO	M1	1.096
	M2	2.213
	M3	3.819
5^{th}order WENO	M1	1.144
	M2	2.448
	M3	4.169

Table 4.4: Reconstruction CPU time

4.2 Subsonic flow over the NACA 4412 aerofoil

The next case considered is the subsonic flow around the NACA 4412 aerofoil near maximum lift, as an example of a two dimensional high-lift aerofoil with flow separation. Experiments regarding this case were conducted by Coles and Wadcock [101] at subsonic flow conditions at a Reynolds number of $Re_\infty = 1.52 \times 10^6$ and an angle of incidence $\alpha = 13.87^o$. This is a computationally challenging case since turbulence models tend to predict time dependent results at the separation region as the spatial resolution is increased. The same case has been chosen as the basis of validation and assessment of different turbulence models such as the original $k - \omega$ model by Menter [76] and the non-linear EARSM model of Hellsten and Laine [102]. Kim et al. [103] used this test case to benchmark linear $k - \epsilon$ and $k - \omega$ models while Schmidt et al. [104] performed LES around a NACA 4412 aerofoil to evaluate subgrid-scale models. However no wind tunnel corrections have been reported in the literature.

To examine grid convergence, three grids comprising of 277×65, 397×95 and 512×125 control volumes were used for the computations and are illustrated in Figure 4.10. Similar to procedure in Section 4.1 the spatial resolution of the numerical scheme was gradually increased by employing first, second, third and fifth order flux reconstructions. Figures 4.11 - 4.15 demonstrate the grid sensitivity of each scheme via surface pressure coefficients distribution and streamwise velocity profiles. Consistent with the observations made for the RAE 2822 transonic case, grid sensitivity decreases asymptotically with increasing the order of accuracy. First and second order methods behave similarly, showing high dependence on the resolution of the grid, while the third and fifth order WENO schemes outperform the more diffusive lower order methods in terms of grid sensitivity.

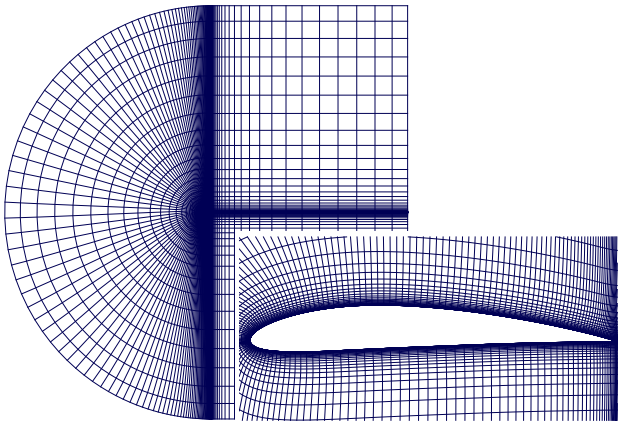

(a) NACAM1 mesh (277x65)

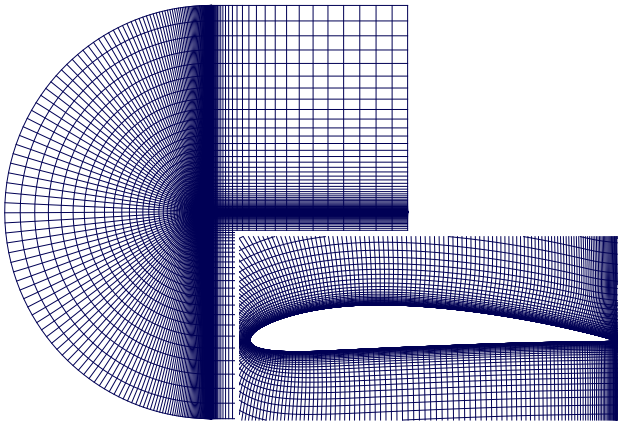

(b) NACAM2 mesh (397x95)

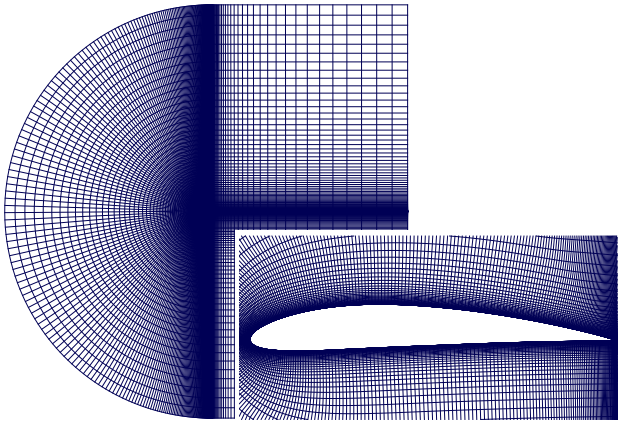

(c) NACAM3 mesh (512x125)

Figure 4.10: Full and close-up views of the NACA4412 meshes

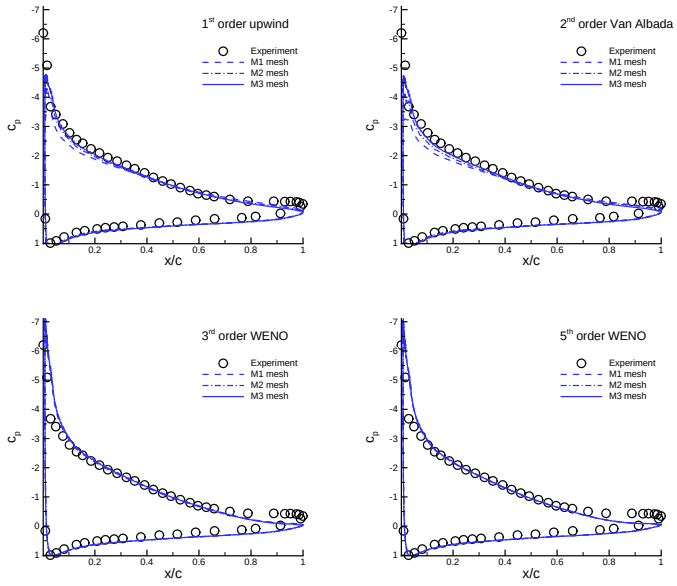

Figure 4.11: Grid convergence of the computed pressure-coefficient distributions along the NACA 4412 aerofoil surface.

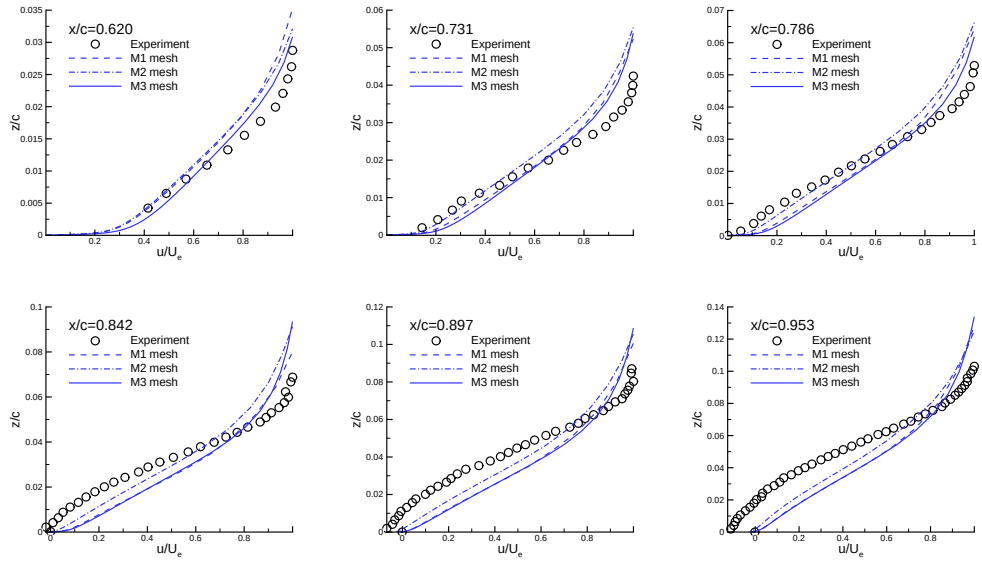

Figure 4.12: Grid convergence of the computed velocity profiles with first order upwind flux reconstruction, along the NACA 4412 aerofoil surface.

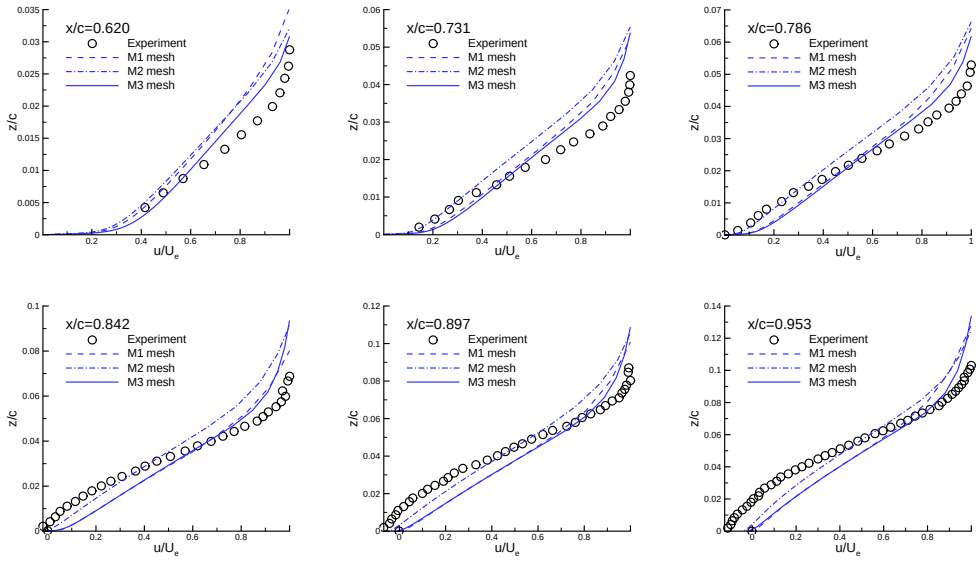

Figure 4.13: Grid convergence of the computed velocity profiles with second order Van Albada MUSCL flux reconstructions, along the NACA 4412 aerofoil surface.

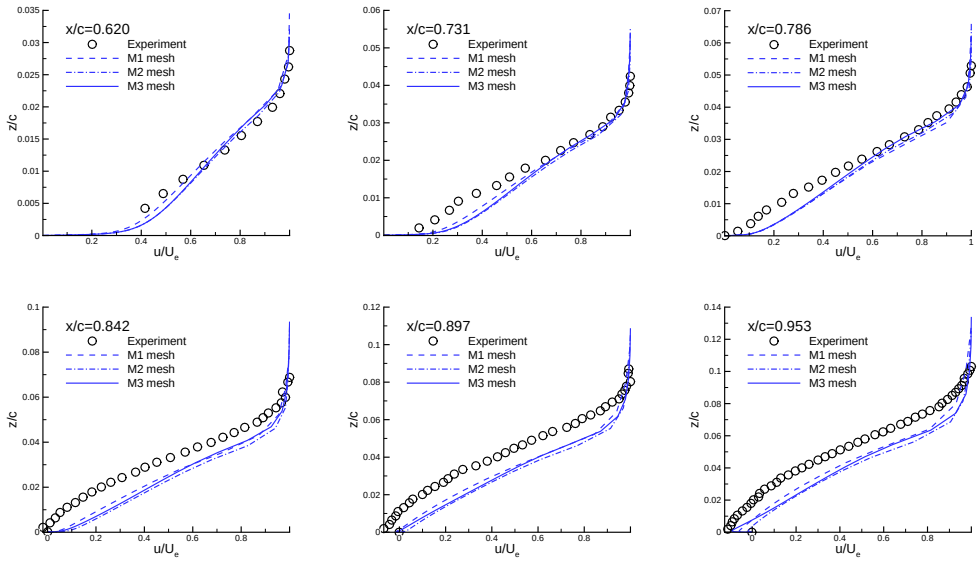

Figure 4.14: Grid convergence of the computed velocity profiles with third order WENO flux reconstructions, along the NACA 4412 aerofoil surface.

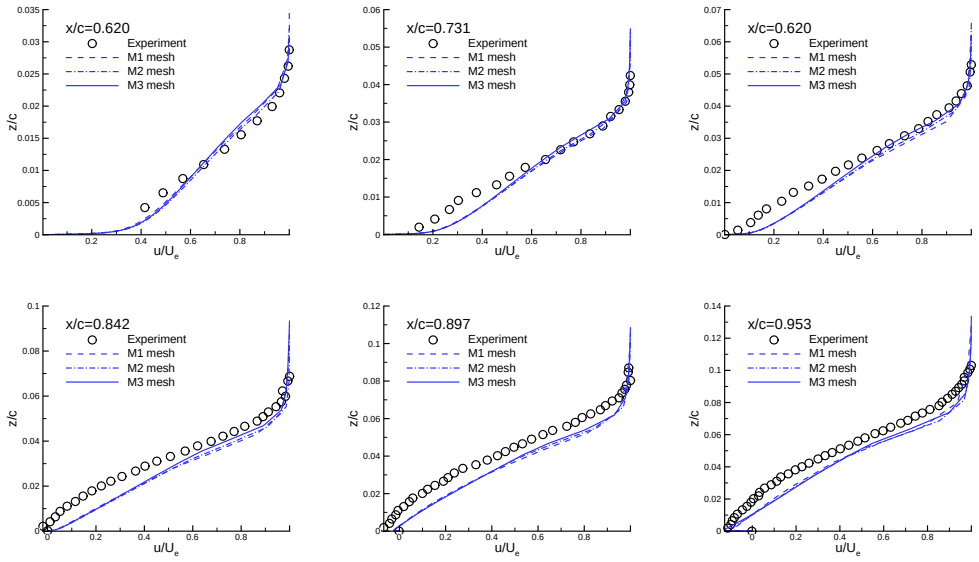

Figure 4.15: Grid convergence of the computed velocity profiles with fifth order WENO flux reconstructions, along the NACA 4412aerofoil surface.

A first qualitative comparison between the different resolution methods can be made by observing closely Figure 4.16 that represents eddy viscosity and Mach contours of the computed flow field. The flow scenery changes noticeably with respect to the order of resolution. First and second order methods predict similar flow fields to each other, whereas, as the order increases the flow is locally accelerated near the leading edge on the suction surface, more than what is observed with the lower order methods. Meanwhile the higher resolution methods, WENO3 and WENO5 result in a thinner wake while the turbulence quantities are convected further downstream, as indicated by the contours of eddy viscosity.

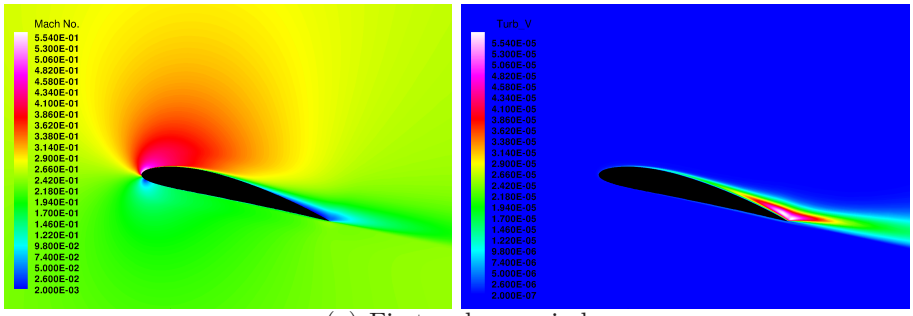

(a) First order upwind

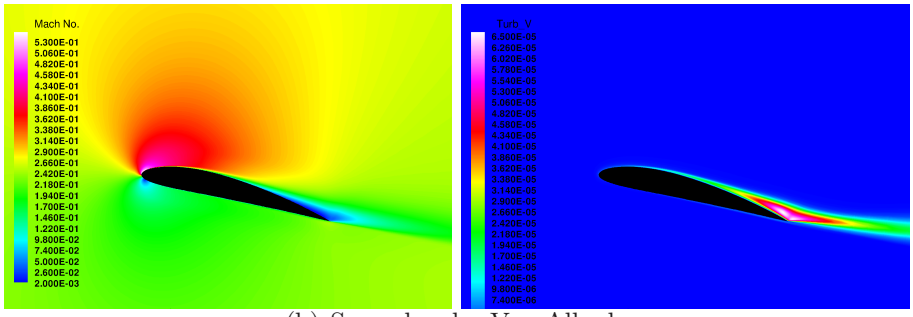

(b) Second order Van Albada

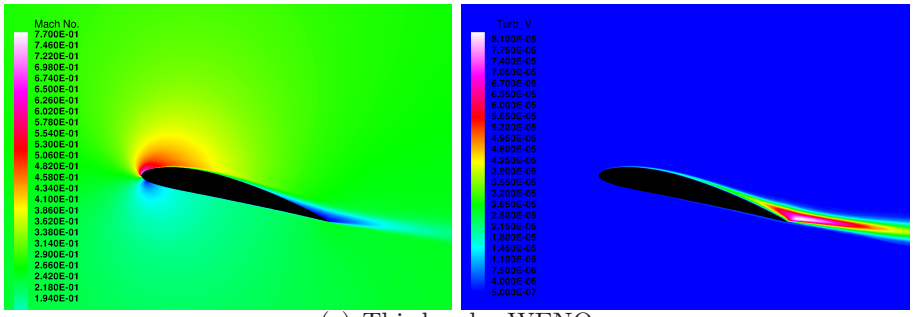

(c) Third order WENO

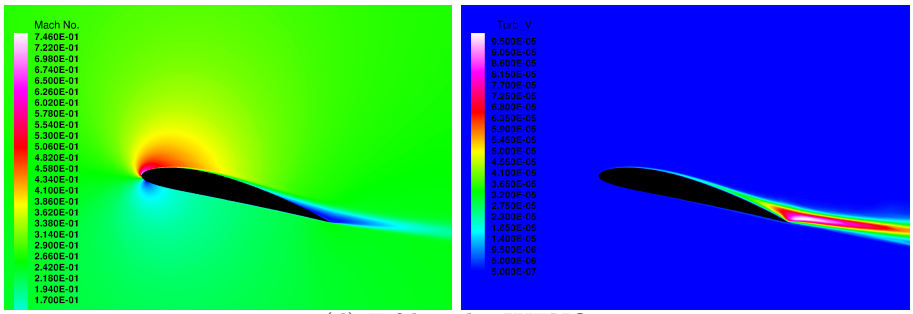

(d) Fifth order WENO

Figure 4.16: Mach number (left) and eddy viscosity (dimensionless) (right) contours of the Naca4412 aerofoil at $R_\infty = 1.52 \times 10^6$ and $\alpha = 13.87^o$as predicted by different order methods.

A direct comparison of the pressure coefficients curves, resulting from different resolution methods, is given in Figure 4.17. It is evident that the pressure plateau at the trailing edge is notably coupled with the suction peak near the leading edge of the aerofoil. The computations generally agree well with each other. However, all of the computed pressure curves do not match closely the measured distribution near the trailing edge, while visible discrepancies occur around the suction peak near the leading edge. Besides the slight overshoot at the leading edge and the coupled undershoot at the trailing edge the higher order WENO3 and WENO5 outperform the lower order methods.

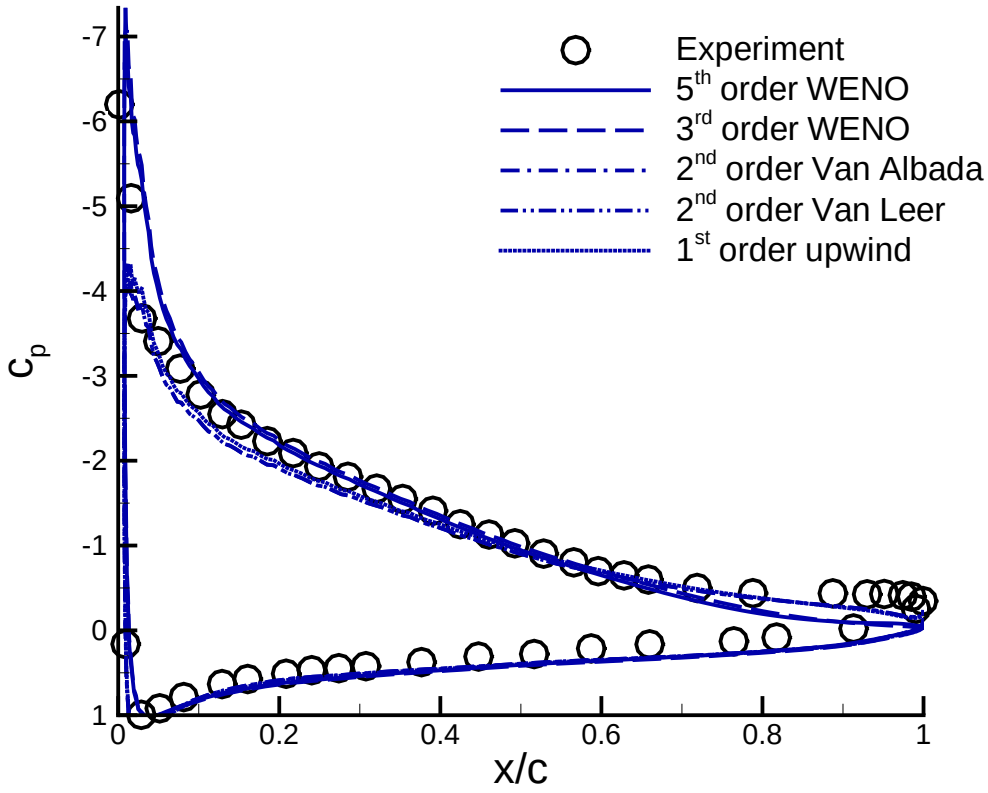

Figure 4.17: Computed and measured pressure-coefficients distribution along the NACA 4412 aerofoil surface

The effect of increasing the order of the method is more clearly seen in the plot of the velocity streamlines, Figure 4.18. The inherent diffusivity of the first and second order schemes in conjunction with the limitations of the turbulence model resulted in capturing a smaller, in extend, separation bubble towards the trailing edge of the aerofoil. On the other hand the higher resolution schemes, WENO3 and especially WENO5, predicted a separation bubble to a better agreement with what was observed in the experiment. This is justified by the velocity profiles studied next.

The velocity profiles are compared with experimental measurements at six stations on the suction surface. The sections are located at x/c =0.620, 0.731, 0.786, 0.842, 0.897 and 0.953, while the respective streanwise velocity profiles are shown in Figure 4.19. Discrepancies with the experimental profiles are evident for all stations. The first and second order methods predicted too retarded velocity profiles at stations located before the separation and at the same time the inherent diffusivity of these methods failed to capture correctly the separated flow. The separated flow is dominated by coherent structures that are different from the relatively ordered structure of attached boundary layers. For this reason the turbulence model employed, which is designed for boundary layers displays serious difficulties in modelling the separated motion accurately. By increasing the spatial resolution the mixing of momentum and the shear stress become more resolved in the recirculation area. This in turn explains why the fifth order WENO scheme results in a better agreement of the computed velocity profiles with the measured ones. However, even with the high resolution method, the maximum adverse streamwise velocity component is slightly low, which suggests an under estimation of the shear stress and shear strain, mainly due to the isotropic assumption inherent in the linear model that cannot simulate the behavior of near wall turbulence anisotropy.

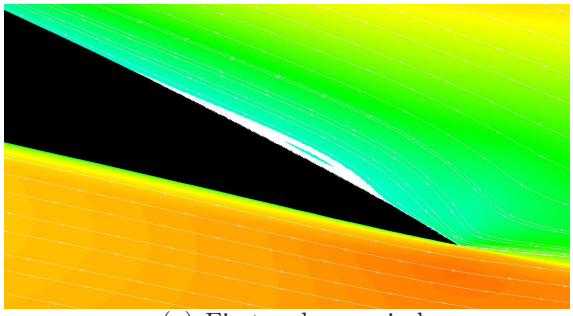

(a) First order upwind

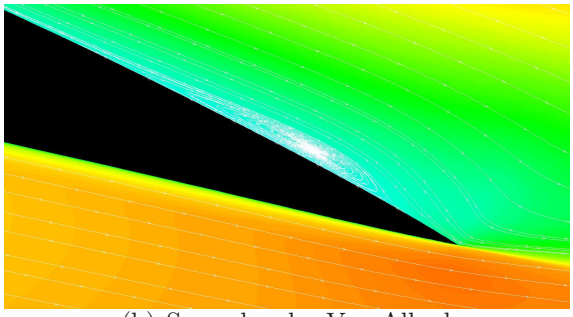

(b) Second order Van Albada

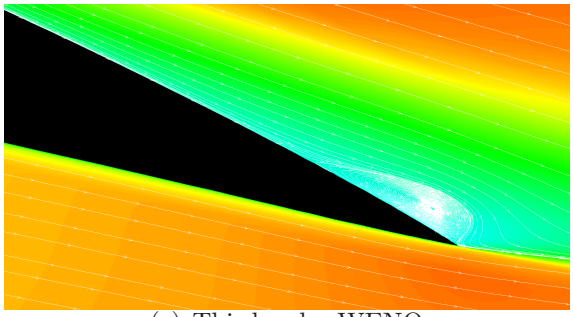

(c) Third order WENO

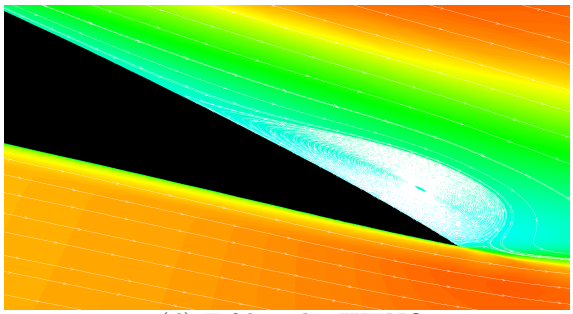

(d) Fifth order WENO

Figure 4.18: Effect of the order of resolution to the recirculating flow region near the trailing edge of the NACA 4412 aerofoil surface.

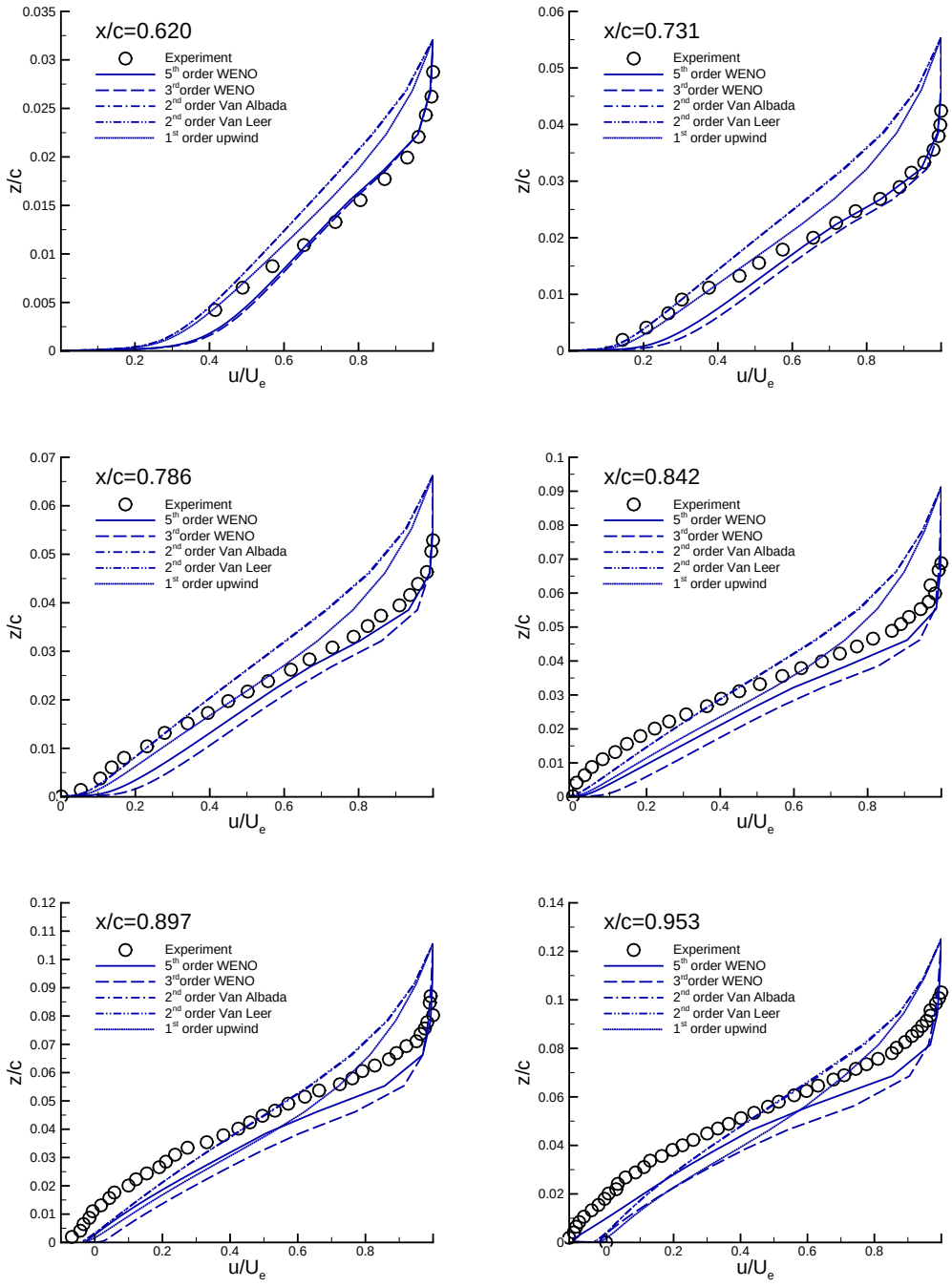

Figure 4.19: Computed and measured velocity profiles along the NACA 4412 suction surface.

A comparison of the integrated aerodynamic loads using different order methods and grids is given in Table 4.5. An obscure inconsistency with theory is noticed and regards the accuracy of the second order scheme with respect to the first order upwind scheme. One would expect the second order scheme to outperform the more diffusive first order scheme. Although in the transonic flow regime this is true (see Table 4.2), in the present subsonic simulation near maximum lift this is not the case. In fact the first order method predicts better lift coefficients than the second order methods, while the drag coefficients are comparable between the two schemes. Since in both cases grid convergence has not been achieved no decisive conclusions can be made. However, this abnormality in behavior is noteworthy.

Spatial Resolution	Grid	c_l (% error)	c_d
1^{st}order upwind	M1	1.588 (5.0)	0.1960
	M2	1.605 (3.9)	0.1507
	M3	1.651 (1.1)	0.1353
2^{nd}order Van Albada	M1	1.531 (8.7)	0.1939
	M2	1.557 (7.0)	0.1507
	M3	1.620 (3.0)	0.1336
2^{nd}order Van Leer	M2	1.556 (7.0)	0.1507
3^{rd}order WENO	M1	1.707 (2.2)	0.0427
	M2	1.742 (4.2)	0.0380
	M3	1.722 (3.1)	0.0383
5^{th}order WENO	M1	1.680 (0.6)	0.0375
	M2	1.686 (0.9)	0.0373
	M3	1.686 (0.9)	0.0375
Experiment		1.67	-

Table 4.5: Spatial resolution and grid dependency of the lift and drag coefficients of the NACA4412 aerofoil at $\alpha = 13.87^o$.

On the other hand the higher order methods prove to be more consistent both in terms of accuracy and grid sensitivity. The third order WENO scheme produces reasonable coefficients of lift, when compared to the experimental value, while the performance of the fifth order WENO scheme is remarkable; not only the 0.6 % error -resulting from the coarse grid computation- between the numerical and

measured c_l is within the experimental uncertainty but the values of lift and drag coefficients are virtually the same regardless of the grid resolution.

Table 4.6 compares the current computations with the calculations of Hellsten who used the same test case to validate his version of $k-\omega$ EARSM model using a grid that consisted of 320×96 control volumes, similar to the M2 grid used in this work. The relative comparison strengthens the hypothesis that at least in 2d RANS computations, the effect of high resolution methods is more profound than the turbulence model. Although Hellsten [44] employed a more sophisticated non-linear model, calibrated specifically for flows around high lift configurations, the relative discrepancies of the results, favor the present high resolution method coupled with a modest and thus computationally more efficient two equation linear model.

Turbulence Model	c_l (%error)	c_d
$k-\omega$ TNT (Current:WENO5)	1.686 (0.9)	0.0373
$k-\omega$ EARSM (Hellsten)	1.56 (6.6)	0.037
Experiment	1.67	-

Table 4.6: Comparison of lift and drag coefficients of the NACA4412 aerofoil.

Chapter 5

Active Camber Optimisation

Although CFD based aerodynamic optimisation has been performed by many authors, most of the times CFD methods of low flow-descriptive capacity have been used. To name a few, Bowen and Zhilde [105] performed multi objective optimisation of a transonic aerofoil using a combination of a potential and boundary layer method, while Kumar et al. [106] performed aerodynamic aerofoil shape optimisation using a hybrid variant of Genetic Algorithm and Ant Colony Optimisation coupled with a 2D meshless Euler solver. Hazra et al. [107] employed a gradient based optimisation using the Euler variant of the FLOWer CFD solver of the German Aerospace Center (DLR). In fact it has not been up to very recently that Epstein and Peigin [108] performed 3D optimisation on lifting surfaces using GA coupled with a full Navier-Stokes code that employed the incomplete algebraic turbulence model of Baldwin and Lomax. The same turbulence model has been also employed in the work of Kipouros [51], who performed TS optimisation on compressor blades.

It is clear that low order CFD methods and relatively simple turbulence models have been employed for their cost effectiveness, however the question that quickly rises is as to what expense, if any. Furthermore, a systematic approach to answer that question has not been performed, up to date. Having said that, the objective of the subsequent study is twofold: (a) to improve the aerodynamic performance of an aerofoil within the Active Camber concept, described in Chapter 1 and furthermost (b) to demonstrate that the use of high resolution CFD methods coupled with a meta-heuristic multi-objective optimisation algorithm,

can have significant impact on the resulting optimised shapes and hence on their aerodynamic performance.

5.1 Definition of the Optimisation Problem

As already outlined in Chapter 1, the performance requirements for the next generation helicopters include both higher forward flight speeds and more maneuverability, requiring higher lift loads on the retreating rotor blade. The additional loading can be accommodated by increases in the aerofoil section maximum lift coefficient and/or an increase in the blade solidity. Since a higher solidity results in greater blade weight and drag, improving, real-time, the lift capability of the aerofoil, by means of flow control, is the more efficient approach. Employing flow control in the sense of aerofoil morphing, the effective aerofoil geometry adjusts to the changing flow and load requirements. This allows to further explore the aerodynamic flow potential of the flight envelope resulting not only in aerodynamic performance gains but also in an improved structural design. The use of smart materials and structures can be used as an efficient means of achieving aerofoil morphing that can be reconfigured in response to changing conditions with potential aerodynamic benefits. A preliminary parametric investigation of the aerofoil morphing concept has been performed by Zachariadis et al. [109] that demonstrated potential performance gains.

Under the "FRIENDCOPTER" EUROPEAN FP6 project no (AIP3-CT-2003-502773) a new concept for an IBC actuator, the Active Camber concept, has been investigated with an emphasis on aerodynamic benefits. The variation of the aerofoil geometry is accomplished by a set of on-board piezoelectric actuators capable of moving the aerofoil surface. For the employed, non-disclosed, piezoelectric actuator design the active chord percentage, x_a, may be varied in the range of 80% to 20%. Furthermore, it is assumed that upward and downward actuation result in the same deflection shape neglecting asymmetries from aerodynamic loading or actuator design. What is more, the chord length of the aerofoil is assumed constant. With the above assumptions, a sixth order polynomial is

employed to parametrize the actively deformed camber line:

$$f(\bar{x}) = a_6\bar{x}^6 + a_5\bar{x}^5 + a_4\bar{x}^4 + a_3\bar{x}^3 + a_2\bar{x}^2 + a_1\bar{x} + a_0 \tag{5.1}$$

where $\bar{x} = \frac{x-(1-x_a)}{c-(1-x_a)}$ and c being the chord of the aerofoil.

The authority of the actuator is introduced by the maximum achievable non-dimensional deflection $z^*_{max} = z_{max}/c$ that varies depending on the actuator design: $-0.01 \leq z^*_{max} \leq 0.01$. The polynomial function (5.1) is scaled with the actuator authority thus forming the actual shape function,

$$\Phi(\bar{x}) = z^*_{max} f(\bar{x}) \tag{5.2}$$

that is superimposed to the skeleton line of the underlying aerofoil.

The optimisation effort was undertaken in order to identify the aerodynamic effectiveness in terms of servo effect c_m or direct lift effect c_l of the Active Camber concept when applied to the OA 312 aerofoil. In general the desired characteristics for an inboard region aerofoil of a main rotor blade are (a) the highest possible maximum lift coefficients at Mach numbers ranging from 0.3 to 0.5, for increased blade loading on the retreating side of the rotor disk and (b) pitching-moment coefficients nearly equal to zero, for low pitch-link loads and blade torsion loads [110]. In order to identify the aerodynamic characteristics of the baseline OA 312 aerofoil and to be able to specify the design goals of the present investigation, a set of two dimensional polars were computed.

Computations are performed at typical flow conditions encountered by the retreating blades on a full scale helicopter rotor. These conditions correspond to a Mach number of 0.4 and a Reynolds number of 3.0×10^6. For the polar computations the angle of attack varied between 8 and 15 degrees, while for increased accuracy the 5th order WENO scheme is employed for the discretization of the divergence of the inviscid fluxes. Table 5.1 compares the computed results at 9.8 and 10.5 degrees against experimental data that were provided by ONERA, an industrial partner within the FRIENDCOPTER project. The computed aerodynamic loads are in a close agreement with the experimental values. Therefore,

it is expected that the rest of the polar computations provide an accurate aerodynamic characterization of the OA 312 aerofoil. However, lack of experimental data for the entire polar set designate the last statement an unavoidable speculation. The computed polars are presented in Figure 5.1 and reveal that maximum lift occurs at 13.5 degrees, while the actual flow metrics for the datum design are: $c_l = 1.486,\ c_m = 0.004$ and $c_d = 0.0354$. Therefore the design goals of the present investigation are set to be: 1) $c_l > 1.5$ and 2) $c_m \simeq 0$.

	AoA (deg.)	c_l	c_m	c_d
Experiment (ONERA)	9.8	1.27	-0.0122	0.0137
	10.5	1.34	-0.0113	0.0149
Computational	9.8	1.29	-0.0125	0.0158
	10.5	1.35	-0.0115	0.0177

Table 5.1: Comparison between experimental and computational lift, drag and pitching moment coefficients for the baseline OA 312 aerofoil.

Having identified the design goals, the optimisation task can now be described as a constrained bi-objective minimization problem, with the following objective functions:

$$f_1 = -c_l \ , \tag{5.3}$$

$$f_2 = |c_m| \tag{5.4}$$

Obvious constraints of the current optimisation task are the active part of the aerofoil and the authority of the piezo-electric actuator:

$$20\% \leq x_a \leq 80\% \tag{5.5}$$

$$-0.01 \leq z^*_{max} \leq 0.01 \tag{5.6}$$

A not so obvious constraint, is related to the amplitude of the polynomial itself. It is imperative that the maximum deflection of the polynomial shape does not exceed unity, in order to prevent large deformations that are not realizable by the piezoelectric actuator. This constraint is clearly satisfied by setting $a_0 = 0$

and most importantly by:

$$\sum |a_n| \leq 1, \ with \ n = 1, ..., 6 \tag{5.7}$$

In fact, this constraint will turn out to be very stringent, since it limits considerably the allowable design variable step-size.

Besides the identification and definition of the objectives and constraints of the optimisation problem and the parametrization of the datum geometry, an efficient mesh generation process is necessary to create the computational domain around the deforming body. Generating a grid by means of an elliptic method or other iterative methods for each new design vector is a non-trivial and time consuming task. The geometry of the aerofoil must be updated frequently during the optimisation cycle. In fact, the number of mesh generations required is proportional to the number of design variables. Therefore, it is imperative to keep the method simple, fast and robust. It is also essential that the computational meshes are of high quality in order not to impair computational accuracy. Subsequently, a method of propagating geometric perturbations into an existing high quality initial grid while preserving the initial grid characteristics is employed and presented below.

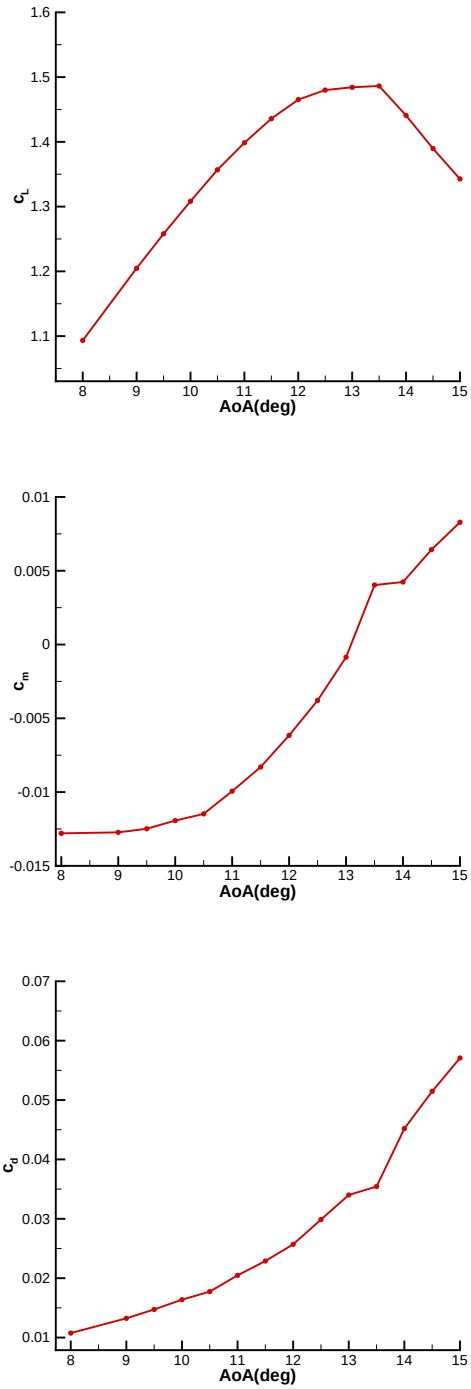

Figure 5.1: OA312 2D polars at Mach =0.4 and Re=3.0×10^6, at various angles of attack (AoA).

5.2 Arc-length Transfinite Interpolation

Assuming that the displacement of the vertexes and the edge of the aerofoil body is already defined by the design vector, the displacement of the interior points is computed by transfinite interpolation (TFI). Moreover the TFI is arc-length-based in order to preserve the characteristics of the initial grid.

A 2-d grid consists of a face {F}, edges {E} and vertexes {V} and is the connectivity relations between these elements that define the topology of the grid. Moreover, the face {F} is defined by:

$$\mathbf{X}^{\mathrm{F}} = \left\{ \overrightarrow{x}_{i,k} \middle| i = 1, ..., NI^{F} \, , k = 1, ..., NK^{F} \right\} \tag{5.8}$$

In the parametrization process, grid points are parametrized according to the global $i,\ k$ indices of the normalized arc-lengths $s,\ t$ respectively. Therefore the normalized arch-length in the i direction is defined as [111, 112]:

$$s_{i,k} = \frac{\sum_{m=2}^{i} \| \overrightarrow{x}_{m,k} - \overrightarrow{x}_{m-1,k} \|}{\sum_{m=2}^{NI} \| \overrightarrow{x}_{m,k} - \overrightarrow{x}_{m-1,k} \|} \tag{5.9}$$

with $s_{1,k} = 0$ and $s_{NI,k} = 1$. Similarly the normalized arch-length in the i direction is defined as:

$$t_{i,k} = \frac{\sum_{m=2}^{k} \| \overrightarrow{x}_{i,m} - \overrightarrow{x}_{i,m-1} \|}{\sum_{m=2}^{NK} \| \overrightarrow{x}_{i,m} - \overrightarrow{x}_{i,m-1} \|} \tag{5.10}$$

with $t_{i,1} = 0$ and $t_{i,NK} = 1$.

Following the parametrization process and the already known edge and corner point deformations of the newly deformed body, a one dimensional linear projector which computes the displacements in the i- direction can be defined as [113]:

$$P_{\xi}\left(i,\ k\right) = \overrightarrow{dx}^{i}\left(i,\ k\right) \ = \left(1 - s_{i,k}\right) \overrightarrow{dx}\left(1,\ k\right) + s_{i,k} \overrightarrow{dx}\left(NI,\ k\right) \tag{5.11}$$

while for the k- direction:

$$P_{\zeta}\left(i,\ k\right) = \overrightarrow{dx}^{k}\left(i,\ k\right) \ = \left(1 - t_{i,k}\right) \overrightarrow{dx}\left(i,\ 1\right) + t_{i,k} \overrightarrow{dx}\left(i,\ NK\right) \tag{5.12}$$

Having specified the uni-variate interpolations in each of the computational directions, what follows is the formation of the tensor products of the projectors. Therefore, forming the composite mapping $P_\xi P_\zeta$ (tensor product) of Eq.'s (5.11) and (5.12) such that:

$$\begin{aligned} P_\xi\left(P_\zeta\left(i,\ k\right)\right) = \ & \left(1-s_{i,k}\right)\Big[\ \left(1-t_{i,k}\right)\overrightarrow{dx}\left(1,\ 1\right)+t_{i,k}\overrightarrow{dx}\left(1,\ NK\right)\ \Big]+ \\ & s_{i,k}\Big[\ \ \left(1-t_{i,k}\right)\overrightarrow{dx}\left(NI,\ 1\right)+t_{i,k}\overrightarrow{dx}\left(NI,\ NK\right)\ \Big] \end{aligned} \tag{5.13}$$

It is easily shown that this tensor product is commutative, simply by collecting common terms:

$$\begin{aligned} P_\xi P_\zeta = \ & \left(1-t_{i,k}\right)\Big[\ \left(1-s_{i,k}\right)\overrightarrow{dx}\left(1,\ 1\right)+s_{i,k}\overrightarrow{dx}\left(NI,\ 1\right)\ \Big]+ \\ & t_{i,k}\Big[\ \left(1-s_{i,k}\right)\overrightarrow{dx}\left(1,\ NK\right)+s_{i,k}\overrightarrow{dx}\left(NI,\ NK\right)\ \Big] \\ = P_\zeta P_\xi & \end{aligned} \tag{5.14}$$

or in condensed form:

$$P_\zeta P_\xi = \ \left(1-t_{i,k}\right)\overrightarrow{dx}^{i}\left(i,\ 1\right)+t_{i,k}\overrightarrow{dx}^{i}\left(i,\ NK\right) \tag{5.15}$$

In essence, TFI is the Boolean sum of the previously defined projections:

$$\overrightarrow{dx}^{ik}\left(i,\ k\right) = P_\xi \oplus P_\zeta = \overrightarrow{dx}^{i}\left(i,\ k\right)+\overrightarrow{dx}^{k}\left(i,\ k\right)-P_\xi P_\zeta \tag{5.16}$$

$$\begin{aligned} \overrightarrow{dx}^{ik}\left(i,\ k\right) = \ & P_\xi\left(i,\ k\right) \ + \Big[\left(1-t_{i,k}\right)\overrightarrow{dx}\left(i,\ 1\right)+t_{i,k}\overrightarrow{dx}\left(i,\ NK\right)+\Big] \\ & \qquad -\Big[\left(1-t_{i,k}\right)\overrightarrow{dx}^{i}\left(i,\ 1\right)+t_{i,k}\overrightarrow{dx}^{i}\left(i,\ NK\right)\Big] \end{aligned}$$

By gathering common terms the 2-D TFI can be most easily defined as a two step recursion formula [114]:

$$\begin{aligned} \overrightarrow{dx}^{ik}\left(i,\ k\right) = \ & \overrightarrow{dx}^{i}\left(i,\ k\right) \ + \left(1-t_{i,k}\right)\Big[\overrightarrow{dx}\left(i,\ 1\right)-\overrightarrow{dx}^{i}\left(i,\ 1\right)\Big] \\ & \qquad +\ t_{i,k}\Big[\overrightarrow{dx}\left(i,\ NK\right)-\overrightarrow{dx}^{i}\left(i,\ NK\right)\Big] \end{aligned} \tag{5.17}$$

Finally, the displacements in the interior of the 2-D grid are defined as:

$$\overrightarrow{dx}\left(i,\ k\right) = \overrightarrow{dx}^{ik}\left(i,\ k\right) \tag{5.18}$$

5.2.1 Orthogonality Enforcement at solid boundaries.

Although TFI provides an efficient and robust way of grid deformation, it does not guarantee an orthogonal mesh near the solid boundaries. For the sake of computational accuracy, orthogonality at the boundary is enforced by the following procedure:

Consider a grid node on the boundary with co-ordinates $(x_1,\ z_1)$, at which the tangential gradient is calculated to be m_1, then the straight line normal to the boundary, through node $(x_1,\ z_1)$ has equation:

$$z - z_1 = -\frac{1}{m_1}(x - x_1) \tag{5.19}$$

Suppose that the corresponding node off the boundary has co-ordinates $(x_2,\ z_2)$ and a tangential gradient m_2. Then the straight line tangent to this node has equation:

$$z - z_2 = m_2(x - x_2) \tag{5.20}$$

By solving simultaneously Eq.'s (5.19), (5.20) orthogonality at the wall is enforced. However, this technique may result in severe slope discontinuities near the solid boundary. In order to circumvent this, a grid blending method is employed.

5.2.2 Grid Blending near solid boundaries.

At large deformations, crossover of cells may occur near the solid boundary or at sharp corners as in the trailing edge of the airfoil. In order to improve the quality of the grid near the wall and to prevent crossover of cells, a blending function is implemented. The blending function is a weighting function of the arc-tangent that makes the deformed grid lines extend the same angle from the surface as the original line and is defined as follows [115]:

$$F_1 = \frac{2}{\pi} tan^{-1}\left[\frac{k - k_{min}}{\frac{TRI}{NK}(k_{max} - k_{min})}\right]^{bp} \tag{5.21}$$

$$F_2 = \frac{2}{\pi} tan^{-1} \left[\frac{\frac{TRI}{NK} (k_{max} - k_{min})}{k - k_{min}} \right]^{bp} \tag{5.22}$$

where TRI is the transition index, k_{bmin}, k_{bmax} define the maximum and minimum grid index of the region where the blending is to occur, and bp, the blending power, is used to control the blending.

The blended values are given by the sum of the product F_1 with the non-blended grid points $\overrightarrow{x}(i,\ k)$ and the product of F_2 with the projection of the non-blended original grid points:

$$\overrightarrow{x}(i,\ k)^{blend} = F_1 \overrightarrow{x}(i,\ k)^{project} + F_2 \overrightarrow{x}(i,\ k) \tag{5.23}$$

Figure 5.2 below demonstrates the evolution of the deformed mesh and the impact that the developed analytic method has on the smoothness and orthogonality of the generated grid. In order to check the validity of the method at large, unrealistic, deformations the maximum displacement was defined to be $10 \times z^*_{max}$.

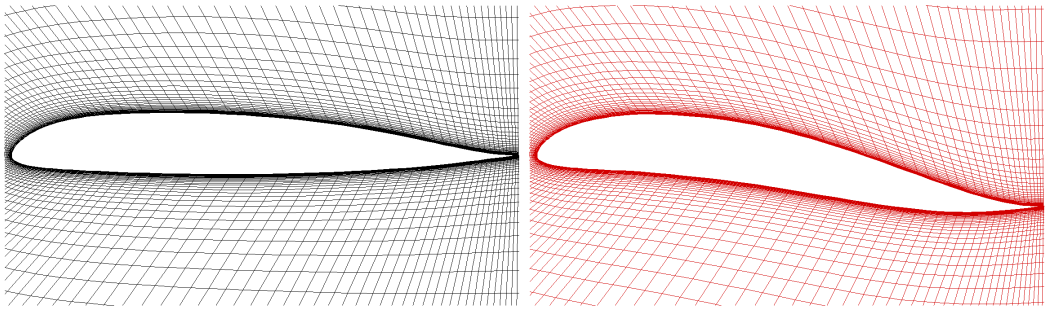

(a) Initial Mesh (b) Deformed Mesh

Figure 5.2: Demonstration of the TFI implementation.

5.3 Description of the Aerodynamic Optimisation System

The Multi-OBjective Integrated Design system (MOBID_2D) that was build for the needs of the present work consists of a series of codes, written in FORTRAN77, C and C++. It incorporates the recently developed CFD solver, described and

validated in Chapters 3 and 4, coupled with TS algorithm that has been developed by Jaeggi et al. [59], a simple and efficient geometry parametrization technique and a fast and robust analytic mesh perturbation method that is based on an arc length transfinite interpolation (TFI), detailed in the preceding Section 5.2.

The first step of the entire optimisation process is the parametrization of the initial geometry, that is the transformation of the active part of the aerofoil into the parametrized design vector. The produced design vector consists of 8 variables in total, of which the first two describe the chordwise length of the active part of the aerofoil and the authority of the piezoelectric actuator, whereas the next 6 variables define the actual shape of the active camber.

Soon after the parametrization process is complete, the master, optimiser, and the slave, CFD solver, processes of the parallelized optimisation application are initialized. In the master process the optimisation problem is defined, according to which the objective functions, design variables and initial design vector are assigned and the initial step size of the design parameters are set. The Multi-Objective Tabu Search (MOTS) libraries are invoked and the optimisation process is started, at which point the slave processes are launched. The main characteristic of the slave process is the CFD interface that is effectively the communication medium between the optimiser and the CFD solver. It receives the design vector from the optimiser and tranceives the objective function values, evaluated by the flow solver. On receipt of a new design vector the computational mesh is deformed according to the geometry specification. Then a detailed CFD analysis is performed. Based on this simulation, the objective functions are evaluated and passed on to the optimiser. The optimiser generates the new design vector, that is in turn evaluated. This loop continues until a stopping criterion is met. Figure 5.3 presents a schematic description of the main components of the design system.

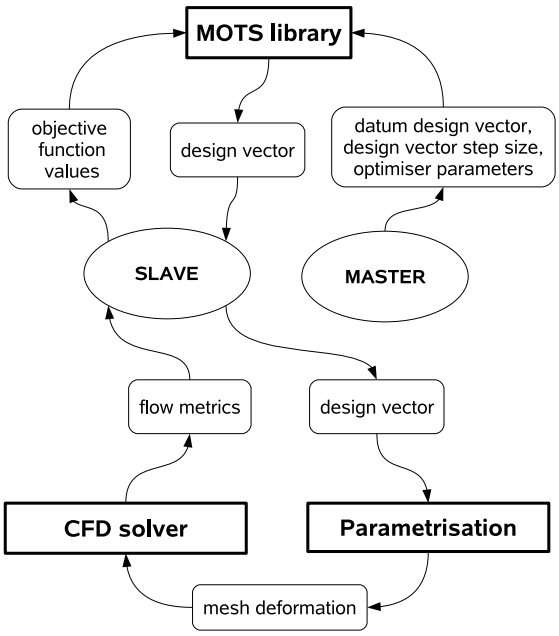

Figure 5.3: Design Core System flowchart.

5.4 Bi-objective Optimisation of the OA312 aerofoil

One of the main objectives of this research effort is to investigate the effect that high resolution CFD methods have on the optimised shapes and aerodynamic performance, resulting from an optimisation process whereby the CFD solver is coupled with a state-of-the art heuristic optimisation algorithm. For this reason a methodical investigation was undertaken. The optimisation process, described in the preceding chapters, was performed with gradually increasing the spatial resolution of the numerical scheme by employing second, third and fifth order inviscid flux reconstructions. Meanwhile, for consistency reasons, the same computation mesh was used in all of the variants of the optimisation system.

The number of CFD iterations in conjunction with the number of the grid nodes have great impact on the computational cost while the optimisation process progresses. However, as observed in Chapter 4 the effect of increasing the

resolution of the grid is more constraining in terms of CPU time than the effect of increasing the order of the numerical method. Therefore and in order to keep the optimisation cost to a minimum without comprising in accuracy, computation grids comprising 280×90 control volumes have been employed for all of the optimisation cycles. At this point, it should be stressed that the grid used for the present investigation is considered much finer than what is generally used for CFD based optimisation - Peigin & Epstein [108] and Hazra et al. [107] performed CFD based optimisation using grids that consisted of 81×25 and 193×33 control volumes, respectively. This adds another level of confidence regarding the reduction of numerical errors in the CFD simulation and allows to investigate solely the effect of varying the order of the numerical method.

To increase computational efficiency of the process, the CFD computations during each optimisation step are restarted from the converged solution of the datum design, obtained with the highest resolution method available in the solver. For each optimisation process, the initial design vector corresponds to the baseline geometry and the flow metrics resulting from the very first CFD evaluation are used to aerodynamically characterize the datum design. Therefore, it is expected that the objective functions of the datum design will vary with respect to the nominal order of accuracy of the CFD method.

Ideally the reduction of the residuals should be brought down to machine zero. However, this would result in significant time costs. In this work, the convergence criterion for the CFD simulation is the reduction of the residuals under a predefined threshold. Numerical experiments have shown that reducing the total maximum residual by five orders of magnitude, the flow metrics of interest remained constant. Furthermore, a maximum number of iterations is specified in order to avoid possible stagnation of the pseudo-unsteady time marching scheme due to potential flow unsteadiness, which would significantly increase computational time. Each CFD evaluation stage terminates when either the residual convergence criterion is met or the maximum number of iterations is reached. Moreover, to assure that no fictitious optima are obtained when the convergence criterion is not met, an exception flag is passed on to the optimiser that neglects the non-converged designs, which constitute the infeasible design vectors of the optimisation process.

The findings of the optimisation processes are summarized in Figures 5.4 - 5.6, which correspond to the second, third and fifth order CFD method employed in the optimisation design system, respectively. Qualitative similarities and differences in the optimisation search pattern between the different optimisation processes are visible. All of the optimisation variants display numerous discontinuities in the search pattern and the Pareto front that is indicative of the non-linear nature of the aerodynamic problem. The observed gaps in the search pattern is attributed to geometrically and aerodynamically infeasible designs as well as aerofoil designs of poor aerodynamic performance. The high density areas of the search pattern is a combined result of the stringent constraint, defined in Eq. 5.7, and the small step size of the design vector. However, the compromise design areas of all optimisation variants, are well explored and the corresponding aerofoil shapes cover a wide range of the Pareto fronts. Moreover, it is apparent that improvements in both the objective functions have been achieved relative to the datum design for each of the optimisation variants. The aforementioned commonalities are attributed to the effectiveness of the optimisation algorithm employed as well as in the nature and definition of the optimisation problem.

On the other hand significant differences are observed as the numerical accuracy is increased. In terms of computational time it is evident that the 2^{nd} order optimisation variant performed the most CFD evaluations when compared with the higher order variants. This testifies the computational efficiency of the lower order method. This is expected since the larger discretisation stencil of the higher order methods increases the floating point operations. More important however, is that the results of the search pattern changes noticeably with respect to the order of resolution of the CFD method. From the results of 5^{th}order optimisation variant, Figure 5.6, it is clear that the design space is strongly constrained in the region where designs with the lowest absolute pitching moment occur. In fact, the resulted feasible designs have similar values of this objective function and the trade-off surface in this area is almost horizontal, indicating that small improvements in pitching moment are obtained at the cost of lift deterioration. A similar behavior in results is observed from the 3^{th}order optimisation variant, Figure 5.5, where the achievable trade-off between lift and minimum absolute pitching moment is manifested through a clear discontinuity in the Pareto

front. On the contrary, the Pareto front resulted from a 2^{nd} order accurate CFD evaluations exhibits a nearly linear relation between minimum moment and lift coefficient. This indicates that although significantly more optimisation steps have been performed, the inherent diffusivity of the lower order method, failed to accurately predict the flow metrics. As a result the optimisation search pattern got trapped in a local optimum but globally sub-optimum region, at least as far as the minimisation of the pitching moment is concerned.

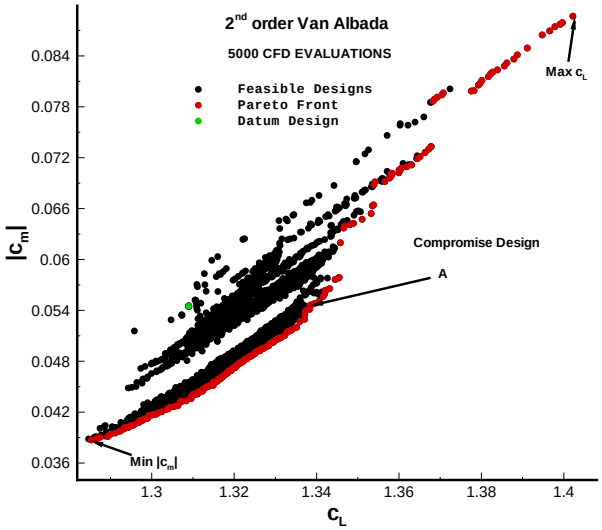

Figure 5.4: Optimisation Search Pattern: Feasible Designs and the Pareto Front as resulted from the 2^{nd} order Van Albada CFD method.

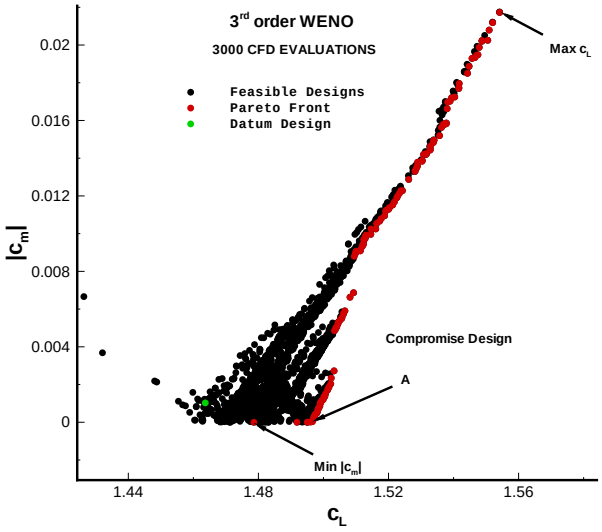

Figure 5.5: Optimisation Search Pattern: Feasible Designs and the Pareto Front as resulted from the 3^{rd} order WENO CFD method.

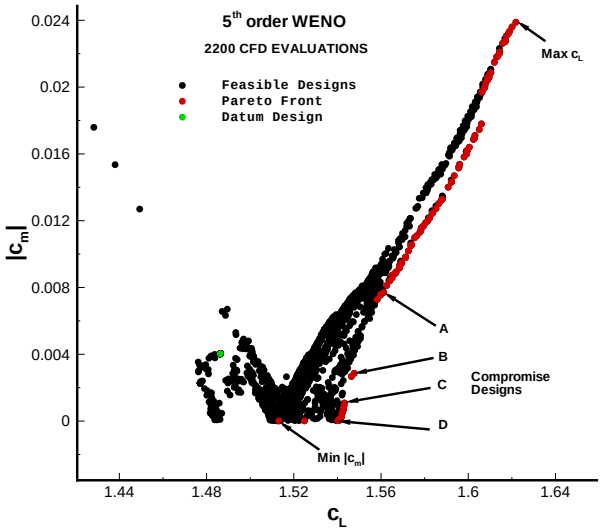

Figure 5.6: Optimisation Search Pattern: Feasible Designs and the Pareto Front as resulted from the 5^{th} order WENO CFD method.

5.5 Discussion of Results

To draw a more decisive conclusion on the effect that high resolution methods have on aerodynamic shape optimisation, a comparative analysis of the optimum designs obtained by different optimisation cycles has been performed. The optimum, as well as a compromise design that were the outcome of the optimisation process, using low resolution methods, have been numerically investigated using the higher resolution method available in the present computational method, namely the fifth order WENO scheme. Figures 5.8 - 5.19 display the geometric characteristics of the optimum designs along with pressure coefficient distributions and the resulting flow field, while Table 5.2 summarizes the flow metrics of this analysis.

The optimised aerofoil geometries found with the 5^{th} order WENO scheme are presented in Figures 5.14 - 5.19, which show, respectively, the highest coefficient of lift, the lowest, in absolute value, pitching moment coefficient design and compromise designs for the trade-off, Pareto, surface. These aerofoil designs are quite different to the baseline geometry and in addition there are significant differences amongst them. The aerofoil design for the highest lift has a completely different camber variation, compared to the design for lowest absolute pitching moment. In contrast the compromise designs display similar geometrical characteristics with each other.

Comparing Figures 5.8, 5.11 and 5.14, it is evident that the maximum lift designs resulting from the different optimisation processes show similar geometric characteristics, whereas this is not true for the designs corresponding to minimum moments coefficients as can be seen from Figures 5.8, 5.12 and 5.15. The latter manifests the sensitivity of the moment coefficient objective function to the employed resolution of the numerical method.

There are some general geometrical characteristics that distinguish the optimum designs from the baseline aerofoil design. Geometries that result in a higher camber tend to exhibit higher lift coefficient. The flow is accelerated on the suction surface increasing the lift, drag and moment coefficients. Furthermore throughout the optimisation processes maximum lift coefficients are obtained with

almost maximum piezo-electric actuator authority. Meanwhile the design variable that corresponds to the extension of the active part of the camber reaches the lower part of the constraint, which makes the effect of the actuator authority more profound, as it is observed from Figures 5.8, 5.11 and 5.14. On the other hand the minimisation of the more sensitive pitching moment coefficient requires more subtle geometric changes dictating mediocre piezo-electric authority and active camber width as can be seen from Figure 5.15.

The changes made to the aerofoil geometry during the search demonstrate the flexibility of the geometry parametrization system used, while the geometrical differences amongst the optimal designs indicate the richness of the design space and highlight the need for an efficient optimisation tool to support the designer in exploring the design space.

Table 5.2 summarises the flow metrics of the optimisation investigation. Overall, it is observed that the attainment of higher lift is in conflict with the need for low drag coefficients and pitching moment characteristics. Furthermore it is obvious that high accuracy CFD methods result in optimised shapes that outperform significantly the datum design. On the other hand the lower order methods, can yield designs that satisfy the first objective, while they fail to meet the second design goal, that is pitching moments nearly equal to zero. In fact, even the minimum c_m designs of both the 2^{nd} and 3^{rd} order methods yield higher pitching moments than the datum design. This in turn is attributed to the incorrect evaluation of the initial flow metrics of the datum design and illustrates the deterministic nature of the optimisation process,i.e., the entire optimisation process and the resulting search pattern are highly dependent on the initial flow metrics of the datum design configuration.

CFD method	Design	c_l	c_m	c_d
	Datum	1.48625	0.00403	0.03543
5^{th}Order	Max. c_l	1.62183	-0.02388	0.04079
	Min. c_m	1.51211	-0.00002	0.03671
	Comp. A	1.55664	-0.00763	0.03889
	Comp. B	1.54586	-0.00244	0.03888
	Comp. C	1.54126	-0.00063	0.03874
	Comp. D	1.53842	0.00039	0.03857
3^{th}Order	Max. c_l	1.598101	-0.017023	0.039646
	Min. c_m	1.504994	0.004946	0.036718
	Comp. A	1.526962	0.004888	0.038101
2^{th}Order	Max. c_l	1.637523	-0.027933	0.041407
	Min. c_m	1.452454	0.023553	0.034088
	Comp. A	1.52236	0.006204	0.037963

Table 5.2: Aerodynamic Loads Comparison between optimum shapes resulted from different order methods.

Nevertheless, it is noteworthy that the more diffusive second order method has resulted in an optimum shape that performs better with respect to c_l than WENO5. Although the relative difference between the two methods is a merely 0.9 %, this observation cannot be neglected or be thought of as incidental. In fact the comparison of the coefficients of pressure distribution, in Figure 5.7, depicts the physical reasoning behind this finding. Although the pressure distributions match closely, there is a noticeable difference in the pressure plateau at the trailing edge, especially on the pressure surface. The optimum shape resulted from the optimisation task with the WENO5 method is more deflected than the one obtained with the second order method. This practically results in an increase in camber. Inviscid theory assumes that the increase in camber will result in higher lift gains through the Kutta condition. In real viscous flows a separation bubble occurs near the trailing edge that has an adverse effect on lift. The more deflected shape increases the extend of the separation bubble towards the wake which causes the flow to decelerate on both suction and pressure surfaces. As Figure 5.7 shows, the resulting pressure drop on the lower surface is more profound and is what causes the net reduction in lift.

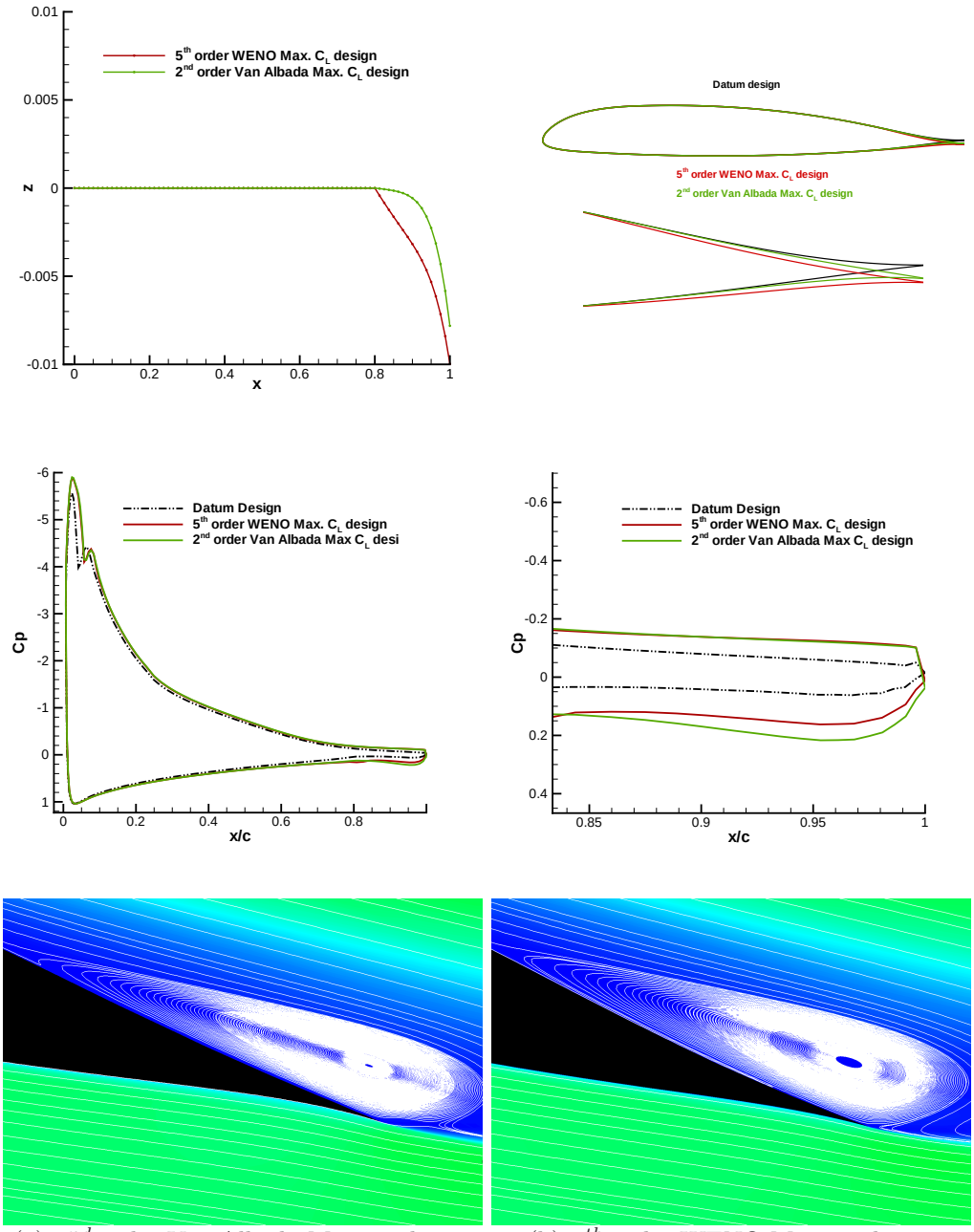

(a) 2^{nd} order Van Albada Max. c_l design (b) 5^{th} order WENO Max. c_l design

Figure 5.7: Comparison of optimum design for maximum lift coefficient between the 2^{nd}order and 5^{th} order method. Polynomial design function (top left) and resulting aerofoil shape (top right), c_p distribution (middle), Mach number contours with superimposed streamlines (bottom).

This observation however does not diminish the importance of high resolution methods. Instead, it highlights the effectiveness of the optimisation algorithm employed, when a large amount of optimisation cycles are performed, at least as far as the less sensitive lift coefficient is concerned. It further illustrates how subtle shape differences can have a significant impact on the local flow physics and hence on aerodynamic performance. In fact the sensitivity of the flow metrics to the geometric perturbations is more profound as the resolution and thus quality and accuracy of the CFD simulation increases.

Depending on the flow metrics of interest the use of low accuracy computational methods can result in undesirable and misleading conclusions. This has been most clearly demonstrated for the case of the very sensitive c_m. On the other hand the objective function regarding the c_l was less sensitive to the accuracy of the numerical method. In fact the higher and lower numerical schemes performed comparably well when it came to satisfying the first objective function. However, to control the introduction of fictitious virtual maxima or minima into the objective function front, it is imperative that the CFD solution is as precise as possible. The correct and accurate integration of the aerodynamic loads is highly dependent on the underlying nominal order of accuracy of the CFD methods.

Optimum Designs resulting from the Second Order Method

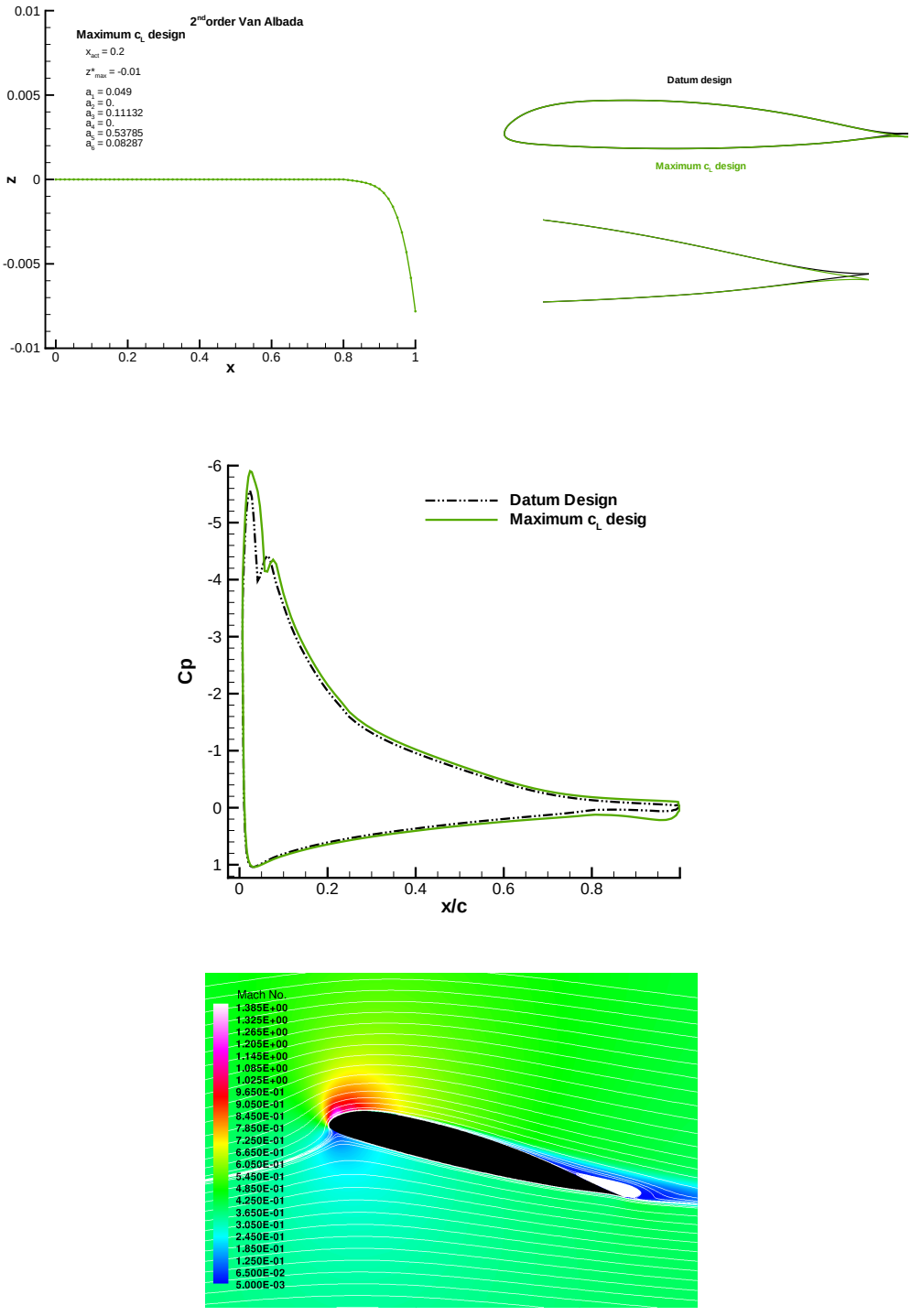

Figure 5.8: Maximum c_l design, resulting from 2^{nd}order VanAlbada scheme. Polynomial design function (top left) and resulting aerofoil shape (top right), c_p distribution (middle), Mach number contours with superimposed streamlines (bottom).

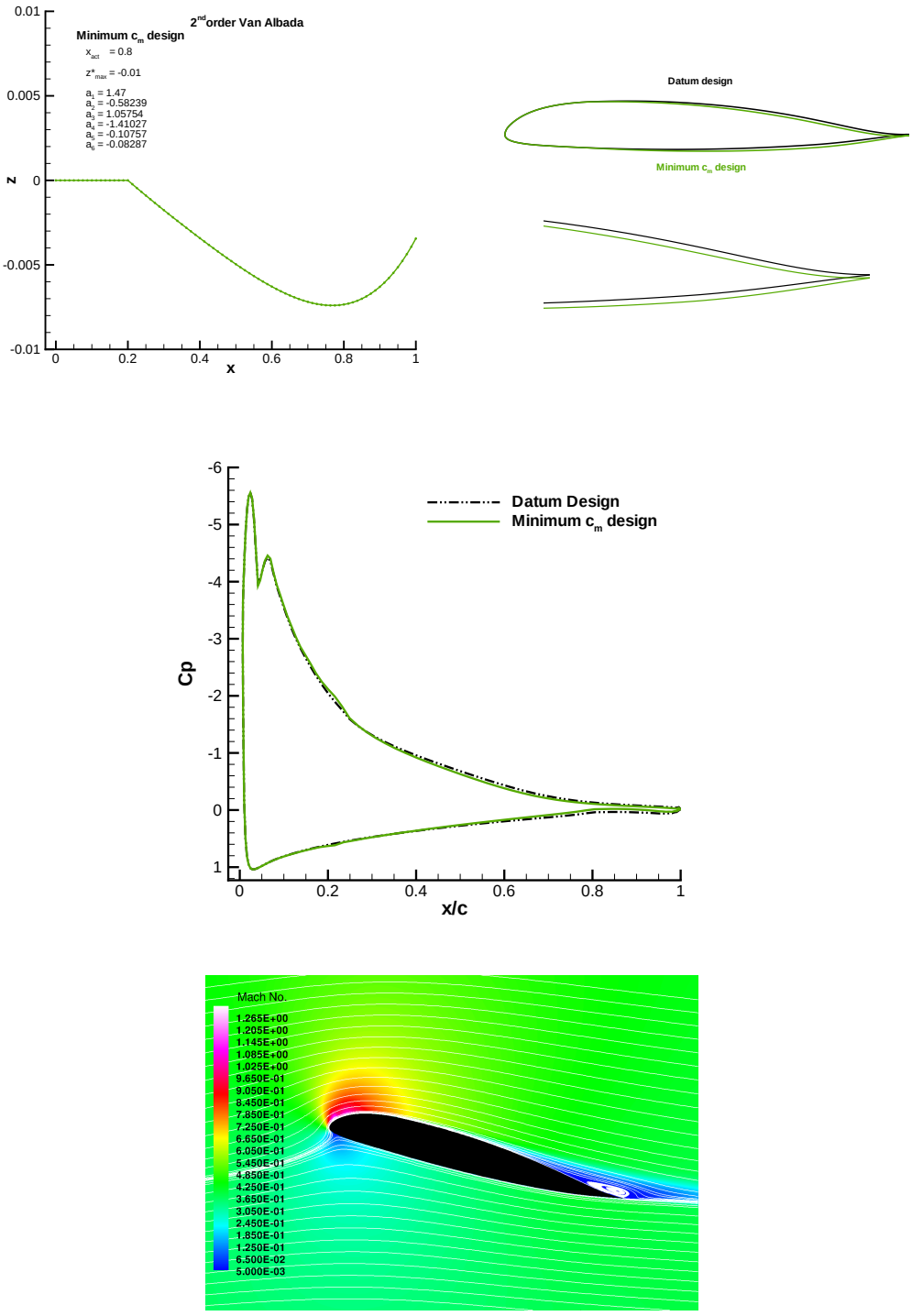

Figure 5.9: Minimum c_m design, resulting from 2^{nd}order VanAlbada scheme. Polynomial design function (top left) and resulting aerofoil shape (top right), c_p distribution (middle), Mach number contours with superimposed streamlines (bottom).

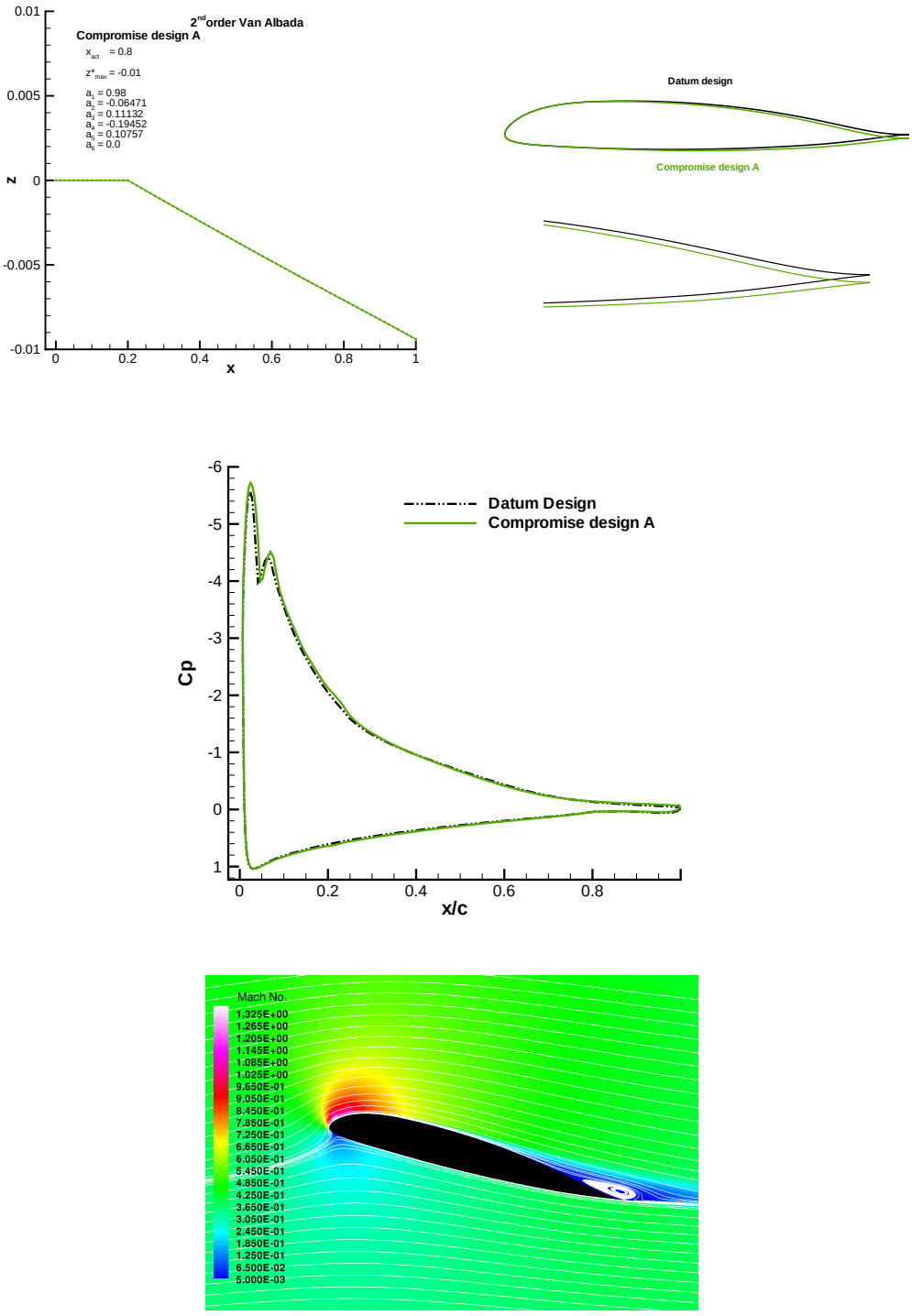

Figure 5.10: Compromise design A, resulting from 2^{nd}order VanAlbada scheme. Polynomial design function (top left) and resulting aerofoil shape (top right), c_p distribution (middle), Mach number contours with superimposed streamlines (bottom).

Optimum Designs resulting from the Third Order Method

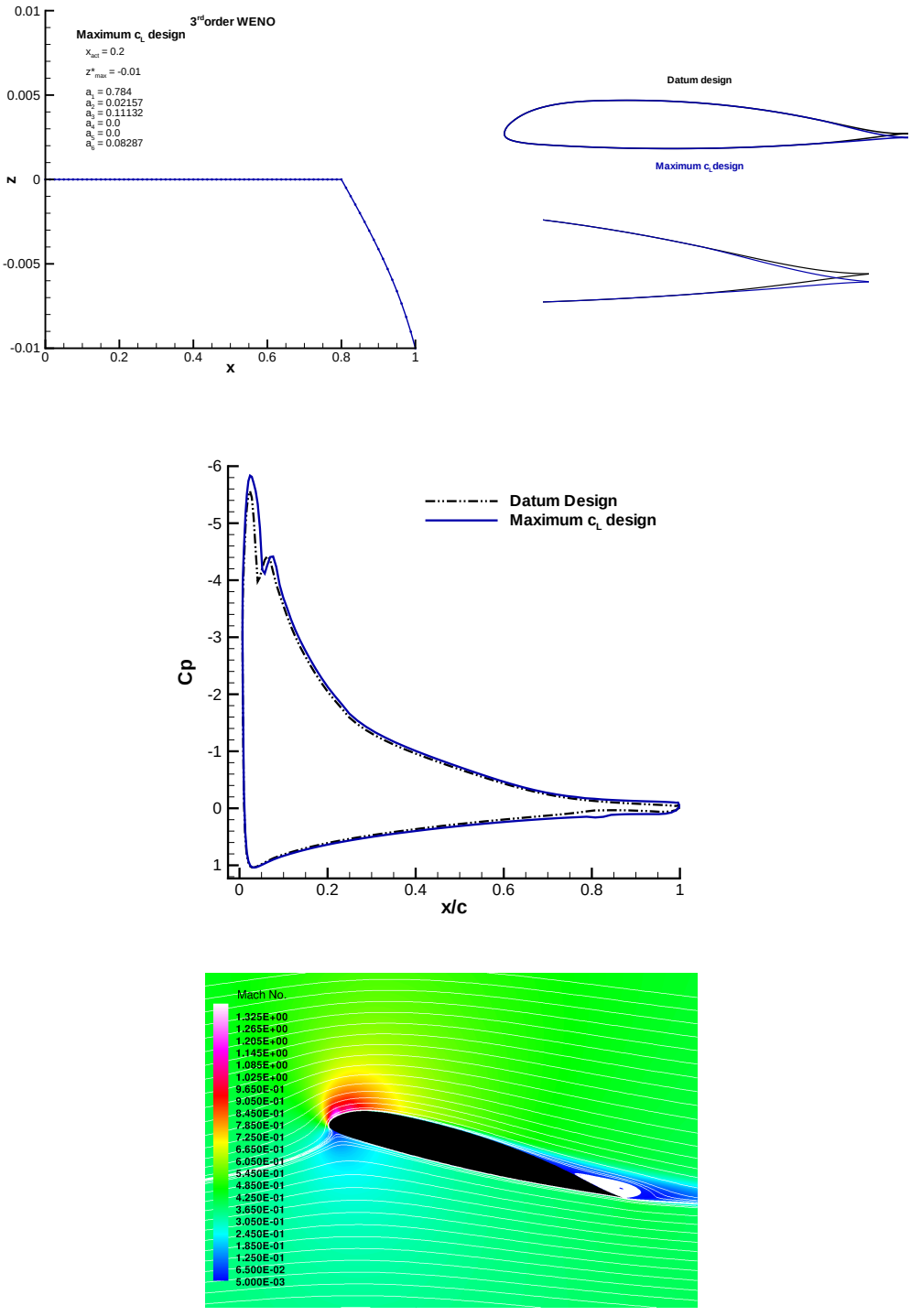

Figure 5.11: Maximum c_l design, resulting from 3^{rd}order WENO scheme. Polynomial design function (top left) and resulting aerofoil shape (top right), c_p distribution (middle), Mach number contours with superimposed streamlines (bottom).

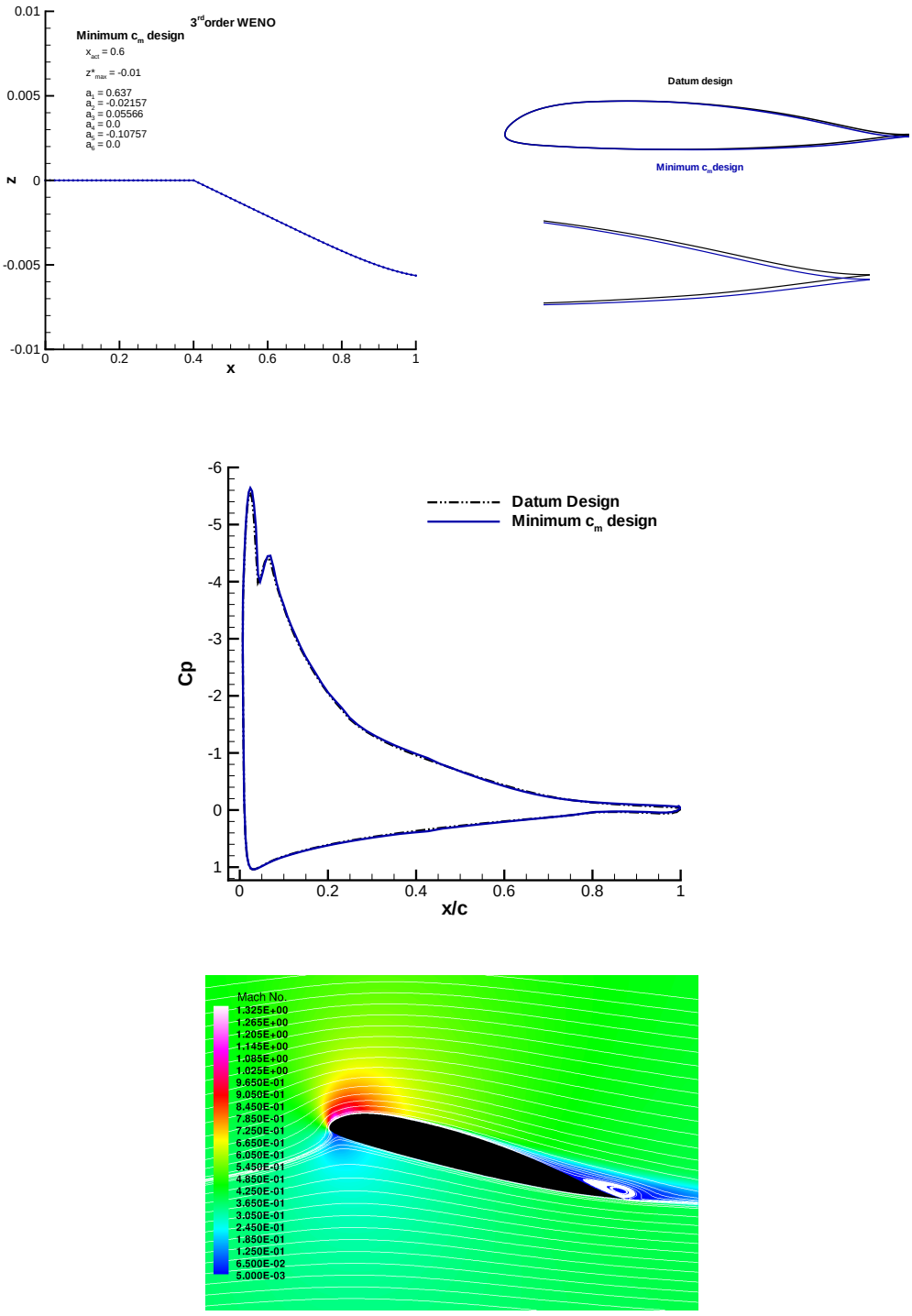

Figure 5.12: Maximum c_m design, resulting from 3^{rd}order WENO scheme. Polynomial design function (top left) and resulting aerofoil shape (top right), c_p distribution (middle), Mach number contours with superimposed streamlines (bottom).

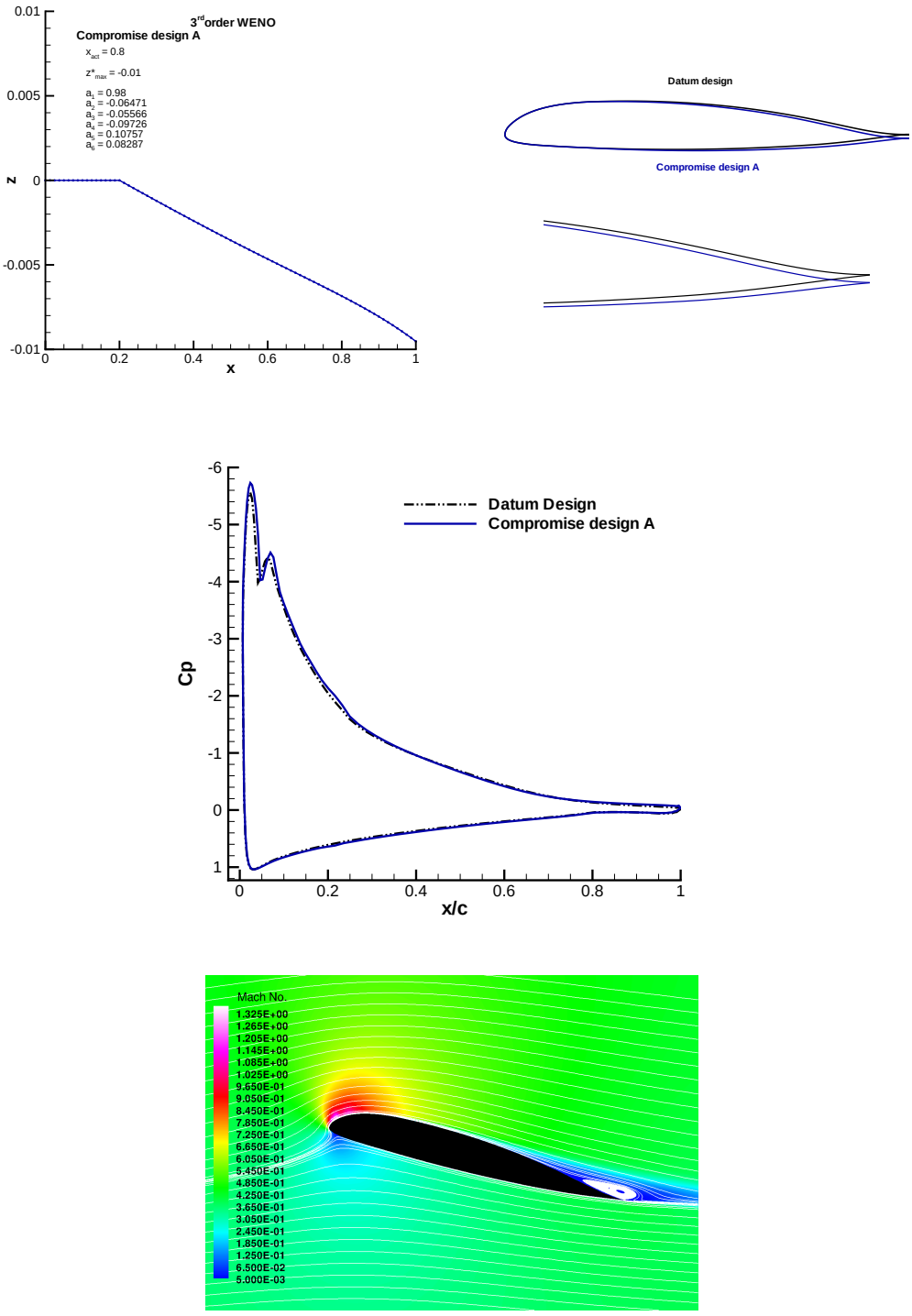

Figure 5.13: Compromise design A, resulting from 3^{rd}order WENO scheme. Polynomial design function (top left) and resulting aerofoil shape (top right), c_p distribution (middle), Mach number contours with superimposed streamlines (bottom).

Optimum Designs resulting from the Fifth Order Method

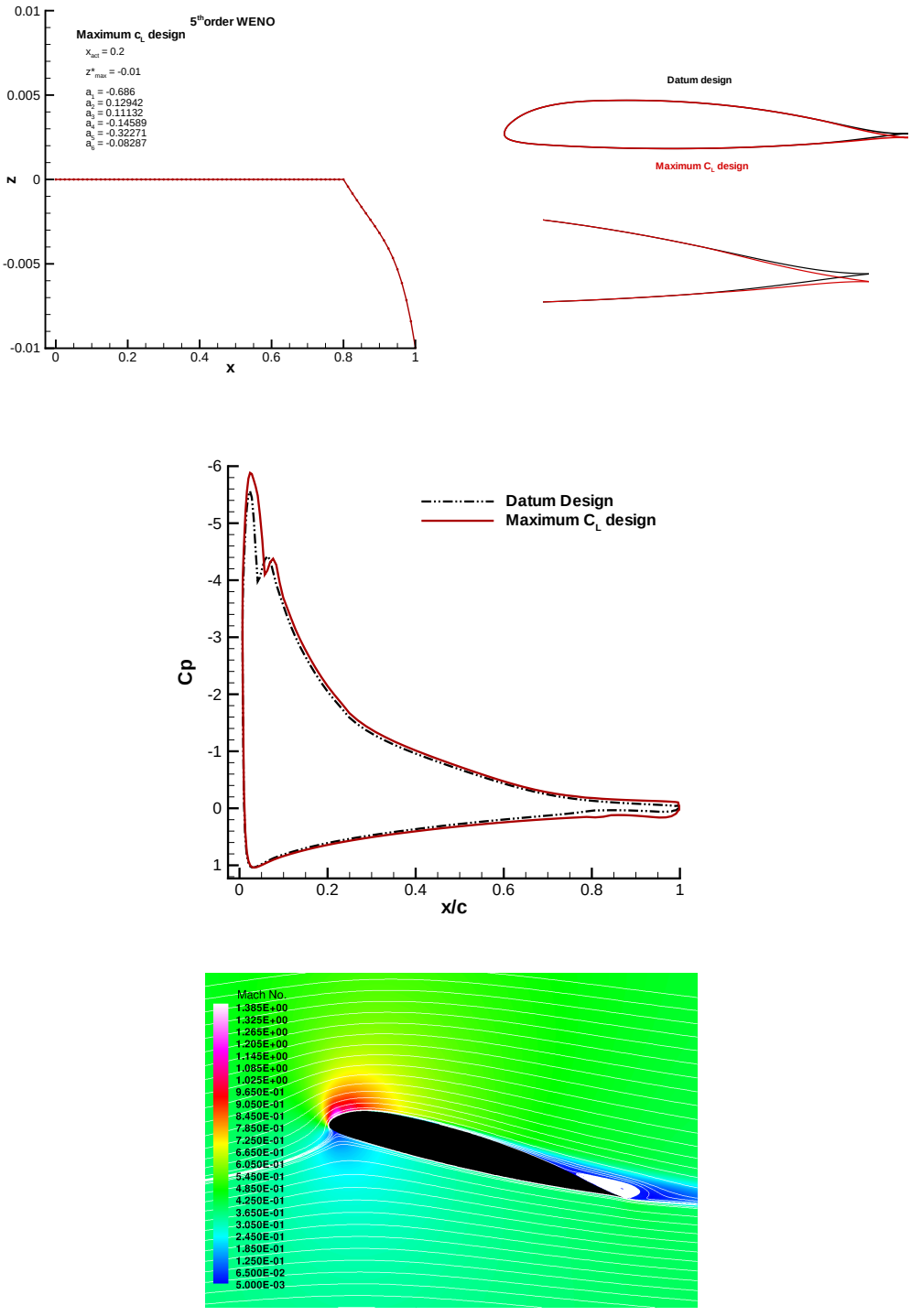

Figure 5.14: Maximum c_l design, resulting from 5^{th}order WENO scheme. Polynomial design function (top left) and resulting aerofoil shape (top right), c_p distribution (middle), Mach number contours with superimposed streamlines (bottom).

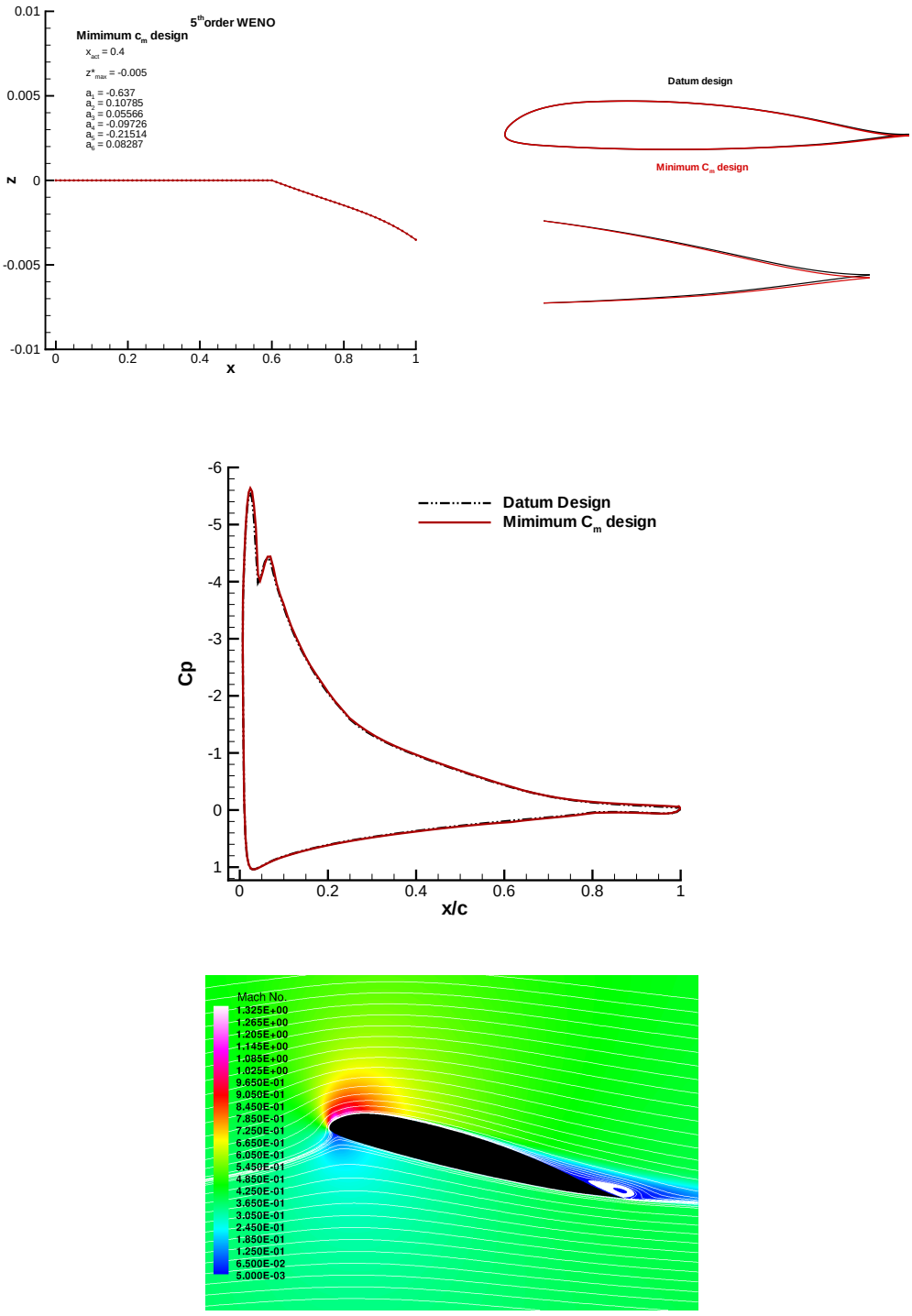

Figure 5.15: Minimum c_m design, resulting from 5^{th}order WENO scheme. Polynomial design function (top left) and resulting aerofoil shape (top right), c_p distribution (middle), Mach number contours with superimposed streamlines(bottom).

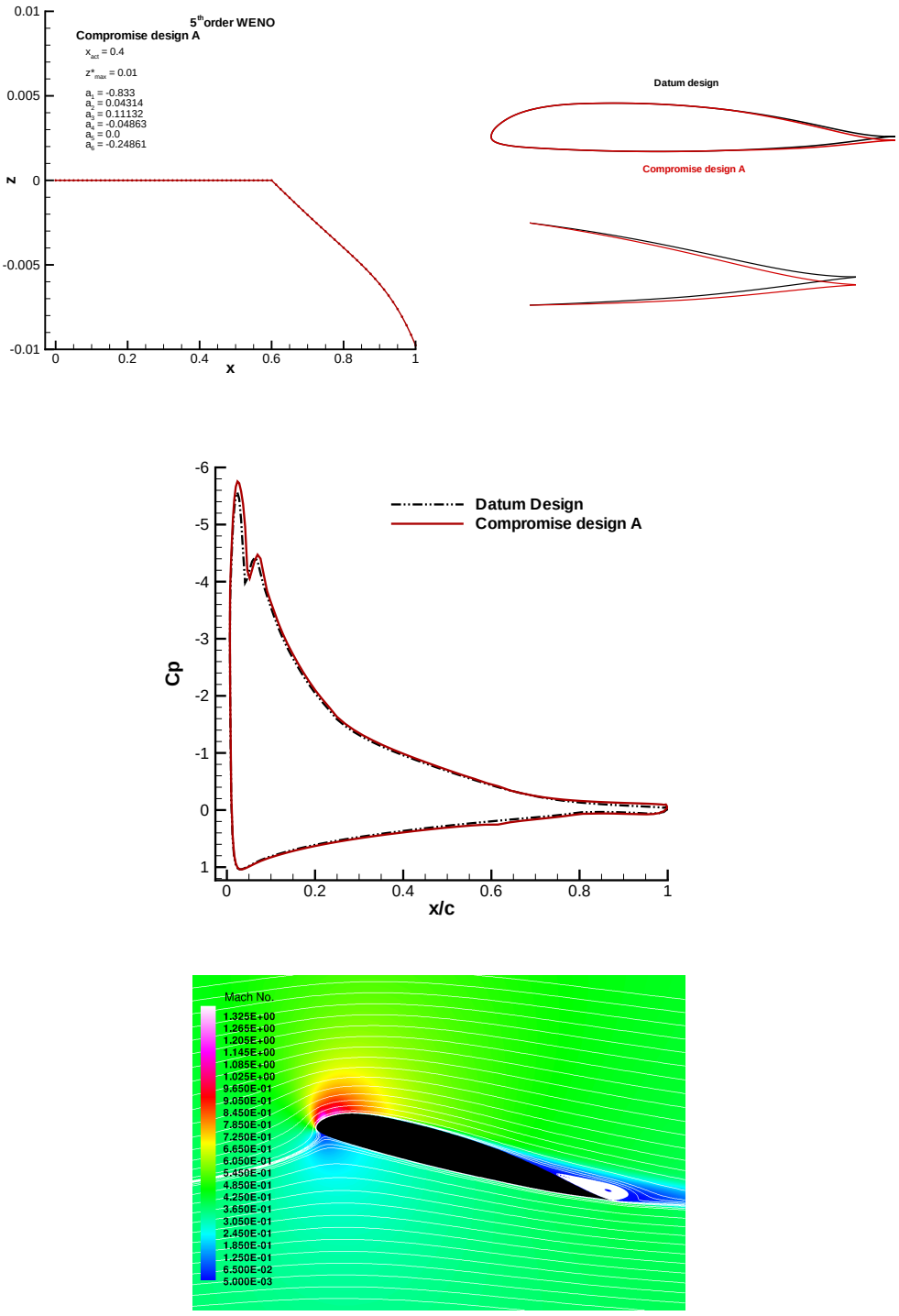

Figure 5.16: Compromise design A, resulting from 5^{th}order WENO CFD scheme. Polynomial design function (top left) and resulting aerofoil shape (top right), c_p distribution (middle), Mach number contours with superimposed streamlines(bottom)

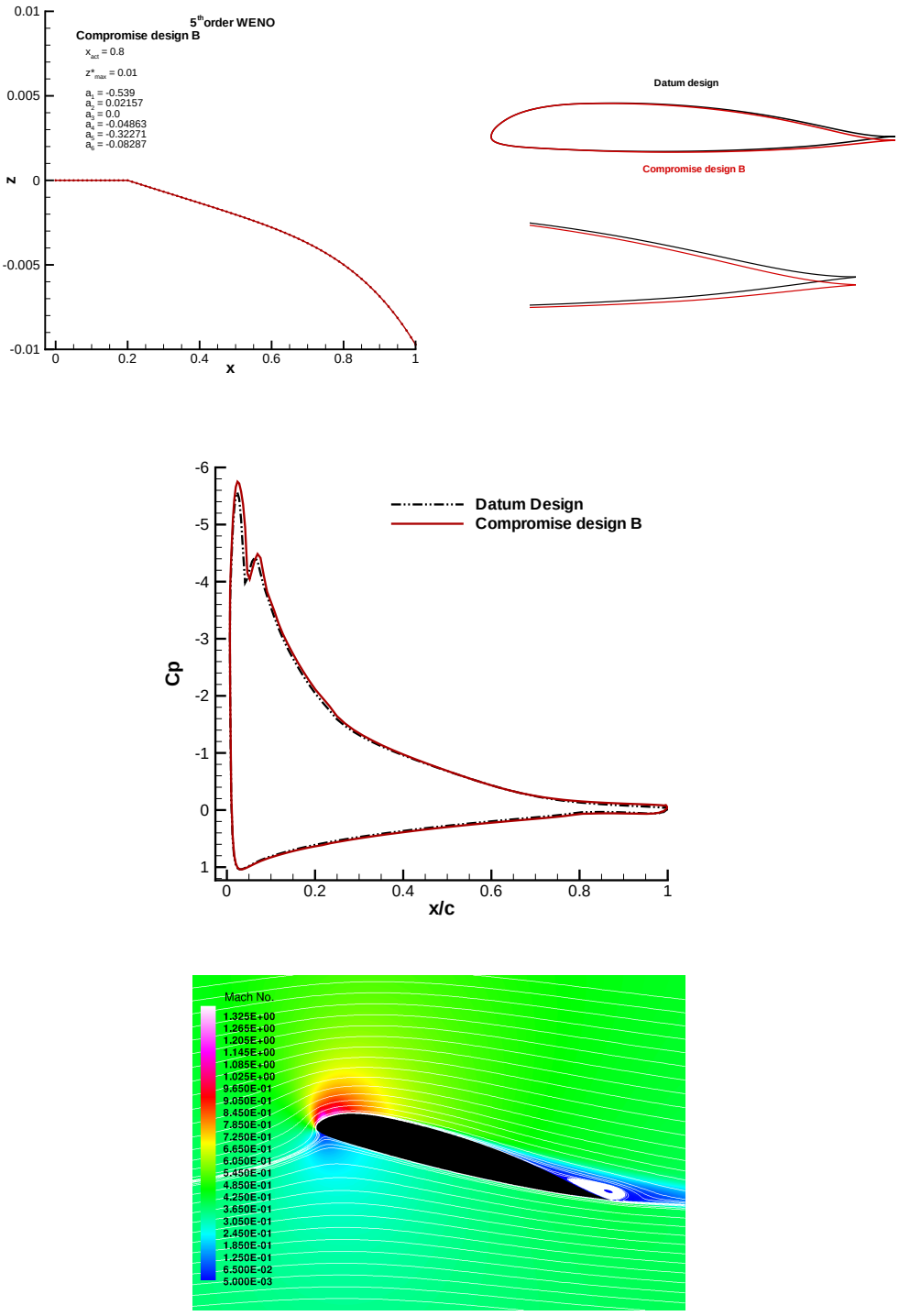

Figure 5.17: Compromise design B, resulting from 5^{th}order WENO scheme. Polynomial design function (top left) and resulting aerofoil shape (top right), c_p distribution (middle), Mach number contours with superimposed streamlines (bottom).

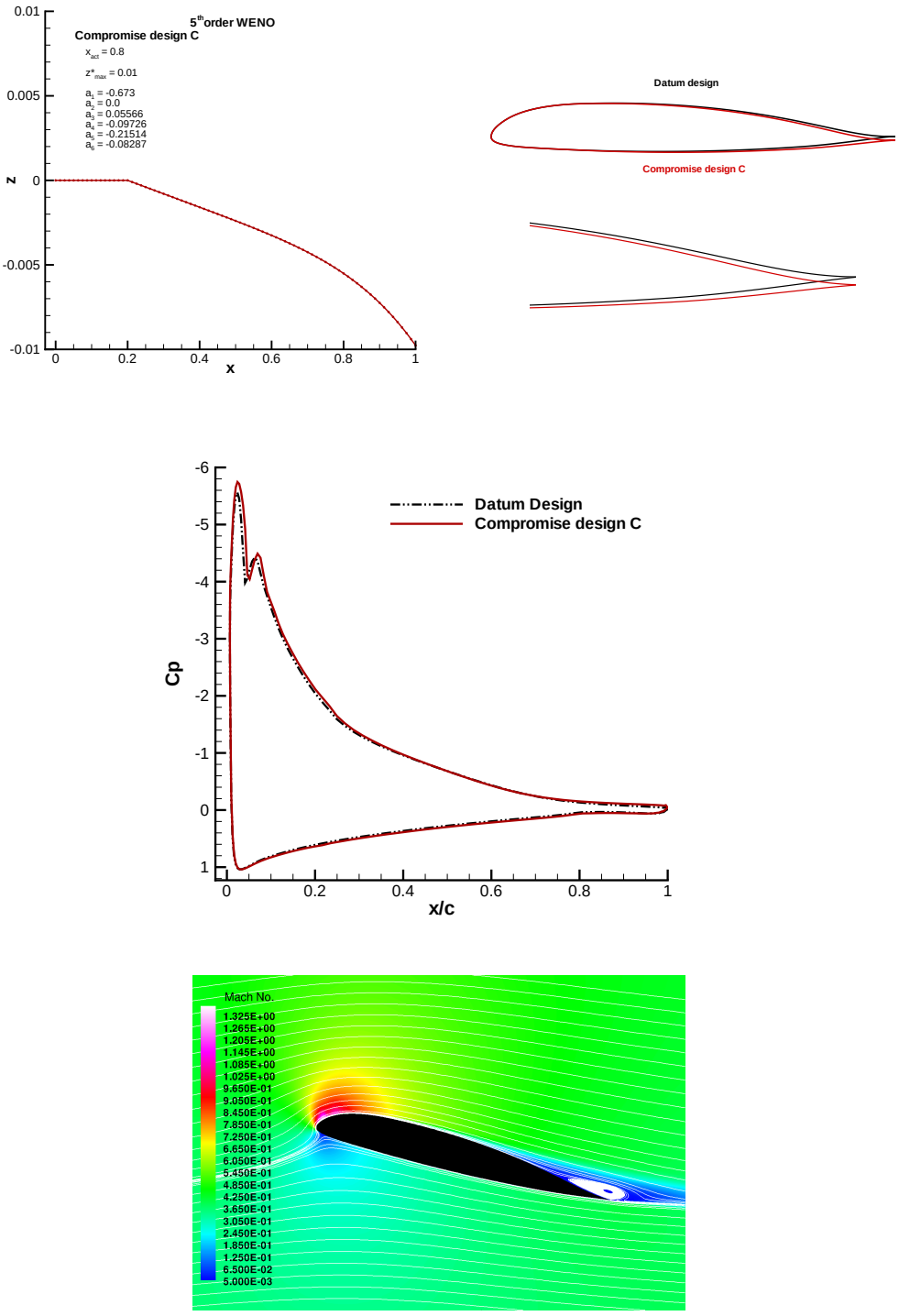

Figure 5.18: Compromise design C, resulting from 5^{th}order WENO scheme. Polynomial design function (top left) and resulting aerofoil shape (top right), c_p distribution (middle), Mach number contours with superimposed streamlines (bottom).

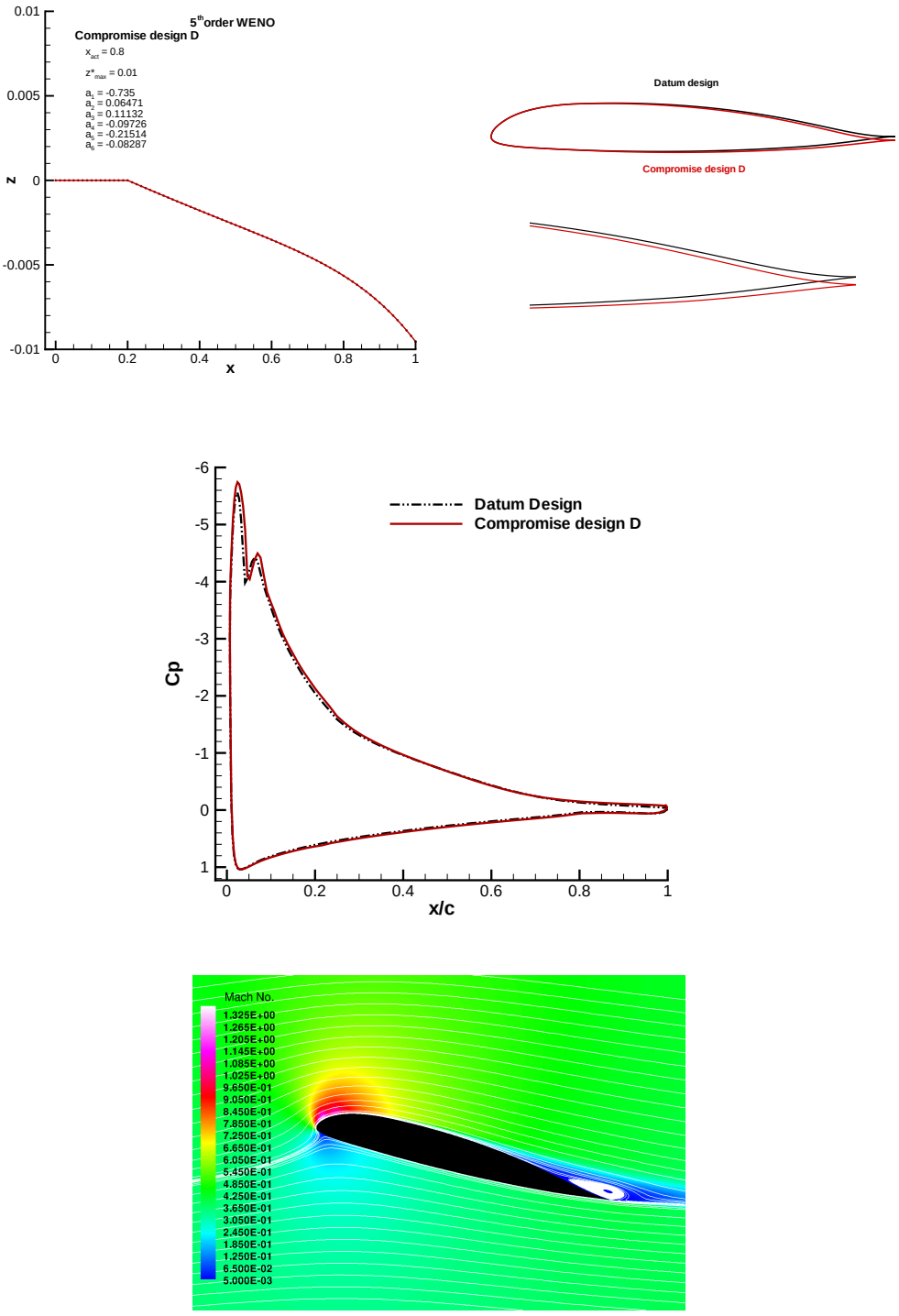

Figure 5.19: Compromise design D, resulting from 5^{th}order WENO scheme. Polynomial design function (top left) and resulting aerofoil shape (top right), c_p distribution (middle), Mach number contours with superimposed streamlines (bottom).

Chapter 6

Conclusions

The results of the foregoing studies demonstrate the importance of high resolution methods for RANS modeling and aerodynamic optimisation. The effect that the increased numerical accuracy has on RANS computation was signified in Chapter 4, where computations were performed for two highly diverse flow regimes and computationally demanding test cases with complex flow phenomena. The transonic flow over the RAE 2822 aerofoil features shock boundary layer interaction and shock induced separation, while the subsonic flow over the NACA 4412 near maximum lift is substantially separated near the trailing edge and a steady separation bubble is formed. For both cases a grid convergence study was performed and it was observed that the 5^{th} order method displayed signs of grid independence. Furthermore, the relative timings of the different numerical schemes on different grids proved that it is much more efficient to employ a high resolution method on a coarser grid than to use a lower order method on a finer computational mesh.

As it was expected the highest order method outperformed all other methods in terms of accuracy. Any observed discrepancies with the experimental data were partially attributed to the assumed linear dependency of the Reynolds stress to the mean strain rate tensor, via the Boussinesq relation. Since each method converged to a different result, it became evident that besides the constitutive relation (Boussinesq), the solution was greatly affected by the discretisation of the convected fluxes. In fact, the increase of the numerical resolution improved significantly the predictions. The aerodynamic loads resulting from the present

work were compared with the aerodynamic loads reported by other authors for the same cases using similar grids, but with lower order methods and more sophisticated non linear eddy viscosity models. The comparison strongly favors and justifies the use of high, 5^{th}, order methods for turbulent flow computations in the context of RANS. The relative comparison strengthens the hypothesis that at least in 2d RANS computations, the effect of high resolution methods is more profound than the turbulence model. This is not to diminish the importance of the eddy viscosity models but to rather highlight the need for high accuracy both in terms of turbulence modeling and numerical methods in engineering analysis and design.

Regarding aerodynamic design optimisation, a Multi-Objective Integrated Design system (MOBID) has been built in order to identify feasible designs of the novel Active Camber, flow control concept. The system encompasses the developed CFD solver with a state of the art heuristic optimisation algorithm, along with an efficient parametrization technique and a fast and robust method of propagating geometric displacements. The methodologies in the MOBID system resulted in the identification of the design vectors that revealed aerodynamic performance gains over the datum aerofoil design. The Pareto front provided a clear picture of the achievable trade-offs between the competing objectives.

For the present investigation a much finer computational mesh was used and a more accurate turbulence model was employed than what is generally the case in aerodynamic optimisation. The same optimisation problem was iterated with the resolution scheme varying. Remarkably, it was found that the results of the search pattern change noticeably with respect to the order of the CFD method. In fact the search pattern resulted from the 2^{nd} order method got trapped in a sub-optimum region, making evident that in order to control the introduction of fictitious optima into the objective function front, it is imperative to employ a high precision CFD solver. The high accuracy CFD method resulted in optimised shapes that outperformed significantly the datum design. Whereas, the lower order methods failed to satisfy the more sensitive objective regarding c_m.

However, the search patterns of the 3^{rd} and 5^{th}order optimisation variants, displayed similar characteristics. The 3^{rd}order variant managed to capture the design space morphology compared to 5^{th} order Pareto front, thus one could

suggest to use the lower order, and thus faster, CFD method for optimisation algorithm development and adaptation to complex engineering design problems, and more specifically to aerodynamics. Nevertheless, when it comes to the actual optimisation process there is no choice but to employ the highest resolution available in order not to compromise the accuracy of the evaluation.

6.1 Future Work

The efficacy of high resolution methods points towards a new direction regarding turbulence modeling for large scale engineering applications. In the present study it became apparent that by increasing the nominal order of accuracy of the scheme, more of the flow physics are resolved than modeled and thus some of the shortcomings of the turbulence modeling assumption are somewhat alleviated. Nevertheless, the inability of the models to predict transition results in a globally present eddy viscosity that results in excessive damping of fluctuations, loss of information and effectively pollutes the solution. There is a clear need to extract large-scale features at minimal computational expense and for real life-applications. This is the main drive of emerging computational methods that combine the cost-effectiveness of RANS with the accuracy of LES, such as detached-eddy simulations (DES) [116], and hybrid RANS/LES

Quite recently Girimaji [117], presented a method of intermediate cost/accuracy ratio, the Partially-Averaged Navier Stokes (PANS). The intriguing idea of PANS is that by defining filter-type "unresolved-to-total" ratios of kinetic energy (f_k)and dissipation (f_ϵ) the method ranges from RANS to DNS. The filters delimiting resolved and modeled motion are implied rather than explicitly defined, while the parameters f_k and f_ϵ can be constant or vary as a function of time and space (in the spirit of DES). Such concepts, make the PANS method a promising way towards robust CFD solvers that can be either used for DNS studies or as part of an engineering design system.

In order to improve the newly developed multi-objective integrated design system a restart strategy is suggested for implementation. The Epanechnikov function [118] can be used as a statistical quantity, measuring the density of

visited designs. The search pattern should be directed towards the least investigated region, according to the relative densities of the design area. The step size of the design variables should be also adapted according to the respective density. Large step sizes should be assigned for low percentage density and small for high percentage density. This way a broader design space can be explored in a more efficient manner, while the possibility of a sub-optimum region lock will be alleviated.

Appendix A

Transformation of Viscous Fluxes to Generalized Curvilinear Coordinates

The viscous fluxes can be written explicitely as;

- In ξ- direction;

$$R = \begin{bmatrix} 0 \\ \tau_{xx}\hat{\xi_x} + \tau_{zx}\hat{\xi_z} \\ \tau_{xz}\hat{\xi_x} + \tau_{zz}\hat{\xi_z} \\ u\tau_{xx}\hat{\xi_x} + w\tau_{xz}\hat{\xi_x} - q_x\hat{\xi_x} + u\tau_{zx}\hat{\xi_z} + w\tau_{zz}\hat{\xi_z} - q_z\hat{\xi_z} \\ \frac{1}{Re}\left(\mu + \sigma_\kappa\mu_t\right)\left(\frac{\partial k}{\partial x}\hat{\xi_x} + \frac{\partial k}{\partial z}\hat{\xi_z}\right) \\ \frac{1}{Re}\left(\mu + \sigma_\omega\mu_t\right)\left(\frac{\partial \omega}{\partial x}\hat{\xi_x} + \frac{\partial \omega}{\partial z}\hat{\xi_z}\right) \end{bmatrix}$$

where also the stresses and the heat transfer are transformed to generalized coordinates such that;

$$\tau_{xx} = \frac{4}{3}\frac{1}{Re}\left(\mu + \mu_t\right)\left(\frac{\partial u}{\partial x}\right) - \frac{2}{3}\frac{1}{Re}\left(\mu + \mu_t\right)\left(\frac{\partial w}{\partial z}\right) - \frac{2}{3}\rho\kappa$$

remembering that $\hat{\xi_x} = J\xi_x$, $\hat{\xi_z} = J\xi_z$, then

$$\tau_{xx} = \frac{1}{J}\frac{1}{Re}\left[\frac{4}{3}\left(\mu + \mu_t\right)\left(\frac{\partial u}{\partial \xi}\hat{\xi_x} + \frac{\partial u}{\partial \zeta}\hat{\zeta_x}\right) - \frac{2}{3}\left(\mu + \mu_t\right)\left(\frac{\partial w}{\partial \xi}\hat{\xi_z} + \frac{\partial w}{\partial \zeta}\hat{\zeta_z}\right)\right]$$

Similarly;

$$\tau_{zz} = \frac{1}{J}\frac{1}{Re}\left[\frac{4}{3}\left(\mu+\mu_t\right)\left(\frac{\partial w}{\partial \xi}\hat{\xi}_z+\frac{\partial w}{\partial \zeta}\hat{\zeta}_z\right)-\frac{2}{3}\left(\mu+\mu_t\right)\left(\frac{\partial u}{\partial \xi}\hat{\xi}_x+\frac{\partial u}{\partial \zeta}\hat{\zeta}_x\right)\right]$$

and

$$\tau_{xz}=\tau_{zx} = \frac{1}{J}\frac{1}{Re}\left(\mu+\mu_t\right)\left[\left(\frac{\partial u}{\partial \xi}\hat{\xi}_z+\frac{\partial u}{\partial \zeta}\hat{\zeta}_z\right)+\left(\frac{\partial w}{\partial \xi}\hat{\xi}_x+\frac{\partial w}{\partial \zeta}\hat{\zeta}_x\right)\right]$$

The non-dimensional heat fluxes read;

$$q_x = -\frac{1}{J}\frac{1}{Re}\left(\mu\frac{\gamma}{Pr}+\mu_t\frac{\gamma}{Pr_\tau}\right)\left(\frac{\partial T}{\partial \xi}\hat{\xi}_x+\frac{\partial T}{\partial \zeta}\hat{\zeta}_x\right)$$

and

$$q_z = -\frac{1}{J}\left(VIST_L\frac{\gamma}{Pr}+\mu_t\frac{\gamma}{Pr_\tau}\right)\left(\frac{\partial T}{\partial \xi}\hat{\xi}_z+\frac{\partial T}{\partial \zeta}\hat{\zeta}_z\right)$$

while the turbulent viscous terms;

$$\begin{aligned}\frac{\partial k}{\partial x} &= \left(\frac{\partial k}{\partial \xi}\xi_x+\frac{\partial k}{\partial \zeta}\zeta_x\right)\\ &= \frac{1}{J}\left(\frac{\partial k}{\partial \xi}\hat{\xi}_x+\frac{\partial k}{\partial \zeta}\hat{\zeta}_x\right),\end{aligned}$$

$$\begin{aligned}\frac{\partial k}{\partial z} &= \left(\frac{\partial k}{\partial \xi}\xi_z+\frac{\partial k}{\partial \zeta}\zeta_z\right)\\ &= \frac{1}{J}\left(\frac{\partial k}{\partial \xi}\hat{\xi}_z+\frac{\partial k}{\partial \zeta}\hat{\zeta}_z\right)\end{aligned}$$

and

$$\begin{aligned}\frac{\partial \omega}{\partial x} &= \left(\frac{\partial \omega}{\partial \xi}\xi_x+\frac{\partial \omega}{\partial \zeta}\zeta_x\right)\\ &= \frac{1}{J}\left(\frac{\partial \omega}{\partial \xi}\hat{\xi}_x+\frac{\partial \omega}{\partial \zeta}\hat{\zeta}_x\right),\end{aligned}$$

$$\begin{aligned}\frac{\partial \omega}{\partial z} &= \left(\frac{\partial \omega}{\partial \xi}\xi_z+\frac{\partial \omega}{\partial \zeta}\zeta_z\right)\\ &= \frac{1}{J}\left(\frac{\partial \omega}{\partial \xi}\hat{\xi}_z+\frac{\partial \omega}{\partial \zeta}\hat{\zeta}_z\right)\end{aligned}$$

Appendix B

Inviscid Jacobians

The conservative Flux Jacobians in generalized time dependent curvilinear coordinates can be written as:

$$A_{inv} = \begin{bmatrix} 0 & \hat{\xi_x} & \hat{\xi_z} \\ (\gamma-1)\left(\frac{q^2}{2}\right)\hat{\xi_x} - uq_\xi & q_\xi - (\gamma-2)\,u\hat{\xi_x} & u\hat{\xi_z} - (\gamma-1)\,w\hat{\xi_x} \\ (\gamma-1)\left(\frac{q^2}{2}\right)\hat{\xi_z} - wq_\xi & w\hat{\xi_x} - (\gamma-1)\,u\hat{\xi_z} & q_\xi - (\gamma-2)\,w\hat{\xi_z} \\ \left[(\gamma-1)\left(\frac{q^2}{2}\right) - H\right]q_\xi & H\hat{\xi_x} - (\gamma-1)\,uq_\xi & H\hat{\xi_z} - (\gamma-1)\,wq_\xi \\ -kq_\xi & k\hat{\xi_x} & k\hat{\xi_z} \\ -\omega q_\xi & \omega\hat{\xi_x} & \omega\hat{\xi_z} \end{bmatrix}$$

$$\begin{bmatrix} 0 & 0 & 0 \\ (\gamma-1)\,\hat{\xi_x} & -\mathbf{C}\,(\gamma-1)\,\hat{\xi_x} & 0 \\ (\gamma-1)\,\hat{\xi_z} & -\mathbf{C}\,(\gamma-1)\,\hat{\xi_z} & 0 \\ \gamma q_\xi & -\mathbf{C}\,(\gamma-1)\,\overrightarrow{U} & 0 \\ 0 & q_\xi & 0 \\ 0 & 0 & q_\xi \end{bmatrix}$$

and

$$
C_{inv} = \begin{bmatrix}
0 & \hat{\zeta_x} & \hat{\zeta_z} \\
(\gamma-1)\left(\frac{q^2}{2}\right)\hat{\zeta_x} - uq_\zeta & q_\zeta - (\gamma-2)\,u\hat{\zeta_x} & u\hat{\zeta_z} - (\gamma-1)\,w\hat{\xi_x} \\
(\gamma-1)\left(\frac{q^2}{2}\right)\hat{\zeta_z} - wq_\zeta & w\hat{\zeta_x} - (\gamma-1)\,u\hat{\zeta_z} & q_\zeta - (\gamma-2)\,w\hat{\xi_z} \\
\left[(\gamma-1)\left(\frac{q^2}{2}\right) - H\right]\overrightarrow{q_\zeta} & H\hat{\zeta_x} - (\gamma-1)\,uq_\zeta & H\hat{\zeta_z} - (\gamma-1)\,wq_\zeta \\
-kq_\zeta & k\hat{\zeta_x} & k\hat{\zeta_z} \\
-\omega q_\zeta & \omega\hat{\zeta_x} & \omega\hat{\zeta_z}
\end{bmatrix}
\begin{bmatrix}
0 & 0 & 0 \\
(\gamma-1)\,\hat{\zeta_x} & -\mathbf{C}\,(\gamma-1)\,\hat{\zeta_x} & 0 \\
(\gamma-1)\,\hat{\zeta_z} & -\mathbf{C}\,(\gamma-1)\,\hat{\zeta_z} & 0 \\
\gamma q_\zeta & -\mathbf{C}\,(\gamma-1)\,q_\zeta & 0 \\
0 & q_\zeta & 0 \\
0 & 0 & q_\zeta
\end{bmatrix}
$$

Appendix C

Diagonalization of the Jacobian matrices and compatibility relations

Since there are few zero elements in Jacobians $A,\ C$ it is difficult to determine their eigenvalues-eigenvectors necessary for the intended splitting. Hence it is more convenient to consider the non-conservative form of inviscid equations in curvilinear co-ordinates. Upon definition of the non conservative solution vector;

$$\upsilon = [\rho, u, w, p_t, k, \omega]^T$$

and

$$M = \frac{\partial \mathbf{U}}{\partial \upsilon} = \begin{bmatrix} 1 & 0 & 0 & 0 & 0 & 0 \\ u & \rho & 0 & 0 & 0 & 0 \\ w & 0 & \rho & 0 & 0 & 0 \\ \frac{q^2}{2} + \mathbf{C}k & \rho u & \rho w & \frac{1}{\gamma - 1} & \mathbf{C}\rho & 0 \\ k & 0 & 0 & 0 & \rho & 0 \\ \omega & 0 & 0 & 0 & 0 & \rho \end{bmatrix}$$

$$M^{-1} = \frac{\partial v}{\partial \mathbf{U}} = \begin{bmatrix} 1 & 0 & 0 & 0 & 0 & 0 \\ -\frac{u}{\rho} & \frac{1}{\rho} & 0 & 0 & 0 & 0 \\ -\frac{w}{\rho} & 0 & \frac{1}{\rho} & 0 & 0 & 0 \\ (\gamma-1)\frac{q^2}{2} & -(\gamma-1)u & -(\gamma-1)w & \gamma-1 & -\mathbf{C}(\gamma-1) & 0 \\ -\frac{k}{\rho} & 0 & 0 & 0 & \frac{1}{\rho} & 0 \\ -\frac{\omega}{\rho} & 0 & 0 & 0 & 0 & \frac{1}{\rho} \end{bmatrix}$$

the non-concervative convective Flux Jacobians are defined as;

$$a_{inv} = M^{-1} A_{inv} M,\ c_{inv} = M^{-1} C_{inv} M$$

therefore the matrices a_{inv}, c_{inv} are (given that the speed of sound $c^2 = \frac{\gamma p_t}{\rho}$);

$$a_{inv} = \begin{bmatrix} q_\xi & \rho\hat{\xi_x} & \rho\hat{\xi_z} & 0 & 0 & 0 \\ 0 & q_\xi & 0 & \frac{\hat{\xi_x}}{\rho} & 0 & 0 \\ 0 & 0 & q_\xi & \frac{\hat{\xi_z}}{\rho} & 0 & 0 \\ 0 & \rho c^2\hat{\xi_x} & \rho c^2\hat{\xi_x} & q_\xi & 0 & 0 \\ 0 & 0 & 0 & 0 & q_\xi & 0 \\ 0 & 0 & 0 & 0 & 0 & q_\xi \end{bmatrix},$$

$$c_{inv} = \begin{bmatrix} q_\zeta & \rho\hat{\zeta_x} & \rho\hat{\zeta_z} & 0 & 0 & 0 \\ 0 & q_\zeta & 0 & \frac{\hat{\zeta_x}}{\rho} & 0 & 0 \\ 0 & 0 & q_\zeta & \frac{\hat{\zeta_z}}{\rho} & 0 & 0 \\ 0 & \rho c^2\hat{\zeta_x} & \rho c^2\hat{\zeta_x} & q_\zeta & 0 & 0 \\ 0 & 0 & 0 & 0 & q_\zeta & 0 \\ 0 & 0 & 0 & 0 & 0 & q_\zeta \end{bmatrix}$$

Because of their relative simplicity, the eigensystem of the non-conservative equations will be derived first and the these will be transformed to the conservative form using compatibility relations.

The eigenvalues of $a_{inv}$are given by;

$$det\,|a_{inv} - \Lambda| = 0$$

with $\Lambda = \lambda I$

from which, one can find that;

$$\lambda_0 = \lambda_1 = \lambda_2 = \lambda_5 = \lambda_6 = q_\xi$$
$$\lambda_3 = \lambda_0 + c\sqrt{\hat{\xi}_x^2 + \hat{\xi}_z^2}$$
$$\lambda_4 = \lambda_0 - c\sqrt{\hat{\xi}_x^2 + \hat{\xi}_z^2}$$

Although matrix a_{inv} has an eigenvalue of multiplicity four, it has a complete set of linearly independent eigenvectors and can be defined up to arbitrary normalization factors. Consequently the matrix P is constructed using these eigenvectors as columns (right eigenvector)[Beam Warming], by solving ;

$$a_{inv}P = \Lambda P$$

$$P = \begin{bmatrix} 0 & \frac{1}{c^2} & \frac{1}{2c^2} & \frac{1}{2c^2} & 0 & 0 \\ -\frac{\hat{\xi_z}}{\sqrt{\hat{\xi_x^2}+\hat{\xi_z^2}}} & 0 & \frac{\hat{\xi_x}}{2\rho c\sqrt{\hat{\xi_x^2}+\hat{\xi_z^2}}} & -\frac{\hat{\xi_x}}{2\rho c\sqrt{\hat{\xi_x^2}+\hat{\xi_z^2}}} & 0 & 0 \\ \frac{\hat{\xi_x}}{\sqrt{\hat{\xi_x^2}+\hat{\xi_z^2}}} & 0 & \frac{\hat{\xi_z}}{2\rho c\sqrt{\hat{\xi_x^2}+\hat{\xi_z^2}}} & -\frac{\hat{\xi_z}}{2\rho c\sqrt{\hat{\xi_x^2}+\hat{\xi_z^2}}} & 0 & 0 \\ 0 & 0 & \frac{1}{2} & \frac{1}{2} & 0 & 0 \\ 0 & 0 & 0 & 0 & 1 & 0 \\ 0 & 0 & 0 & 0 & 0 & 1 \end{bmatrix}$$

and the left eigenvectors of matrix of a_{inv} is;

$$P^{-1} = \begin{bmatrix} 0 & -\frac{\hat{\xi_z}}{\sqrt{\hat{\xi_x^2}+\hat{\xi_z^2}}} & \frac{\hat{\xi_x}}{\sqrt{\hat{\xi_x^2}+\hat{\xi_z^2}}} & 0 & 0 & 0 \\ c^2 & 0 & 0 & -1 & 0 & 0 \\ 0 & \frac{\rho c\hat{\xi_x}}{\sqrt{\hat{\xi_x^2}+\hat{\xi_z^2}}} & \frac{\rho c\hat{\xi_z}}{\sqrt{\hat{\xi_x^2}+\hat{\xi_z^2}}} & 1 & 0 & 0 \\ 0 & -\frac{\rho c\hat{\xi_x}}{\sqrt{\hat{\xi_x^2}+\hat{\xi_z^2}}} & -\frac{\rho c\hat{\xi_z}}{\sqrt{\hat{\xi_x^2}+\hat{\xi_z^2}}} & 1 & 0 & 0 \\ 0 & 0 & 0 & 0 & 1 & 0 \\ 0 & 0 & 0 & 0 & 0 & 1 \end{bmatrix}$$

Therefore matrix a_{inv} can be rewritten as;

$$a = P\Lambda P^{-1} = M^{-1}AM$$

$$A = MP\Lambda P^{-1}M^{-1}$$

or if one defines the conservative left/righ eigenvectors as$T = MP$and $T^{-1} = P^{-1}M^{-1}$

then:

$$A = T\Lambda T^{-1}$$

where T and T^{-1} are:

$$T = \begin{bmatrix} 0 & \frac{1}{c^2} & \frac{1}{2c^2} & \frac{1}{2c^2} & 0 & 0 \\ -\frac{\rho\hat{\xi_z}}{\sqrt{\hat{\xi_x^2}+\hat{\xi_z^2}}} & \frac{u}{c^2} & \frac{u}{2c^2}+\frac{\hat{\xi_x}}{2c\sqrt{\hat{\xi_x^2}+\hat{\xi_z^2}}} & \frac{u}{2c^2}-\frac{\hat{\xi_x}}{2c\sqrt{\hat{\xi_x^2}+\hat{\xi_z^2}}} & 0 & 0 \\ \frac{\rho\hat{\xi_x}}{\sqrt{\hat{\xi_x^2}+\hat{\xi_z^2}}} & \frac{w}{c^2} & \frac{w}{2c^2}+\frac{\hat{\xi_z}}{2c\sqrt{\hat{\xi_x^2}+\hat{\xi_z^2}}} & \frac{w}{2c^2}-\frac{\hat{\xi_z}}{2c\sqrt{\hat{\xi_x^2}+\hat{\xi_z^2}}} & 0 & 0 \\ \frac{\rho\left(w\hat{\xi_x}-u\hat{\xi_z}\right)}{\sqrt{\hat{\xi_x^2}+\hat{\xi_z^2}}} & \frac{\mathbf{C}k+\frac{1}{2}q^2}{c^2} & \frac{\mathbf{C}k+\frac{1}{2}q^2}{2c^2}+\frac{1}{2(\gamma-1)}+\frac{\left(u\hat{\xi_x}+w\hat{\xi_z}\right)}{2c\sqrt{\hat{\xi_x^2}+\hat{\xi_z^2}}} & \frac{\mathbf{C}k+\frac{q^2}{2}}{2c^2}+\frac{1}{2(\gamma-1)}-\frac{\left(u\hat{\xi_x}+w\hat{\xi_z}\right)}{2c\sqrt{\hat{\xi_x^2}+\hat{\xi_z^2}}} & \mathbf{C}\rho & 0 \\ 0 & \frac{k}{c^2} & \frac{k}{2c^2} & \frac{k}{2c^2} & \rho & 0 \\ 0 & \frac{\omega}{c^2} & \frac{\omega}{2c^2} & \frac{\omega}{2c^2} & 0 & \rho \end{bmatrix}$$

and

$$T^{-1} = \begin{bmatrix} \frac{u\hat{\xi_z}-w\hat{\xi_x}}{\rho\sqrt{\hat{\xi_x^2}+\hat{\xi_z^2}}} & -\frac{\hat{\xi_z}}{\rho\sqrt{\hat{\xi_x^2}+\hat{\xi_z^2}}} & \frac{\hat{\xi_x}}{\rho\sqrt{\hat{\xi_x^2}+\hat{\xi_z^2}}} & 0 & 0 & 0 \\ c^2-\frac{1}{2}q^2(\gamma-1) & (\gamma-1)u & (\gamma-1)w & -(\gamma-1) & \mathbf{C}(\gamma-1) & 0 \\ \frac{q^2(\gamma-1)}{2}-\frac{c\left(u\hat{\xi_x}+w\hat{\xi_z}\right)}{\sqrt{\hat{\xi_x^2}+\hat{\xi_z^2}}} & -\left[(\gamma-1)u-\frac{c\hat{\xi_x}}{\sqrt{\hat{\xi_x^2}+\hat{\xi_z^2}}}\right] & -\left[(\gamma-1)w-\frac{c\hat{\xi_z}}{\sqrt{\hat{\xi_x^2}+\hat{\xi_z^2}}}\right] & (\gamma-1) & -\mathbf{C}(\gamma-1) & 0 \\ \frac{q^2(\gamma-1)}{2}+\frac{c\left(u\hat{\xi_x}+w\hat{\xi_z}\right)}{\sqrt{\hat{\xi_x^2}+\hat{\xi_z^2}}} & -\left[(\gamma-1)u+\frac{c\hat{\xi_x}}{\sqrt{\hat{\xi_x^2}+\hat{\xi_z^2}}}\right] & -\left[(\gamma-1)w+\frac{c\hat{\xi_z}}{\sqrt{\hat{\xi_x^2}+\hat{\xi_z^2}}}\right] & (\gamma-1) & -\mathbf{C}(\gamma-1) & 0 \\ -\frac{k}{\rho} & 0 & 0 & 0 & \frac{1}{\rho} & 0 \\ -\frac{\omega}{\rho} & 0 & 0 & 0 & 0 & \frac{1}{\rho} \end{bmatrix}$$

Eigenvalue Split Jacobians

The eigenvalue split Jacobian is:

$$\mathbf{A}_{inv} = \begin{bmatrix} T\Lambda T_{11}^{-1} & T\Lambda T_{12}^{-1} & T\Lambda T_{13}^{-1} & T\Lambda T_{14}^{-1} & T\Lambda T_{15}^{-1} & 0 \\ T\Lambda T_{21}^{-1} & T\Lambda T_{22}^{-1} & T\Lambda T_{23}^{-1} & T\Lambda T_{24}^{-1} & T\Lambda T_{25}^{-1} & 0 \\ T\Lambda T_{31}^{-1} & T\Lambda T_{32}^{-1} & T\Lambda T_{33}^{-1} & T\Lambda T_{34}^{-1} & T\Lambda T_{35}^{-1} & 0 \\ T\Lambda T_{41}^{-1} & T\Lambda T_{42}^{-1} & T\Lambda T_{43}^{-1} & T\Lambda T_{44}^{-1} & T\Lambda T_{45}^{-1} & 0 \\ T\Lambda T_{51}^{-1} & T\Lambda T_{52}^{-1} & T\Lambda T_{53}^{-1} & T\Lambda T_{54}^{-1} & T\Lambda T_{55}^{-1} & 0 \\ T\Lambda T_{61}^{-1} & T\Lambda T_{62}^{-1} & T\Lambda T_{63}^{-1} & T\Lambda T_{64}^{-1} & T\Lambda T_{65}^{-1} & T\Lambda T_{66}^{-1} \end{bmatrix}$$

where:

$$T\Lambda T_{11}^{-1} = \lambda_0 + \tfrac{(\lambda_1-\lambda_0)}{2c^2}\left[\tfrac{q^2(\gamma-1)}{2} - \tfrac{c\lambda_0}{\sqrt{\xi_x^2+\xi_z^2}}\right] + \tfrac{(\lambda_2-\lambda_0)}{2c^2}\left[\tfrac{q^2(\gamma-1)}{2} + \tfrac{c\lambda_0}{\sqrt{\xi_x^2+\xi_z^2}}\right],$$

$$T\Lambda T_{12}^{-1} = \tfrac{(\lambda_1-\lambda_0)}{2c^2}\left[\tfrac{c\xi_x}{\sqrt{\xi_x^2+\xi_z^2}} - u\,(\gamma-1)\right] - \tfrac{(\lambda_2-\lambda_0)}{2c^2}\left[\tfrac{c\xi_x}{\sqrt{\xi_x^2+\xi_z^2}} + u\,(\gamma-1)\right],$$

$$T\Lambda T_{13}^{-1} = \tfrac{(\lambda_1-\lambda_0)}{2c^2}\left[\tfrac{c\xi_z}{\sqrt{\xi_x^2+\xi_z^2}} - w\,(\gamma-1)\right] - \tfrac{(\lambda_2-\lambda_0)}{2c^2}\left[\tfrac{c\xi_z}{\sqrt{\xi_x^2+\xi_z^2}} + w\,(\gamma-1)\right],$$

$$T\Lambda T_{14}^{-1} = (\lambda_1-\lambda_0)\,\frac{(\gamma-1)}{2c^2} + (\lambda_2-\lambda_0)\,\frac{(\gamma-1)}{2c^2},$$

$$T\Lambda T_{15}^{-1} = -\,(\lambda_1-\lambda_0)\,\frac{\mathbf{C}\,(\gamma-1)}{2c^2} - (\lambda_2-\lambda_0)\,\frac{\mathbf{C}\,(\gamma-1)}{2c^2},$$

$$\begin{aligned} T\Lambda T_{21}^{-1} = {} & \tfrac{\lambda_1-\lambda_0}{2c^2}\left(u + \tfrac{c\xi_x}{\sqrt{\xi_x^2+\xi_z^2}}\right)\left[\tfrac{1}{2}q^2\,(\gamma-1) - \tfrac{c\lambda_0}{\sqrt{\xi_x^2+\xi_z^2}}\right] + \\ & \tfrac{\lambda_2-\lambda_0}{2c^2}\left(u - \tfrac{c\xi_x}{\sqrt{\xi_x^2+\xi_z^2}}\right)\left[\tfrac{1}{2}q^2\,(\gamma-1) + \tfrac{c\lambda_0}{\sqrt{\xi_x^2+\xi_z^2}}\right], \end{aligned}$$

$$T\Lambda T_{22}^{-1} = \begin{array}{c} \lambda_0 + \\ \frac{(\lambda_1-\lambda_0)}{2c^2}\left(u+\frac{c\xi_x}{\sqrt{\xi_x^2+\xi_z^2}}\right)\left[\frac{c\xi_x}{\sqrt{\xi_x^2+\xi_z^2}}-u\left(\gamma-1\right)\right]+ \\ \frac{(\lambda_2-\lambda_0)}{2c^2}\left(u-\frac{c\xi_x}{\sqrt{\xi_x^2+\xi_z^2}}\right)\left[-\frac{c\xi_x}{\sqrt{\xi_x^2+\xi_z^2}}-u\left(\gamma-1\right)\right] \end{array},$$

$$T\Lambda T_{23}^{-1} = \begin{array}{c} \frac{\lambda_1-\lambda_0}{2c^2}\left(u+\frac{c\xi_x}{\sqrt{\xi_x^2+\xi_z^2}}\right)\left[\frac{c\xi_z}{\sqrt{\xi_x^2+\xi_z^2}}-w\left(\gamma-1\right)\right]+ \\ \frac{\lambda_2-\lambda_0}{2c^2}\left(u-\frac{c\xi_x}{\sqrt{\xi_x^2+\xi_z^2}}\right)\left[-\frac{c\xi_z}{\sqrt{\xi_x^2+\xi_z^2}}-w\left(\gamma-1\right)\right] \end{array},$$

$$T\Lambda T_{24}^{-1} = \begin{array}{c} \frac{\lambda_1-\lambda_0}{2c^2}\left(\gamma-1\right)\left(u+\frac{c\xi_x}{\sqrt{\xi_x^2+\xi_z^2}}\right) \\ +\frac{\lambda_2-\lambda_0}{2c^2}\left(\gamma-1\right)\left(u-\frac{c\xi_x}{\sqrt{\xi_x^2+\xi_z^2}}\right) \end{array}$$

$$T\Lambda T_{25}^{-1} = \begin{array}{c} -\frac{(\lambda_1-\lambda_0)}{2c^2}\mathbf{C}\left(\gamma-1\right)\left(u+\frac{c\xi_x}{\sqrt{\xi_x^2+\xi_z^2}}\right) \\ -\frac{(\lambda_2-\lambda_0)}{2c^2}\mathbf{C}\left(\gamma-1\right)\left(u-\frac{c\xi_x}{\sqrt{\xi_x^2+\xi_z^2}}\right) \end{array}$$

$$T\Lambda T_{31}^{-1} = \begin{array}{c} \frac{\lambda_1-\lambda_0}{2c^2}\left(w+\frac{c\xi_z}{\sqrt{\xi_x^2+\xi_z^2}}\right)\left[\frac{1}{2}q^2\left(\gamma-1\right)-\frac{c\lambda_0}{\sqrt{\xi_x^2+\xi_z^2}}\right]+ \\ \frac{\lambda_2-\lambda_0}{2s^2}\left(w-\frac{c\xi_z}{\sqrt{\xi_x^2+\xi_z^2}}\right)\left[\frac{1}{2}q^2\left(\gamma-1\right)+\frac{c\lambda_0}{\sqrt{\xi_x^2+\xi_z^2}}\right], \end{array}$$

$$T\Lambda T_{32}^{-1} = \begin{array}{c} \frac{(\lambda_1-\lambda_0)}{2c^2}\left(w+\frac{c\xi_z}{\sqrt{\xi_x^2+\xi_z^2}}\right)\left[\frac{c\xi_x}{\sqrt{\xi_x^2+\xi_z^2}}-u\left(\gamma-1\right)\right]+ \\ \frac{(\lambda_2-\lambda_0)}{2c^2}\left(w-\frac{c\xi_z}{\sqrt{\xi_x^2+\xi_z^2}}\right)\left[-\frac{c\xi_x}{\sqrt{\xi_x^2+\xi_z^2}}-u\left(\gamma-1\right)\right] \end{array},$$

$$T\Lambda T_{33}^{-1} = \begin{array}{c} \lambda_0 + \\ \frac{(\lambda_1-\lambda_0)}{2c^2}\left(w+\frac{c\xi_z}{\sqrt{\xi_x^2+\xi_z^2}}\right)\left[\frac{c\xi_z}{\sqrt{\xi_x^2+\xi_z^2}}-w\left(\gamma-1\right)\right]+ \\ \frac{(\lambda_2-\lambda_0)}{2c^2}\left(w-\frac{c\xi_z}{\sqrt{\xi_x^2+\xi_z^2}}\right)\left[-\frac{c\xi_z}{\sqrt{\xi_x^2+\xi_z^2}}-w\left(\gamma-1\right)\right] \end{array},$$

$$T\Lambda T_{34}^{-1} = \begin{array}{l} \frac{\lambda_1-\lambda_0}{2c^2}\left(\gamma-1\right)\left(w+\frac{c\xi_z}{\sqrt{\xi_x^2+\xi_z^2}}\right)+ \\ \frac{\lambda_2-\lambda_0}{2c^2}\left(\gamma-1\right)\left(w-\frac{c\xi_z}{\sqrt{\xi_x^2+\xi_z^2}}\right) \end{array}$$

$$T\Lambda T_{35}^{-1} = \begin{array}{l} -\frac{(\lambda_1-\lambda_0)}{2c^2}C\left(\gamma-1\right)\left(w+\frac{c\xi_z}{\sqrt{\xi_x^2+\xi_z^2}}\right) \\ -\frac{(\lambda_2-\lambda_0)}{2c^2}C\left(\gamma-1\right)\left(w-\frac{c\xi_z}{\sqrt{\xi_x^2+\xi_z^2}}\right) \end{array}$$

$$T\Lambda T_{41}^{-1} = \begin{array}{l} \frac{\lambda_1-\lambda_0}{2c^2}\left[H+\frac{c\lambda_0}{\sqrt{\xi_x^2+\xi_z^2}}\right]\left[\frac{q^2}{2}\left(\gamma-1\right)-\frac{c\lambda_0}{\sqrt{\xi_x^2+\xi_z^2}}\right]+ \\ \frac{\lambda_2-\lambda_0}{2c^2}\left[H-\frac{c\lambda_0}{\sqrt{\xi_x^2+\xi_z^2}}\right]\left[\frac{q^2}{2}\left(\gamma-1\right)+\frac{c\lambda_0}{\sqrt{\xi_x^2+\xi_z^2}}\right] \end{array}$$

$$T\Lambda T_{42}^{-1} = \begin{array}{l} \frac{\lambda_1-\lambda_0}{2c^2}\left[H+\frac{c\lambda_0}{\sqrt{\xi_x^2+\xi_z^2}}\right]\left[\frac{c\xi_x}{\sqrt{\xi_x^2+\xi_z^2}}-u\left(\gamma-1\right)\right] \\ \frac{\lambda_2-\lambda_0}{2c^2}\left[H-\frac{c\lambda_0}{\sqrt{\xi_x^2+\xi_z^2}}\right]\left[-\frac{c\xi_x}{\sqrt{\xi_x^2+\xi_z^2}}-u\left(\gamma-1\right)\right] \end{array}$$

$$T\Lambda T_{43}^{-1} = \begin{array}{l} \frac{\lambda_1-\lambda_0}{2c^2}\left[H+\frac{c\lambda_0}{\sqrt{\xi_x^2+\xi_z^2}}\right]\left[\frac{c\xi_z}{\sqrt{\xi_x^2+\xi_z^2}}-w\left(\gamma-1\right)\right] \\ \frac{\lambda_2-\lambda_0}{2c^2}\left[H-\frac{c\lambda_0}{\sqrt{\xi_x^2+\xi_z^2}}\right]\left[-\frac{c\xi_z}{\sqrt{\xi_x^2+\xi_z^2}}-w\left(\gamma-1\right)\right] \end{array}$$

$$T\Lambda T_{44}^{-1} = \lambda_0 + \frac{\lambda_1-\lambda_0}{2c^2}\left[H + \frac{c\lambda_0}{\sqrt{\xi_x^2+\xi_z^2}}\right](\gamma-1) + \frac{\lambda_2-\lambda_0}{2c^2}\left[H - \frac{c\lambda_0}{\sqrt{\xi_x^2+\xi_z^2}}\right](\gamma-1)$$

$$T\Lambda T_{45}^{-1} = -\frac{(\lambda_1-\lambda_0)}{2c^2}\left[H + \frac{c\lambda_0}{\sqrt{\xi_x^2+\xi_z^2}}\right]C(\gamma-1) - \frac{(\lambda_2-\lambda_0)}{2s^2}\left[H - \frac{c\lambda_0}{\sqrt{\xi_x^2+\xi_z^2}}\right]C(\gamma-1)$$

$$T\Lambda T_{51}^{-1} = +\frac{(\lambda_1-\lambda_0)}{2c^2}k\left[\frac{q^2}{2}(\gamma-1) - \frac{c\lambda_0}{\sqrt{\xi_x^2+\xi_z^2}}\right] + \frac{(\lambda_2-\lambda_0)}{2c^2}k\left[\frac{q^2}{2}(\gamma-1) + \frac{c\lambda_0}{\sqrt{\xi_x^2+\xi_z^2}}\right]$$

$$T\Lambda T_{52}^{-1} = +\frac{(\lambda_1-\lambda_0)}{2c^2}k\left[\frac{c\xi_x}{\sqrt{\xi_x^2+\xi_z^2}} - u(\gamma-1)\right] + \frac{(\lambda_2-\lambda_0)}{2c^2}k\left[-\frac{c\xi_x}{\sqrt{\xi_x^2+\xi_z^2}} - u(\gamma-1)\right]$$

$$T\Lambda T_{53}^{-1} = +\frac{(\lambda_1-\lambda_0)}{2c^2}k\left[\frac{c\xi_z}{\sqrt{\xi_x^2+\xi_z^2}} - w(\gamma-1)\right] + \frac{(\lambda_2-\lambda_0)}{2c^2}k\left[-\frac{c\xi_z}{\sqrt{\xi_x^2+\xi_z^2}} - w(\gamma-1)\right]$$

$$T\Lambda T_{54}^{-1} = \frac{(\lambda_1-\lambda_0)}{2c^2}k(\gamma-1) + \frac{(\lambda_2-\lambda_0)}{2c^2}k(\gamma-1)$$

$$T\Lambda T_{55}^{-1} = \lambda_0 - \frac{(\lambda_1-\lambda_0)}{2c^2}k\mathbf{C}(\gamma-1) - \frac{(\lambda_2-\lambda_0)}{2c^2}k\mathbf{C}(\gamma-1)$$

$$T\Lambda T_{61}^{-1} = \begin{array}{l} +\frac{(\lambda_1-\lambda_0)}{2c^2}\omega\left[\frac{q^2}{2}(\gamma-1)-\frac{c\lambda_0}{\sqrt{\xi_x^2+\xi_z^2}}\right] \\ +\frac{(\lambda_2-\lambda_0)}{2c^2}\omega\left[\frac{q^2}{2}(\gamma-1)+\frac{c\lambda_0}{\sqrt{\xi_x^2+\xi_z^2}}\right] \end{array}$$

$$T\Lambda T_{62}^{-1} = \begin{array}{l} +\frac{(\lambda_1-\lambda_0)}{2c^2}\omega\left[\frac{c\xi_x}{\sqrt{\xi_x^2+\xi_z^2}}-u(\gamma-1)\right] \\ +\frac{(\lambda_2-\lambda_0)}{2c^2}\omega\left[-\frac{c\xi_x}{\sqrt{\xi_x^2+\xi_z^2}}-u(\gamma-1)\right] \end{array}$$

$$[T\Lambda T^{-1}]_{63} = \begin{array}{l} +\frac{(\lambda_1-\lambda_0)}{2c^2}\omega\left[\frac{c\xi_z}{\sqrt{\xi_x^2+\xi_z^2}}-w(\gamma-1)\right] \\ +\frac{(\lambda_2-\lambda_0)}{2c^2}\omega\left[-\frac{c\xi_z}{\sqrt{\xi_x^2+\xi_z^2}}-w(\gamma-1)\right] \end{array}$$

$$T\Lambda T_{64}^{-1} = \frac{(\lambda_1-\lambda_0)}{2c^2}\omega(\gamma-1)+\frac{(\lambda_2-\lambda_0)}{2c^2}\omega(\gamma-1)$$

$$T\Lambda T_{65}^{-1} = -\frac{(\lambda_1-\lambda_0)}{2c^2}\omega\mathbf{C}(\gamma-1)-\frac{(\lambda_2-\lambda_0)}{2c^2}\omega\mathbf{C}(\gamma-1)$$

$$T\Lambda T_{66}^{-1} = \lambda_0$$

Appendix D

Viscous Jacobians

- ξ Viscous Jacobian

$$\mathbf{A}_{vis,\xi} = \frac{\partial \mathbf{R}}{\partial \mathbf{U}_\xi} = \begin{bmatrix} 0 & 0 & 0 & 0 & 0 & 0 \\ A_{vis,\xi 21} & A_{vis,\xi 22} & A_{vis,\xi 23} & 0 & 0 & 0 \\ A_{vis,\xi 31} & A_{vis,\xi 32} & A_{vis,\xi 33} & 0 & 0 & 0 \\ A_{vis,\xi 41} & A_{vis,\xi 42} & A_{vis,\xi 43} & A_{vis,\xi 44} & A_{vis,\xi 45} & 0 \\ A_{vis,\xi 51} & 0 & 0 & 0 & A_{vis,\xi 55} & 0 \\ A_{vis,\xi 61} & 0 & 0 & 0 & 0 & A_{vis,\xi 66} \end{bmatrix}$$

where:

$$A_{vis,\xi 21} = -\frac{1}{J}\frac{1}{Re}(\mu + \mu_t)\left[\left(\frac{4}{3}\hat{\xi_x}\hat{\xi_x} + \hat{\xi_z}\hat{\xi_z}\right)\left(\frac{u}{\rho}\right) + \left(\frac{1}{3}\hat{\xi_x}\hat{\xi_z}\right)\left(\frac{w}{\rho}\right)\right]$$

$$A_{vis,\xi 22} = \frac{1}{J}\frac{1}{Re}(\mu + \mu_t)\left(\frac{4}{3}\hat{\xi_x}\hat{\xi_x} + \hat{\xi_z}\hat{\xi_z}\right)\left(\frac{1}{\rho}\right)$$

$$A_{vis,\xi 23} = A_{vis,\xi 32} = \frac{1}{J}\frac{1}{Re}(\mu + \mu_t)\left(\frac{1}{3}\hat{\xi_x}\hat{\xi_z}\right)\left(\frac{1}{\rho}\right)$$

$$A_{vis,\xi 31} = -\frac{1}{J}\frac{1}{Re}(\mu + \mu_t)\left[\left(\frac{1}{3}\hat{\xi_x}\hat{\xi_z}\right)\left(\frac{u}{\rho}\right) + \left(\hat{\xi_x}\hat{\xi_x} + \frac{4}{3}\hat{\xi_z}\hat{\xi_z}\right)\left(\frac{w}{\rho}\right)\right]$$

$$A_{vis,\xi 33} = \frac{1}{J}\frac{1}{Re}\left(\mu+\mu_t\right)\left(\hat{\xi}_x\hat{\xi}_x + \frac{4}{3}\hat{\xi}_z\hat{\xi}_z\right)\left(\frac{1}{\rho}\right)$$

$$A_{vis,\xi 41} = \begin{array}{rl} - & \frac{1}{J}\frac{1}{Re}\left(\mu+\mu_t\right) \left\{\left[u\left(\frac{4}{3}\hat{\xi}_x\hat{\xi}_x + \hat{\xi}_z\hat{\xi}_z\right) + w\left(\frac{1}{3}\hat{\xi}_x\hat{\xi}_z\right)\right]\left(\frac{u}{\rho}\right) + \right. \\ & \left. \left[u\left(\frac{1}{3}\hat{\xi}_x\hat{\xi}_z\right) + w\left(\hat{\xi}_x\hat{\xi}_x + \frac{4}{3}\hat{\xi}_z\hat{\xi}_z\right)\right]\left(\frac{w}{\rho}\right)\right\} \\ + & \frac{1}{J}\frac{1}{Re}\left(\mu\frac{\gamma}{Pr} + \mu_t\frac{\gamma}{Pr_\tau}\right)\left[\left(\hat{\xi}_x\hat{\xi}_x + \hat{\xi}_z\hat{\xi}_z\right)\frac{1}{\rho}\left(\frac{u^2+w^2}{2} - T\right)\right] \end{array}$$

$$A_{vis,\xi 42} = \begin{array}{rl} + & \frac{1}{J}\frac{1}{Re}\left(\mu+\mu_t\right)\left[u\left(\frac{4}{3}\hat{\xi}_x\hat{\xi}_x + \hat{\xi}_z\hat{\xi}_z\right) + w\left(\frac{1}{3}\hat{\xi}_x\hat{\xi}_z\right)\right]\left(\frac{1}{\rho}\right) \\ - & \frac{1}{J}\frac{1}{Re}\left(\mu\frac{\gamma}{Pr} + \mu_t\frac{\gamma}{Pr_\tau}\right)\left(\hat{\xi}_x\hat{\xi}_x + \hat{\xi}_z\hat{\xi}_z\right)\left(\frac{u}{\rho}\right) \end{array}$$

$$A_{vis,\xi 43} = \begin{array}{rl} + & \frac{1}{J}\frac{1}{Re}\left(\mu+\mu_t\right)\left[u\left(\frac{1}{3}\hat{\xi}_x\hat{\xi}_z\right) + w\left(\hat{\xi}_x\hat{\xi}_x + \frac{4}{3}\hat{\xi}_z\hat{\xi}_z\right)\right]\left(\frac{1}{\rho}\right) \\ - & \frac{1}{J}\frac{1}{Re}\left(\mu\frac{\gamma}{Pr} + \mu_t\frac{\gamma}{Pr_\tau}\right)\left(\hat{\xi}_x\hat{\xi}_x + \hat{\xi}_z\hat{\xi}_z\right)\left(\frac{w}{\rho}\right) \end{array}$$

$$A_{vis,\xi 44} = \frac{1}{J}\frac{1}{Re}\left(\mu\frac{\gamma}{Pr} + \mu_t\frac{\gamma}{Pr_\tau}\right)\left(\hat{\xi}_x\hat{\xi}_x + \hat{\xi}_z\hat{\xi}_z\right)\frac{1}{\rho}$$

$$A_{vis,\xi 45} = -\frac{1}{J}\frac{1}{Re}\left(\mu\frac{\gamma}{Pr} + \mu_t\frac{\gamma}{Pr_\tau}\right)\left(\hat{\xi}_x\hat{\xi}_x + \hat{\xi}_z\hat{\xi}_z\right)\left(\frac{1}{\rho}\right)$$

$$A_{vis,\xi 51} = -\frac{1}{J}\frac{1}{Re}\left(\mu+\sigma_\kappa\mu_t\right)\left(\hat{\xi}_x\hat{\xi}_x + \hat{\xi}_z\hat{\xi}_z\right)\left(\frac{k}{\rho}\right)$$

$$A_{vis,\xi 55} = \frac{1}{J}\frac{1}{Re}\left(\mu+\sigma_k\mu_t\right)\left(\hat{\xi}_x\hat{\xi}_x + \hat{\xi}_z\hat{\xi}_z\right)\left(\frac{1}{\rho}\right)$$

$$A_{vis,\xi 61} = -\frac{1}{J}\frac{1}{Re}\left(\mu+\sigma_\omega\mu_t\right)\left(\hat{\xi}_x\hat{\xi}_x + \hat{\xi}_z\hat{\xi}_z\right)\left(\frac{\omega}{\rho}\right)$$

$$A_{vis,\xi 66} = \frac{1}{J}\frac{1}{Re}\left(\mu + \sigma_\omega \mu_t\right)\left(\hat{\xi_x}\hat{\xi_x} + \hat{\xi_z}\hat{\xi_z}\right)\left(\frac{1}{\rho}\right)$$

- ξ Viscous cross term Jacobian

$$\mathbf{A}_{vis,\zeta} = \frac{\partial \mathbf{R}}{\partial \mathbf{U}_\zeta} = \begin{bmatrix} 0 & 0 & 0 & 0 & 0 & 0 \\ A_{vis,\zeta 21} & A_{vis,\zeta 22} & A_{vis,\zeta 23} & 0 & 0 & 0 \\ A_{vis,\zeta 31} & A_{vis,\zeta 32} & A_{vis,\zeta 33} & 0 & 0 & 0 \\ A_{vis,\zeta 41} & A_{vis,\zeta 42} & A_{vis,\zeta 43} & A_{vis,\zeta 44} & A_{vis,\zeta 45} & 0 \\ A_{vis,\zeta 51} & 0 & 0 & 0 & A_{vis,\zeta 55} & 0 \\ A_{vis,\zeta 61} & 0 & 0 & 0 & 0 & A_{vis,\zeta 66} \end{bmatrix}$$

where:

$$A_{vis,\zeta 21} = -\frac{1}{J}\frac{1}{Re}\left(\mu + \mu_t\right)\left[\left(\frac{4}{3}\hat{\zeta_x}\hat{\xi_x} + \hat{\zeta_z}\hat{\xi_z}\right)\left(\frac{u}{\rho}\right) + \left(\hat{\zeta_x}\hat{\xi_z} - \frac{2}{3}\hat{\zeta_z}\hat{\xi_x}\right)\left(\frac{w}{\rho}\right)\right]$$

$$A_{vis,\zeta 22} = \frac{1}{J}\frac{1}{Re}\left(\mu + \mu_t\right)\left(\frac{4}{3}\hat{\zeta_x}\hat{\xi_x} + \hat{\zeta_z}\hat{\xi_z}\right)\left(\frac{1}{\rho}\right)$$

$$A_{vis,\zeta 23} = A_{vis,\zeta 32} = \frac{1}{J}\frac{1}{Re}\left(\mu + \mu_t\right)\left(\hat{\zeta_x}\hat{\xi_z} - \frac{2}{3}\hat{\zeta_z}\hat{\xi_x}\right)\left(\frac{1}{\rho}\right)$$

$$A_{vis,\zeta 33} = \frac{1}{J}\frac{1}{Re}\left(\mu + \mu_t\right)\left(\hat{\zeta_x}\hat{\xi_x} + \frac{4}{3}\hat{\zeta_z}\hat{\xi_z}\right)\left(\frac{1}{\rho}\right)$$

$$A_{vis,\zeta 31} = -\frac{1}{J}\frac{1}{Re}\left(\mu + \mu_t\right)\left[\left(\hat{\zeta_z}\hat{\xi_x} - \frac{2}{3}\hat{\zeta_x}\hat{\xi_z}\right)\left(\frac{u}{\rho}\right) + \left(\hat{\zeta_x}\hat{\xi_x} + \frac{4}{3}\hat{\zeta_z}\hat{\xi_z}\right)\left(\frac{w}{\rho}\right)\right]$$

$$\begin{aligned} A_{vis,\zeta 41} = & - \frac{1}{J}\frac{1}{Re}\left(\mu + \mu_t\right) \begin{array}{c} \left\{\left[u\left(\frac{4}{3}\hat{\zeta_x}\hat{\xi_x} + \hat{\zeta_z}\hat{\xi_z}\right) + w\left(\hat{\zeta_z}\hat{\xi_x} - \frac{2}{3}\hat{\zeta_x}\hat{\xi_z}\right)\right]\left(\frac{u}{\rho}\right) + \\ \left[u\left(\hat{\zeta_x}\hat{\xi_z} - \frac{2}{3}\hat{\zeta_z}\hat{\xi_x}\right) + w\left(\hat{\zeta_x}\hat{\xi_x} + \frac{4}{3}\hat{\zeta_z}\hat{\xi_z}\right)\right]\left(\frac{w}{\rho}\right)\right\} \end{array} \\ & + \frac{1}{J}\frac{1}{Re}\left(\mu\frac{\gamma}{Pr} + \mu_t\frac{\gamma}{Pr_\tau}\right)\left[\left(\hat{\zeta_x}\hat{\xi_x} + \hat{\zeta_z}\hat{\xi_z}\right)\frac{1}{\rho}\left(\frac{u^2+w^2}{2} - T\right)\right] \end{aligned}$$

$$A_{vis,\zeta 42} = \begin{array}{c} \frac{1}{J}\frac{1}{Re}\left(\mu+\mu_t\right)\left[u\left(\frac{4}{3}\hat{\zeta}_x\hat{\xi}_x+\hat{\zeta}_z\hat{\xi}_z\right)+w\left(\hat{\zeta}_z\hat{\xi}_x-\frac{2}{3}\hat{\zeta}_x\hat{\xi}_z\right)\right]\left(\frac{1}{\rho}\right) \\ - \quad \frac{1}{J}\frac{1}{Re}\left(\mu\frac{\gamma}{Pr}+\mu_t\frac{\gamma}{Pr_\tau}\right)\left(\hat{\zeta}_x\hat{\xi}_x+\hat{\zeta}_z\hat{\xi}_z\right)\left(\frac{u}{\rho}\right) \end{array}$$

$$A_{vis,\zeta 43} = \begin{array}{c} \frac{1}{J}\frac{1}{Re}\left(\mu+\mu_t\right)\left[u\left(\hat{\zeta}_x\hat{\xi}_z-\frac{2}{3}\hat{\zeta}_z\hat{\xi}_x\right)+w\left(\hat{\zeta}_x\hat{\xi}_x+\frac{4}{3}\hat{\zeta}_z\hat{\xi}_z\right)\right]\left(\frac{1}{\rho}\right) \\ - \quad \frac{1}{J}\frac{1}{Re}\left(\mu\frac{\gamma}{Pr}+\mu_t\frac{\gamma}{Pr_\tau}\right)\left(\hat{\zeta}_x\hat{\xi}_x+\hat{\zeta}_z\hat{\xi}_z\right)\left(\frac{w}{\rho}\right) \end{array}$$

$$A_{vis,\zeta 44} = \frac{1}{J}\left(\mu\frac{\gamma}{Pr}+\mu_t\frac{\gamma}{Pr_\tau}\right)\left(\hat{\zeta}_x\hat{\xi}_x+\hat{\zeta}_z\hat{\xi}_z\right)\frac{1}{\rho}$$

$$A_{vis,\zeta 45} = -\frac{1}{J}\frac{1}{Re}\left(\mu\frac{\gamma}{Pr}+\mu_t\frac{\gamma}{Pr_\tau}\right)\left(\hat{\zeta}_x\hat{\xi}_x+\hat{\zeta}_z\hat{\xi}_z\right)\left(\frac{1}{\rho}\right)$$

$$A_{vis,\zeta 51} = -\frac{1}{J}\frac{1}{Re}\left(\mu+\sigma_\kappa\mu_t\right)\left(\hat{\zeta}_x\hat{\xi}_x+\hat{\zeta}_z\hat{\xi}_z\right)\left(\frac{k}{\rho}\right)$$

$$A_{vis,\zeta 55} = \frac{1}{J}\frac{1}{Re}\left(\mu+\sigma_\kappa\mu_t\right)\left(\hat{\zeta}_x\hat{\xi}_x+\hat{\zeta}_z\hat{\xi}_z\right)\left(\frac{1}{\rho}\right)$$

$$A_{vis,\zeta 61} = -\frac{1}{J}\frac{1}{Re}\left(\mu+\sigma_\omega\mu_t\right)\left(\hat{\zeta}_x\hat{\xi}_x+\hat{\zeta}_z\hat{\xi}_z\right)\left(\frac{\omega}{\rho}\right)$$

$$A_{vis,\zeta 66} = \frac{1}{J}\frac{1}{Re}\left(\mu+\sigma_\omega\mu_t\right)\left(\hat{\zeta}_x\hat{\xi}_x+\hat{\zeta}_z\hat{\xi}_z\right)\left(\frac{1}{\rho}\right)$$

The viscous Jacobian $\mathbf{C}_{vis,\zeta}$ follows by simple substitution of ξ with ζ in $\mathbf{A}_{vis,\xi}$. For the viscous cross term Jacobian, it can be proved that $\mathbf{C}_{vis,\xi} = \mathbf{A}_{vis,\zeta}$

References

[1] White, F. M., *Viscous Fluid Flow*, McGraw-Hill International Edition, 3rd ed., 2005.

[2] Lissaman, P. B. S., "Low-Reynolds-Number Airfoils," *Annual Review of Fluid Mechanics*, Vol. 15, 1982, pp. 223–239.

[3] Carmichael, B. H., "Low Reynolds Number airfoil survey, volume 1," NASA-CR-165803-VOL-1, 1981.

[4] Mueller, T. J. and DeLaurier, J. D., "Aerodynamics of Small Vehicles," *Annual Review of Fluid Mechanics*, Vol. 35, No. 35, 2003, pp. 89–111.

[5] Stanewsky, E., "Adaptive wing and flow control technology," *Progress in Aerospace Sciences*, Vol. 37, No. 7, 2001, pp. 583–667.

[6] Peake, D. J., Henry, F. S., and Pearcey, H. H., "Viscous flow control with air-jet vortex generators," AIAA-1999-3175, 1999.

[7] Ashill, P. R., Fulker, J. L., and Hackett, K. C., "Research at DERA on sub boundary layer vortex generators (SBVGS)," AIAA-2001-0887, 2001.

[8] Seifert, A. and Pack, L. G., "Oscillatory control of separation at high Reynolds numbers," *AIAA*, Vol. 37, No. 9, 1999, pp. 1062–1071.

[9] Stanewsky, E. and Krogmann, P., "Transonic drag rise and drag reduction by active/passive boundary layer control," *Aircraft Drag Prediction and Reduction*, AGARD REPORT No.723, 1985, pp. 11.1–11.41.

[10] Hefner, J. N. and Bushnell, D. M., "Viscous Drag Reduction via Surface Mass Injection," *Viscous Drag Reduction in Boundary Layers*, Vol. 123, Progress in Astronautics and Aeronautics, 1990, pp. 457–476.

[11] Jeffrey, D. R. M. and Hurst, D. W., "Aerodynamics of the Gurney flap," AIAA-1996-2418, 1996.

[12] Meyer, R., Bechert, D. W., and Hage, W., "Wind tunnel experiment with artificial bird feathers for passive separation control on airfoils," *IUTAM Symposium on Mechanics of Passive and Active Flow Control*, edited by G. E. A. Meier and P. R. Viswanath, Kluwer Academic Publishers, 1999, pp. 99–100.

[13] Kimura, M., Tung, S., Ho, C. M., Jiang, F., and Tai, Y. C., "MEMS for Aerodynamic control," AIAA-1997-2118, 1997.

[14] Ho, C. M., Huang, P. H., Yang, J. M., Lee, G. B., and Thai, Y. C., "Active Flow Control by Micro Systems," *IUTAM Symposium on Mechanics of Passive and Active Flow Control*, edited by G. E. A. Meier and P. R. Viswanath, Kluwer Academic Publishers, 1999, pp. 195–202.

[15] Raghunathan, S. and Mabey, D. G., "Passive shockwave boundary layer control experiments on a circular arc model," AIAA-1986-0285, 1986.

[16] Stanewsky, E., Delery, J., J., J. F., and Geissler, W., *Notes on numerical fluid dynamics, Vol. 56, EUROSHOCK-Drag reduction by passive shock control*, Friedrich Vieweg & Sohn Verlag, 1997.

[17] Ashill, P. R., Fulker, J. L., and Simmons, M. J., "Study of simulated active control of shock waves on aerofoil sections," DRA-TR-93025, 1993.

[18] McCormick, D. C., "Shock/boundary-layer interaction control with vortex generators and passive cavity," *AIAA*, Vol. 31, No. 1, 1993, pp. 91–96.

[19] Siclari, M. J., van Nostrand, W., and Austin, F., "The design of transonic airfoil sections for an adaptive wing concept using a stochastic optimization method," AIAA-1996-0329, 1996.

[20] Smith, S. B. and Nelson, D. W., "Determination of the aerodynamic characteristics of the Mission Adaptive Wing," *Journal of Aircraft*, Vol. 27, No. 11, 1990, pp. 950–958.

[21] Szodruch, J., "The influence of camber variation on the aerodynamics of civil transport aircraft," AIAA-1985-353, 1985.

[22] Thorton, S. V., "Reduction of structural loads using maneuver load control on the Advanced Fighter Technology Integration (AFTI)/F-111 Mission Adaptive Wing," NASA-TM-4526, 1993.

[23] Teves, D., Niesl, G., Blaas, A., and Jacklin, S., "The role of active control in future rotorcraft," *21st European Rotorcraft Forum*, Saint Petersburg, Russia, 30 August - 1 September 1995.

[24] Kessler, C., Fuerst, D., and Arnold, U. T., "Open Loop Flight Test Results and Closed Loop Status of the IBC System on the CH-53G Helicopter," *American Helicopter Society 59th Annual Forum*, Phoenix, Arizona, USA, 6-8 May 2003.

[25] Roth, D., "Advanced vibration reduction by IBC technology," *30th European Rotorcraft Forum*, Marseilles, France, 14-16 September 2004.

[26] Arnold, U. T., Fuerst, D., Neuheuser, T., and Bartels, R., "Development of an Integrated Electrical Swashplateless Primary and Individual Blade Control System," *American Helicopter Society 63rd Annual Forum*, Virginia Beach, USA, 1-3 May 2007.

[27] Giurgiutiu, V., "Review of Smart-Materials Actuation Solutions for Aerolelastic and Vibration Control," *Journal of Intelligent Material Systems and Strucures*, Vol. 11, No. 7, 2000, pp. 525–544.

[28] Drikakis, D. and W.Rider, *High-Resolution Methods for Incompressible and Low-Speed Flows*, Springer, 2005.

[29] Harten, A., "High resolution schemes for hyperbolic conservation laws," *Journal of Computational Physics*, Vol. 135, No. 2, 1997, pp. 260–278.

[30] Toro, E. F., *Riemann Solvers and Numerical Methods for Fluid Dynamics: A Practical Introduction*, Springer-Verlag, 2nd ed., 1999.

[31] Richtmyer, R. D. and Morton, K. W., *Difference Methods for Initial-Value Problems*, Krieger, 2nd ed., 1994.

[32] van Leer, B., "Towards the ultimate conservative difference Scheme I. The quest for monotonicity," *Lecture Notes in Physics*, Vol. 18, 1973, pp. 163–168.

[33] van Leer, B., "Towards the ultimate conservative difference scheme II. Monotonicity and conservation combined in a second-order scheme," *Lecture Notes in Physics*, Vol. 14, 1974, pp. 361–370.

[34] van Leer, B., "Towards the ultimate conservative difference scheme III. Upstream-centered finite-difference schemes for ideal compressible flow," *Lecture Notes in Physics*, Vol. 23, No. 3, 1977, pp. 263–275.

[35] Roe, P. L., "Some contributions to the modelling of discontinuous Flows," *Large-scale computations in fluid mechanics; Proceedings of the Fifteenth Summer Seminar on Applied Mathematics*, American Mathematical Society, La Jolla, CA, 27 June - 8 July 1983.

[36] van Albada, G. D., van Leer, B., and Roberts, W. W., "A comparative study of computational methods in cosmic gas dynamics," *Astronomy and Astrophysics*, Vol. 108, No. 1, 1982, pp. 76–84.

[37] Shu, C. W., "Essentially Non-Oscillatory and Weighted Essentially Non-Oscillatory Schemes for Hyperbolic Conservation Laws," NASA/CR-97-206253, 1997.

[38] Zaki, T. A. and Durbin, P. A., "Mode interaction and the bypass route to transition," *Journal of Fluid Mechanics*, Vol. 531, 2005, pp. 85–111.

[39] Liu, Y., Zaki, T. A., and Durbin, P. A., "Boundary-layer transition by interaction of discrete and continuous modes," *Journal of Fluid Mechanics*, Vol. 604, 2008, pp. 199–233.

[40] Piomelli, U., Balaras, E., Squires, K. D., and Spalart, P. R., "Interaction of the inner and outer layers in large-eddy simulations with wall-layer models," *Engineering Turbulence Modelling and Experiments 5*, edited by W. Rodi and N. Fueyo, Elsevier, 2002, pp. 307–316.

[41] Moin, P. and Kim, J., "Tackling turbulence with supercomputers," *Scientific American*, Vol. 276, 1997, pp. 62–68.

[42] Wilcox, D. C., *Turbulence Modeling for CFD*, DCW Industries, Inc., 2nd ed., 1999.

[43] Hutton, A. G. and Ashworth, R. M., "The challenge of turbulence modelling in modern aeronautical design," *International Journal for Numerical Method in Fluids*, Vol. 47, 2005, pp. 721–737.

[44] Hellsten, A., *New two-equation turbulence model for aerodynamic applications*, Ph.D. thesis, Helsinki University of Technology, 2004.

[45] Smith, A. M. O. and Cebeci, T., "Numerical solution of the turbulent-boundary-layer equations," DAC-33735, Douglas Aircraft Division, 1967.

[46] Baldwin, B. S. and Lomax, H., "Thin-layer approximation and algebraic model for separated turbulent flows," AIAA-1978-257, 1978.

[47] Johnson, D. A. and King, L. S., "A mathematically simple turbulent closure model for attached and separated turbulent boundary layers," *AIAA*, Vol. 23, No. 11, 1985, pp. 1684–1692.

[48] Baldwin, B. S. and Barth, T. J., "A one-equation turbulence transport model for high Reynolds number wall-bounded flows," AIAA-1991-610, 1991.

[49] Spalart, P. R. and Allmaras, S. R., "A One Equation Turbulence Model for Aerodynamic Flows," AIAA-1992-0439, 1992.

[50] Hajela, P., "Nongradiend Methods in Multidisciplinary Design OPtimization - Status and Potential," *Journal of Aircraft*, Vol. 36, No. 1, 1999, pp. 255–265.

[51] Kipouros, T., *Multi-Objective Aerodynamic Design Optimisation*, Ph.D. thesis, University of Cambridge, 2006.

[52] Aly, S., Ogot, M., and Pelz, R., "Stochastic Approach to Optimal Aerodynamic Shape Design," *Journal of Aircraft*, Vol. 33, No. 5, 1996, pp. 956–961.

[53] Kirkpatrick, S., Gelatt, C. D., and Vecchi, M. P., "Optimization by Simulated Annealing," *Science*, Vol. 220, No. 4598, 1983.

[54] Aarts, E. and Korst, J., *Simulated Annealing and Boltzmann Machines: A Stochastic Approach to Combinatorial Optimisation and Neural Computing*, John Willey & Sons, 1988.

[55] Goldberg, D. E., *Genetic Algorithms in Search, Optimization and Machine Learning*, Addison-Wesley Longman Publishing Company, 1989.

[56] Glover, F., "Future paths for integer programming and links to artificial intelligence," *Computers and Operations Research*, 1986.

[57] Glover, F. W. and Laguna, M., *Tabu Search*, Kluwer Academic Publishers, 1997.

[58] Vanderplaats, G. N., *Numerical Optimization Techniques for Engineering Design with applications*, McGraw-Hill, 1984.

[59] Jaeggi, D. M., Asselin-Miller, C. S., Parks, G. T., Kipouros, T., Bell, T., and Clarkson, P. J., "Multi-Objective Parallel Tabu Search," *Lecture Notes in Computer Science*, Vol. 3242, 2004, pp. 732–741.

[60] Harvey, S. A., *The Design Optimisation of Turbomachinery Blade Rows*, Ph.D. thesis, Cambridge University, 2002.

[61] Hansen, M. P., "Tabu Search for Multiobjective Optimization:MOTS," *Proceedings of the 13th International Conference on Multiple Criteria Decision Making (MCDN'97)*, 1997.

[62] Baykasoglu, A., Owen, S., and Gindy, N., "A taboo search based approach to find the pareto optimal set in multiple objective optimization," *Engineering Optimization*, Vol. 31, No. 6, 1999, pp. 731–748.

[63] Connor, P. and Tilley, D., "A Tabu search method for the optimisation of fluid power circuits," *Journal of Systems and Control Engineering*, Vol. 212, No. 5, 1998, pp. 373–381.

[64] Hooke, R. and Jeeves, T. A., "Direct Search Solution of Numerical and Statistical Problems," *Journal of the ACM*, Vol. 8, No. 2, 1961, pp. 212–229.

[65] Kipouros, T., Parks, G. T., Savill, A. M., and Jaeggi, D. M., "Multi-objective aerodynamic design optimisation," *ERCOFTAC Design Optimization: Methods and Applications. International Conference and Advanced Course Program*, Athens, Greece, 2004.

[66] Jaeggi, D., Parks, G., Kipouros, T., and Clarkson, P., "A Multi-objective Tabu Search Algorithm for Constrained Optimisation Problems," *Lecture Notes in Computer Science*, Vol. 3410, 2005, pp. 490–504.

[67] Hirsch, C., *Numerical Computation of Internal and External Flows, Volume 1: Fundamentals of Numerical Discretization*, Wiley, New York, 1988.

[68] Anderson, J. D., *Computational Fluid Dynamics: The Basics with Applications*, McGraw-Hill, 1995.

[69] Reynolds, O., "On the Dynamical Theory of Incompressible Viscous Fluids and the Determination of the Criterion," *Philosophical Transactions of the Royal Society of London*, Vol. 186, 1895, pp. 123–164.

[70] Favre, A., "Equations des gaz turbulents compressibles," *Journal de mécanique*, Vol. 4, No. 10, 1965, pp. 361–390.

[71] Jones, W. P. and Launder, B. E., "The prediction of laminarization with a two-equation model of turbulence," *International Journal of Heat and Mass Transfer*, Vol. 15, No. 2, 1972, pp. 301–314.

[72] Launder, B. E. and Sharma, B. I., "Application of the energy-dissipation model of turbulence to the calculation of flow near a spinning disk," *Letters in Heat and Mass Transfer*, Vol. 1, 1974, pp. 131–137.

[73] Kolmogorov, A. N., "Equations of turbulent motion of an incompressible fluid," *Izvestia Akademii Nauk SSSR, Serija Fizicheskaya*, Vol. 6, 1942, pp. 56–58.

[74] Menter, F. R., "Improved Two-Equation k-ω Turbulence Models for Aerodynamic Flows," NASA-TM-103975, 1992.

[75] Kok, J. C., "Resolving the Dependence on Freestream Values for the k-ω Turbulence Model," *AIAA*, Vol. 38, No. 7, 2000, pp. 1292–1295.

[76] Menter, F. R., "Two-equation eddy-viscosity turbulence models for engineering applications," *AIAA*, Vol. 32, No. 8, 1994, pp. 1598–1605.

[77] Hirsch, C., *Numerical Computation of Internal and External Flows, Volume 2: Computational Methods for Inviscid and Viscous Flows*, Wiley, New York, 1990.

[78] Venkateswaran, S. and Merkle, L., "Analysis of preconditioning methods for the Euler and Navier-Stokes equations," *Lecture series - von Karman Institute for Fluid Dynamics*, Vol. 3, 1999, pp. B1–B155.

[79] Lee, S. and Choi, D. W., "On coupling the Reynolds-averaged Navier-Stokes equations with two-equation turbulence model equations," *International Journal of Numerical Methods in Fluids*, Vol. 50, No. 2, 2006, pp. 165–197.

[80] Godunov, S. K., "A finite difference method for the computation of discontinuous solutions of the equations of fluid dynamics," *Matematicheskii Sbornic*, Vol. 47, 1959, pp. 271–306.

[81] Einfeldt, B., Munz, C. D., Roe, P. L., and Sjörgreen, B., "On Godunov-type methods near low densities," *Journal of Computational Physics*, Vol. 92, No. 2, 1991, pp. 273–295.

[82] Eberle, A., "Characteristic flux averaging approach to the solution of Euler's equations," *Lecture series - von Karman Institute for Fluid Dynamics*, Vol. 4, 1987, pp. 1–60.

[83] Roe, P. L., "Approximate Riemann Solvers, Parameter Vectors and Difference Schemes," *Journal of Computational Physics*, Vol. 43, 1981, pp. 357–372.

[84] Batten, P., Leschziner, M. A., and Goldberg, U. C., "Average-state Jacobians and implicit methods for compressible viscous and turbulent flows," *Journal of Computational Physics*, Vol. 137, No. 1, 1997, pp. 38–78.

[85] Harten, A., Lax, P. D., and van Leer, B., "On Upstream Differencing and Godunov-Type Schemes for hyperbolic Conservation Laws," *SIAM Review*, Vol. 25, No. 1, 1983, pp. 35–61.

[86] Toro, E. F., Spruce, M., and Speares, W., "Restoration of the contact surface in the HLL-Riemann solver," *Shock Waves*, Vol. 4, No. 1, 1994, pp. 25–34.

[87] Batten, P., Clarke, N., Lambert, C., and Causon, D. M., "On the Choice of Wavespeeds for the HLLC Riemann Solver," *SIAM Journal on Scientific Computing*, Vol. 18, No. 6, 1997, pp. 1553–1570.

[88] Chakravarthy, S., "High Resolution Upwind Formulations for the Navier-Stokes Equations," *Lecture series - von Karman Institute for Fluid Dynamics*, Vol. 5, 1988.

[89] Drikakis, D. and Durst, F., "Parallelization of inviscid and viscous flow solvers," *International Journal of Computational Fluid Dynamics*, Vol. 3, No. 2, 1994, pp. 101–121.

[90] Drikakis, D., Shreck, E., and Durst, F., "Performance analysis of viscous flow computations on various parallel architectures," *ASME Journal of Fluids Engineering*, Vol. 116, No. 4, 1994, pp. 835–841.

[91] Schmatz, M. A., "Three-dimensional viscous flow simulations using an implicit relaxation scheme," *Numerical simulation of compressible viscous flow aerodynamics. Notes on Numerical Fluid Dynamics*, edited by W. Kordulla, Vieweg, Braunschweig - Wiesbaden, 1988, pp. 226–243.

[92] Schmatz, M. A., Brenneis, A., and Eberle, A., "Verification of an implicit relaxation method for steady and unsteady viscous and inviscid flow problems," *Validation of Computational Fluid Dynamics*, AGARD-CP-437, 1988, pp. 15.1–15.33.

[93] Steger, J. L. and Warming, R. F., "Flux vector splitting of the inviscid gasdynamic equations with application to finite-difference methods," *Journal of Computational Physics*, Vol. 40, 1981, pp. 263–293.

[94] Eberle, A., Rizzi, A., and Hirschel, E. H., "Numerical Solutions of the Euler Equations for Steady Flow Problems," *SIAM Review*, Vol. 37, No. 2, 1995, pp. 271–272.

[95] Cook, P. H., McDonald, M. A., and Firmin, M. C. P., "Aerofoil RAE2822-Pressure Distributions,and Boundary Layer and Wake Measurements," AGARD-AR-138, 1979.

[96] Haase, W., Bradsma, F., Elsholz, E., Leschziner, M., and Schwamborn, D., "EUROVAL-An European Initiative on Validation of CFD Codes," *Notes on Numerical Fluid Mechanics*, Vol. 42, 1993.

[97] Moryossef, Y. and Levy, Y., "Unconditionally positive implicit procedure for two-equation turbulence models: Application to k-ω turbulence models," *Journal of Computational Physics*, Vol. 220, No. 6, 2006, pp. 88–108.

[98] Catalano, P. and Amato, M., "An evaluation of RANS turbulence modelling for aerodynamic applications," *Aerospace Science and Technology*, Vol. 7, No. 3, 2003, pp. 493–509.

[99] Lien, F. S. and Kalitzin, G., "Computations of transonic flow with the u^2-f model," *International Journal of Heat and Fluid Flow*, Vol. 22, No. 1, 2001.

[100] Barakos, G. N., *Study of Unsteady Aerodynamics Phenomena Using Advanced Turbulent Closures*, Ph.D. thesis, The University of Manchester, 1999.

[101] Coles, D. and Wadcock, A. J., "Flying-Hot-wire Study of Flow Past an NACA 4412 Airfoil at Maximum Lift," *AIAA*, Vol. 17, No. 4, 1979, pp. 321–329.

[102] Hellsten, A. and Laine, S., "Explicit algebraic Reynolds-stress modelling in decelerating and separating flows," AIAA-2000-2313, 2000.

[103] Kim, C. S., Kim, C., and RHO, O. H., "Parallel computations of high-lift airfoil flows using two-equation turbulence models," *AIAA*, Vol. 38, No. 8, 2000, pp. 1360–1368.

[104] Schmidt, S., Franke, M., and Thiele, F., "Assessment of SGS Models in LES Applied to a NACA 4412 Airfoil," AIAA-2001-0434, 2001.

[105] Zhong, B. and Qiao, Z., "Multiobjective Optimization Design of Transonic Airfoils," Tech. rep., 1994.

[106] Kumar, G. N. S., Mahendra, A. K., and Rao, S. V. R., "Shape Optimization using Hybrid GA-ACO method and grid-free CFD solver," AIAA-2007-3830, 2007.

[107] Hazra, S. B., Schulz, V., Brezillon, J., and Gauger, N. R., "Aerodynamic shape optimization using simultaneous pseudo-timestepping," *Journal of Computational Physics*, Vol. 204, No. 1, 2005, pp. 46–64.

[108] Epstein, B. and Peigin, S., "Accurate CFD driven optimization of lifting surfaces for wing-body configuration," *Computers & Fluids*, Vol. 36, No. 9, 2007, pp. 1399–1414.

[109] Zachariadis, Z. I., Shapiro, E., and Drikakis, D., "Investigation of Aerofoil Morphing for Advanced Blade Design," *Cranfield Multi-Strand Conference Proceedings*, 6-7 May 2008 2008, In Print.

[110] Noonan, K. W., "Aerodynamic characteristics of two rotorcraft airfoils designed for application to the inboard region of a main rotor blade," NASA-TP-3009, 1990.

[111] Soni, B. K., "Two- and three-dimensional grid generation for internal flow applications of computational fluid dynamics," AIAA-1985-1526, 1985.

[112] Spekreijse, S. P., Prananta, B. B., and Kok, J. C., "A simple, robust and fast algorithm to compute deformations of multi-block structured grids," NLR-TP-2002-105, 2002.

[113] Farrashkhalvat, M. and Miles, J. P., *Basic Structured Grid Generation: With an Introduction to Unstructured Grid Generation*, Butterworth-Heinemann, 2003.

[114] Smith, R. E., "Transfinite Interpolation (TFI) Generation Systems," *Handbook of Grid Generation*, edited by J. F. Thompson, B. K. Soni, and N. P. Weatherill, CRC Press, 1999, pp. 3.1–3.15.

[115] Wong, A. S. F., Tsai, H. M., Cai, J., Zhu, Y., and Liu, F., "Unsteady flow calculations with a multi-block moving mesh algorithm," AIAA-2000-1002, 2000.

[116] Spalart, P. R., "Trends in turbulence treatments," AIAA-2000-2306, 2000.

[117] Girimaji, S. S. and Abdol-Hamid, K. S., "Partially-averaged Navier Stokes Model for Turbulence: Implementation and Validation," AIAA-2005-502, 2005.

[118] Silverman, B. W., *Density Estimation for Statistics and Data Analysis*, Chapman & Hall, 1986.